GIS-Based tools and methods for landscape analysis and active tectonic evaluation

José Vicente Pérez Peña

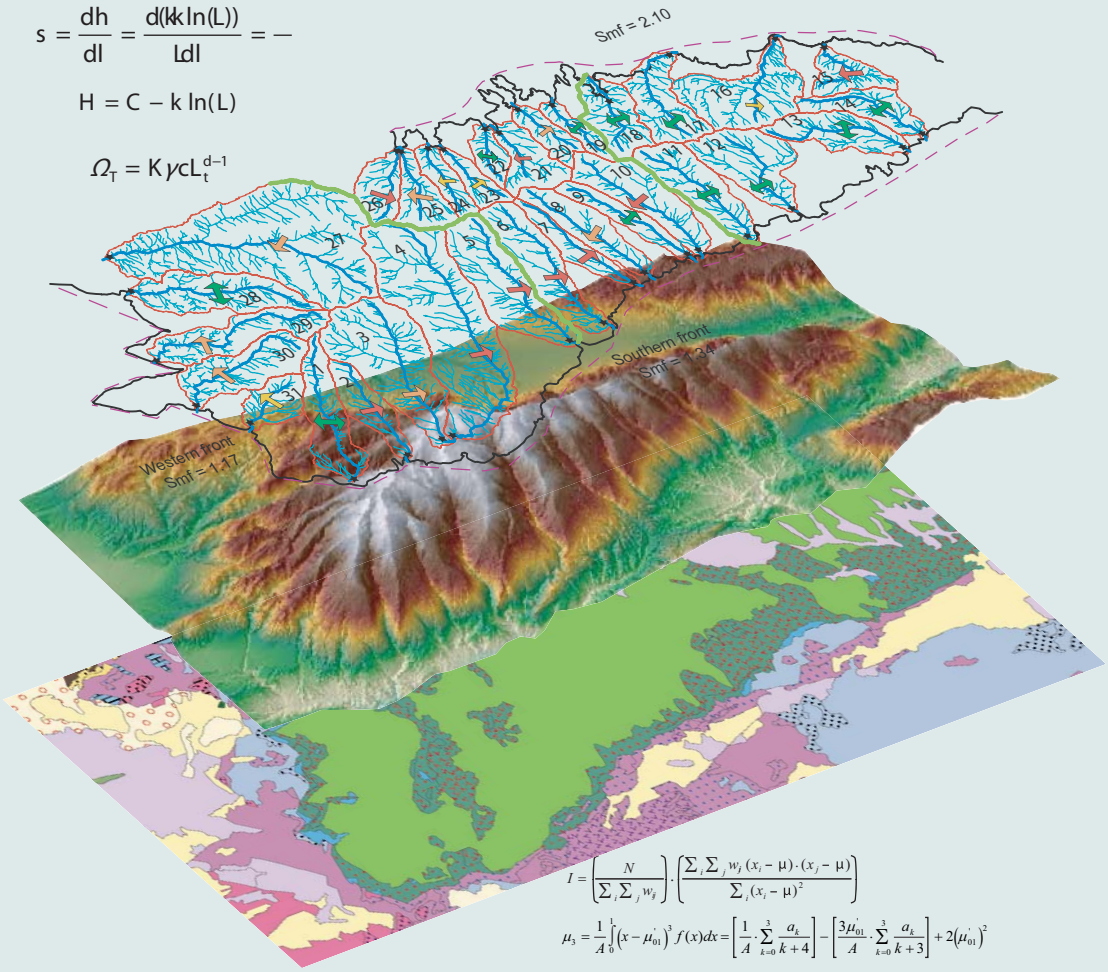

$$s = \frac{dh}{dl} = \frac{d(k - k\ln(L))}{Ldl} = -$$

$$H = C - k\ln(L)$$

$$\Omega_T = K\gamma c L_t^{d-1}$$

$$I = \left[\frac{N}{\sum_i \sum_j w_{ij}}\right] \cdot \left[\frac{\sum_i \sum_j w_j (x_i - \mu)\cdot(x_j - \mu)}{\sum_i (x_i - \mu)^2}\right]$$

$$\mu_3 = \frac{1}{A}\int_0^1 \left(x - \mu_{01}^{'}\right)^3 f(x)dx = \left[\frac{1}{A}\cdot\sum_{k=0}^{3}\frac{a_k}{k+4}\right] - \left[\frac{3\mu_{01}^{'}}{A}\cdot\sum_{k=0}^{3}\frac{a_k}{k+3}\right] + 2\left(\mu_{01}^{'}\right)^2$$

$$\mu_4 = \frac{1}{A}\int_0^1 \left(x - \mu_{01}^{'}\right)^4 f(x)dx = \left[\frac{1}{A}\cdot\sum_{k=0}^{3}\frac{a_k}{k+5}\right] - \left[\frac{4\mu_{01}^{'}}{A}\cdot\sum_{k=0}^{3}\frac{a_k}{k+4}\right] + \left[\frac{6}{A}\left(\mu_{01}^{'}\right)^2\cdot\sum_{k=0}^{3}\frac{a_k}{k+4}\right] - 3\left(\mu_{01}^{'}\right)^4$$

ugr
Tesis Doctoral 2009
Universidad de Granada
Departamento de Geodinámica

Editor: Editorial de la Universidad de Granada
Autor: José Vicente Pérez Peña
D.L.: GR. 2053-2009
ISBN: 978-84-692-2262-1

Departamentdo de Geodinámica
Universidad de Granada

José Miguel Azañon Hernández y Antonio Azor Pérez, doctores y profesores titulares del Departamento de Geodinámica de la Universidad de Granada hacen constar:

Que la presente memoria titulada "*GIS-Based tools and methods for landscape analysis and active tectonic evaluation*" ha sido realizada bajo su dirección por el doctorando José Vicente Pérez Peña y cumple las suficientes condiciones para que su autor pueda optar al grado de Doctor en Ciencias Geologicas por la Universidad de Granada.

José Vicente Pérez Peña

Vº Bº José Miguel Azañón Hernández

Vº Bº Antonio Azor Pérez

Granada, Marzo 2009

Agradecimientos:

Mi gratitud más sincera a mis dos directores de tesis: A José Miguel Azañón por haber estado siempre ahí desde el principio del todo, por su orientación y disposición incondicional, aún cuando no era director de esta tesis. A Antonio Azor, que a pesar de haberse incorporado más tarde, ha hecho una gran labor crítica y de supervisión, ayudando a aumentar en gran medida la calidad de esta tesis y de las publicaciones que de ella se han derivado. Es una suerte haber podido trabajar con ambos, por lo mucho que he aprendido y porque sin su ayuda no habría podido completar mi camino hacia doctor. También quiero dar las gracias a mi antiguo director Francisco González Loderio, que a pesar de que tuvo que delegar la dirección, siempre ha estado interesado por mí y por esta Tesis Doctoral. Mi gratitud sincera a Jesús Galindo, que me acogió y oriento al principio, y asumió en cierto modo funciones de director interino.

Esta tesis es el fruto de la colaboración estrecha con muchos investigadores. Mi gratitud a Jorge Delgado, pues gran parte de las metodologías que se presentan en esta tesis no habrían sido posibles sin su ayuda y colaboración. También quiero agradecer especialmente a Guillermo Booth-Rea, uno de los mejores geólogos de campo que he conocido, por su apoyo y colaboración en el último tramo de esta tesis. Mi gratitud también a José Rodríguez-Fernández, Antonio Jabaloy, Carlos Sanz, José Miguel Martínez-Martínez, Juan Ignacio Soto, y otros muchos investigadores de mi departamento y CSIC.

A los geólogos del GNS en Wellington, Pilar Villamor, Robert Langridge, Kelvin Berryman y Russ van Dissen, por acogerme y enseñarme tantas cosas. Ha sido una gran suerte haber podido trabajar con ellos en un sitio tan espectacular como Nueva Zelanda.

A los investigadores y geólogos de la Universidad de la Sapienza en Roma, especialmente a Marta della Seta, Maurizio, y Franchesca.

A mis amigos de la sala de becarios, con los que he compartido muchos años de esta tesis. Me siento muy afortunado de haber encontrado a tan grandes personas como compañeros y amigos. A Jesús Yesares, con quien comencé en esta aventura, por tantos buenos ratos en nuestro despacho y en la madroñera. A Fermín, que aunque esté lejos, está muy cerca. A Carlos, y su hermano Ricardo (geólogo adoptado) por tantos buenos ratos, dentro y fuera del departamento, porque su casa siempre ha estado abierta. A Antonio Pedrera, por los buenos ratos que he pasado con él, ya sea en campo, charlando de ciencia o en alguna que otra actividad ociosa. A Pedro, una persona excepcional, que estoy seguro hará una gran tesis (aunque le decepcione si no hago el brikindans). A Chema, al que ha sido una suerte conocerle aunque se haya incorporado hace poco. A Silvia por su naturalidad y sencillez. A Ana y su kiosco en la Gran Vía. A Farida por su cariño y alegría. A las chicas de mine y paleo por revitalizar la unión entre becarios.

A Julia, Concha, Claudio, Isa, David, José María, Roció, por su compañía y tantos buenos miércoles (antiguo-día-no-oficial-del-becario).

A Patricia por su gran disponibilidad siempre que necesite algo. A mis compañeros de sobremesa, Paco, Ana Luque, Antonio Acosta, Annika y algunos interinos.

A mis compañeros de carrera, tanto los que se decidieron por la ciencia como los que no. En especial a mis amigos David, Edu, Pablo, Paco, y Florian.

A mis compañeros de piso, que me han sufrido a mí y a esta tesis. Especialmente a Jose Maria, mi prima Mari Chus, Sebatian (y Rocío), Cord, y Christoff.

Al SSC (Alicia, Carmen, Oze Maria, y Eli), que espero tener siempre como amigos y apoyo a la hora de hacer un sandwich.

A mis amigos del pueblo (Priego), Cachu, Julen, Largo, Plata, Compay, Alvaro, Zitroqui, Manolo Bermudez, Jose Gonzalez, Pepe, Mamen, Patruki, Casti, Mamenes, Ursu y María, por haber estado ahí desde que éramos niños. Espero tenerlos siempre muy cerca, como lo han estado durante toda mi vida. A Tere, por haber estado ahí desde el principio hasta el final.

Y especialmente a mi familia, a quien quiero dedicar esta tesis.

Si te sientas en el camino, ponte de frente a lo que aún has de andar y de espaldas a lo ya andado.
(Antiguo proverbio Chino)

INDEX OF CONTENTS:

RESUMEN EXTENDIDO

1. INTRODUCCIÓN

Los Sistemas de Información Geográfica (SIG) constituyen hoy en día una de las herramientas más útiles para la representación, gestión, y análisis de datos espaciales. El uso de los SIG en geología ha experimentado un notable crecimiento en los últimos años, como se puede ver en el alto número de publicaciones científicas de primer orden sobre modelos y metodologías realizados con SIG. Los SIG se pueden contar hoy en día entre las herramientas de trabajo fundamentales en muchos campos de la geología, debido principalmente a tres factores: la versatilidad y potencia en el manejo de datos geo-espaciales, la posibilidad de realizar modelos complejos que usen funciones analíticas para derivar datos, y el uso de estadísticos específicos para datos espaciales, lo que se conoce como "geoestadística". Los primeros usos de los SIG en geología fueron en geomorfología, para la realización de análisis multi-criterio de riesgos (susceptibilidad frente a deslizamientos, riesgos de inundaciones, etc.). En el campo de la tectónica activa y evolución del relieve, su uso no está aún muy generalizado, aunque cada vez son más los investigadores que se dan cuenta de las grandes posibilidades que ofrece la aplicación de los SIGs en estos campos. En esta tesis, se ha pretendido dar un paso en esa dirección, mediante la presentación de utilidades y metodologías diseñadas mediante SIG y enfocadas hacia el estudio de la evolución del relieve y la evaluación de la actividad tectónica reciente. Los capítulos 2, 3 y 4 se centran en dos características de las redes de drenaje y cuencas hidrográficas: la pendiente de los ríos y la hipsometría de las cuencas. Estas aplicaciones se han desarrollado para ArcGIS y hacen uso de métodos geoestadísticos que mejoran notablemente los resultados. También se presenta un método para la reconstrucción de la morfología original de cuencas sedimentarias que luego han sido parcialmente erosionadas con la desarrollo de una red de drenaje; el objetivo último de este análisis es estimar las tasas de erosión y la evolución del relieve durante el cuaternario. En el capítulo 4, se analiza la red de drenaje y diversos índices geomorfológicos en Sierra Nevada, para dilucidar su evolución cuaternaria y la actividad tectónica más reciente.

Estos métodos se han aplicado en la parte central de la Cordillera Bética (SE España), concretamente en las cuencas de Granada, Guadix-Baza, y el antiforme de Sierra Nevada. La Cordillera Bética (junto con el Rif) representa el extremo más occidental de la Cadena Alpina Perimediterránea. Incluye los relieves más importantes del sur de la Península Ibérica y se suele dividir en 3 conjuntos mayores; el dominio Sudibérico o Zona Externa (que incluye el Prebélico y Subbético), el dominio de los Flysch del Campo de

Gibraltar, y el dominio de Alborán o Zona Interna (constituido a su vez por los complejos Maláguide, Alpujárride, y Nevado Filábride). También se incluye en la cordillera un volumen muy importante de sedimentos en cuencas Neógeno-Cuaternarias, como son la cuenca del Guadalquivir (cuenca de antepaís), las cuencas de Granada, Guadix-Baza, Lorca, Ronda, Sorbas-Tabernas, Vera, y el mar de Alborán (cuenca de retro-arco situada entre las Béticas y el Rif).

La Cordillera Bética se formo durante el Neógeno en un régimen general de convergencia entre las placas Euroasiática y Africana. Una posterior extensión (coetánea con una compresión general N-S) generó fallas normales de bajo y alto ángulo, algunas de las cuales muestran actividad en el presente. Las causas de si esta extensión, y por ende los mecanismos que la generaron, es activa a día de hoy es un tema de debate. La orografía de la parte central de la Cordillera Bética está caracterizada por una serie de sierras (que alcanzan hasta los 3400 m de altura en el caso Sierra Nevada) y depresiones topográficas (cuencas sedimentarias). Las sierras corresponden en su mayoría a estructuras antiformales abiertas de dirección general E-O, relacionadas con la compresión dominante N-S a NW-SE entre Iberia y Africa. En la parte central de la Cordillera, se localizan las cuencas de Granada y Guadix-Baza, al Oeste y Norte de Sierra Nevada, respectivamente. La evolución de estas cuencas en el cuaternario, así como su morfología actual está fuertemente influida por la tectónica y estrechamente relacionada con la evolución de Sierra Nevada y la tectónica extensional de esta parte de la Cordillera.

2. ANÁLISIS ESPACIAL DEL POTENCIAL EROSIVO DE LOS RÍOS MEDIANTE SIG: MAPAS DE ANOMÁLIA DE SLK

El índice del gradiente longitudinal de un río (SL, según sus siglas en inglés) muestra las variaciones del poder erosivo a lo largo de los distintos segmentos del mismo, multiplicando la pendiente del tramo por la distancia a la cabecera. Este índice es muy sensible a los cambios de pendiente, y por lo tanto permite la evaluación de la actividad tectónica y/o los cambios litológicos a lo largo del lecho del río. Sin embargo, la comparación de valores de SL procedentes de ríos con distinta longitud es problemática debido a la propia formulación del índice. Este hecho hace que las correlaciones entre valores de SL de ríos de distinta longitud puedan resultar equívocas. Para llevar a cabo tales comparaciones es necesaria una normalización de este índice. La pendiente graduada (K) ha sido utilizada en algunos trabajos para la normalización del índice SL. Sin embargo, las relaciones entre K, el índice SL, y el poder erosivo del río no han sido estudiadas con detalle. En este capítulo, se exploran estas relaciones y se propone el uso de un índice normalizado SLk. Así mismo, se propone un método para la extracción de mapas de anomalías de SLk, basado en ArcGIS y en métodos geoestadísticos. Para verificar las ventajas de este nuevo índice, se ha

realizado un estudio en el borde NE de la cuenca de Granada, donde se compara un mapa de anomalía del índice SLk con un simple análisis de puntos de rotura de pendiente en perfiles de ríos, y frente a un mapa de SL no normalizado. Los resultados muestran que el mapa de anomalía de SLk se adapta mejor a la tectónica y litología generales del área estudiada.

3. METODOS DE AUTOCORRELACIÓN ESPACIAL APLICADOS A LA INTEGRAL HIPSOMÉTRICA PARA DETECTAR ATIVIDAD TECTÓNICA

La hipsometría, entendida ésta como las relaciones entre área y altura, es muy sensible al levantamiento tectónico y a la litología. La hipsometría en un área se puede evaluar por medio de la curva hipsométrica o la integral hipsométrica (HI, según sus siglas en inglés). En este capítulo, se calcula la integral hipsométrica para la cuenca de Granada usando dos fuentes topográficas diferentes: un modelo digital de elevaciones de 10 metros de resolución obtenido mediante vuelos fotogramétricos y un modelo de 90 metros de resolución obtenido mediante radar de satélite. La integral hipsométrica se ha calculado para una malla cuadrada regular para evitar posibles dependencias del área y forma de la cuenca. Las distribuciones espaciales de HI no ofrecen patrones claros y no se correlacionan con parámetros morfométricos como la elevación media o la amplitud del relieve de cada uno de los cuadrados. Tampoco se observa una correlación clara entre la litología y los valores de HI. Sin embargo, tras la aplicación de índices locales de correlación espacial (LISA, según sus siglas en inglés) sobre las distribuciones de HI, se observan claras agrupaciones de valores altos y bajos. Estas distribuciones son robustas e independientes del modelo digital utilizado, pero están influidas por la escala. Los valores de hipsometría de la cuenca de Granada obtenidos mediante esta nueva metodología muestran una fuerte correlación con la distribución actual de fallas normales. Los máximos de HI se localizan en los bloques de muro de estas fallas normales, donde se produce elevación activa y el relieve está siendo disectado por la red de drenaje actual, así como en regiones elevadas en relación con anticlinales tipo roll-over o donde el levantamiento epi-orogénico no ha sido contrarrestado por la extensión local. Una vez que este método ha sido puesto a punto en la cuenca de Granada, se ha chequeado su aplicabilidad en una zona de conocida actividad tectónica compresiva, la región de Otago Central en la Isla Sur de Nueva Zelanda. Con el estudio realizado en esta última región, se pone de manifiesto que la aplicación de estas técnicas geoestadísticas mejora muy notablemente el uso de la integral hipsométrica para deducir actividad tectónica reciente.

3. CALHYPSO: UN MODULO DE ARCGIS DISEÑADO PARA LA EXTRACCIÓN AUTOMATICA DE CURVAS HIPSOMÉTRICAS Y SUS MOMENTOS ESTADÍSTICOS RELACIONADOS

En este capítulo se presenta la extensión Calypso, desarrollada para ArcGIS, y que permite la extracción automática de múltiples curvas hipsométricas a partir de datos de modelos digitales de elevación. Esta extensión ha sido desarrollada en Visual Basic 6 y usa las características y arquitectura de los ArcObjects. Esto proporciona una integración óptima dentro del entorno del programa permitiendo la representación y comparación de curvas hipsométricas directamente dentro del mismo. Esta extensión también calcula los momentos estadísticos relacionados con la curva hipsométrica mediante la aplicación de ajustes polinómicos. Esta utilidad se ha testado mediante la realización de un estudió de las diferentes curvas hipsométricas en la terminación este de Sierra Nevada. Las diferencias entre las curvas de la vertiente norte y sur está probablemente relacionada con el control tectónico del borde sur y la evolución cuaternaria de la red de drenaje en esta parte de la Sierra. Los estatidísticos usados sugieren una disminución de la erosión hacía el este, provocada probablemente por una disminución de la actividad tectónica.

4. EVOLUCIÓN CUATERNARIA DEL RELIEVE Y TASAS DE EROSION DE UNA CUENCA INTRAMONTAÑOSA (CUENCA DE GUADIX-BAZA, CORDILLERA BÉTICA)

La evolución del relieve en una cuenca intra-montañosa es el resultado de la interacción de varios factores como son: la litología, el clima y la tectónica. Una vez que la sedimentación cesa y la cuenca pasa de endorreica a exorreica, ésta entra en un estadio erosivo. La estimación espacial de tasas de erosión ofrece una visión inmejorable de la evolución de la cuenca desde el momento de su captura. En este capítulo, se calculan las tasas de erosión en la cuenca de Guadix-Baza desde que cesó la sedimentación en la misma y comenzó el encajamiento de la red fluvial actual. Para ello se ha restaurado la morfología de la superficie de colmatación de la cuenca y realizado un modelo digital pre-incisión que permita estimar el volumen de sedimentos erosionados. Los cálculos se han hecho mediante un método basado en SIG con el que se obtienen el máximo número de puntos posibles de esta superficie de referencia. Esta superficie se corresponde con un glacis marcado por una calcreta de facies laminares, que ha sido datada por medio del método U/Th. La edad de la captura de la cuenca endorreica por parte del río Guadalquivir es un tema actualmente en debate. Para reforzar las dataciones ya existentes de esta calcreta, se han realizado dataciones por medio de U/Th en otros puntos de la cuenca de Guadix-Baza. Con todo ello, se han calculado las tasas de erosión para la totalidad de la cuenca, así como las tasas específicas de las sub-cuencas de Guadix y Baza por separado. Las tasas de erosión globales para la

cuenca de Guadix-Baza en el Pleistoceno superior - Holoceno se sitúan entre 4.28 y 6.57 m^3 ha^{-1} $año^{-1}$, y son interpretadas como la consecuencia de la interacción de factores climáticos, litológicos, topográficos, y tectónicos. Las tasas de erosión espaciales también permiten tener una idea de la evolución del relieve en el Pleistoceno superior - Holoceno. Las tasas individuales para las sub-cuencas de Guadix y Baza son muy diferentes (11.80 m^3 ha^{-1} $año^{-1}$ y 1.77 m^3 $año^{-1}$, respectivamente), y por lo tanto sugieren diferentes evoluciones de la red de drenaje en ambas subcuencas. Los valores más bajos, obtenidos en la sub-cuenca de Baza, pueden ser debidos a la actividad tectónica reciente de la falla de Baza (que separa ambas sub-cuencas).

5. TECTONICA ACTIVA EN SIERRA NEVADA (CORDILLERA BÉTICA). UNA APROXIMACIÓN MEDIANTE INDICES GEOMORFOLÓGICOS Y ANALISIS DE LA RED DE DRENAJE

Sierra Nevada se localiza en la parte central de la Cordillera Bética e incluye algunos de los relieves más importantes de toda la península Ibérica. Su levantamiento se inició en el Tortoniense. Los bordes oeste y sur de Sierra Nevada se corresponden con sendos sistemas de fallas. Por el contrario, el borde norte se corresponde con una discordancia de los sedimentos neógeno-cuaternarios de la cuenca de Guadix-Baza sobre el basamento metamórfico de la Sierra.

En este capítulo, se realiza un estudio geomorfológico para tratar de dilucidar la tectónica reciente –esencialmente cuaternaria- en Sierra Nevada. Para ello, se han calculado varios indicies geomorfológicos y se ha analizado la red de drenaje. La sinuosidad de frentes montañosos (S_{mf}) varía sistemáticamente de los frente oeste y sur donde, presenta valores muy cercanos a uno (1.17 y 1.34, respectivamente), al frente norte, donde presenta valores de casi el doble (2.21). El índice V_f (razón de altura y anchura de valles), muestra el mismo patrón, con valores máximos en el borde norte y mínimos en el borde oeste. Las curvas hipsométricas analizadas sugieren que las cuencas de drenaje de la vertiente norte están en un estadio erosivo más avanzado, siendo menos activas tectónicamente que las del borde sur. Todos estos datos sugieren que los frentes oeste y sur son más activos que el norte, hecho que es evidenciado también por otros datos geológicos. La ausencia de fallas importantes entre los sedimentos de la cuenca de Guadix-Baza y Sierra Nevada, junto a la altitud media de esta cuenca (situada aproximadamente 500 metros más alta que la vecina cuenca de Granada), sugieren que el levantamiento de la misma se está produciendo solidariamente con el levantamiento regional de Sierra Nevada. El análisis de la red de drenaje muestra un cierto control tectónico de la misma, puesto en evidencia principalmente mediante el cálculo de los factores de asimetría (AF, según sus siglas en inglés) de las cuencas de drenaje. Los AF calculados muestran únicamente un patrón de asimetría sistemático

a ambos lados del Río Lanjarón, lo que sugiere la existencia de un antiforme activo de dirección NNE-SSO en esta parte occidental de Sierra Nevada. Por último, los perfiles topográficos longitudinales de los ríos indican un encajamiento máximo de los ríos de la parte oeste de la sierra, relacionado seguramente con el levantamiento del bloque de muro del sistema de fallas normales de Padul-Nigüelas. Por tanto, el análisis geomorfológico realizado sugiere que la parte occidental de Sierra Nevada es tectónicamente activa mediante una combinación de fallas normales en su borde y pliegues activos de dirección NNE-SSO, que probablemente tienen un origen gravitatorio en relación con la exhumación del bloque de muro del sistema de fallas normales.

6. CONCLUSIONES

En esta tesis se han presentando nuevas herramientas y metodologías basadas en SIG para el análisis del relieve y la evaluación de la tectónica activa. Estas metodologías están basadas principalmente en el análisis de las redes de drenaje y de los parámetros asociados a ellas. Se han mejorado y re-definido algunos índices básicamente en dos aspectos; la creación de procedimientos para su cálculo mediante SIG, y la aplicación de técnicas geoestadísticas que ayuden mejor a su interpretación espacial.

Se ha presentado un re-definido y normalizado índice de gradiente del río (SLk), así como un procedimiento para la generación de mapas de anomalías de SLk por medio de técnicas geoestadísticas. El mapa de anomalía de SLk generado para el borde NE de la cuenca de Granada pone de manifiesto los principales rasgos tectónicos y litológicos de esta zona, así como la existencia de un frente generado por fallas normales con actividad en el Cuaternario.

Se ha introducido la aplicación de índices locales de autocorrelación especial a distribuciones de valores de la integral hipsométrica (HI). Estos estadísticos de autocorrelación mejoran notablemente el significado tectónico y geológico de las distribuciones de HI. La distribución espacial de los clusters de HI en la cuenca de Granada está estrechamente relacionada con la tectónica reciente. Los clusters de valores altos de HI se localizan en los bloques de muro de fallas normales activas, los cuales están experimentando levantamiento tectónico y subsecuente encajamiento de la red de drenaje.

Se ha diseñado una extensión de ArcGIS (CalHypso) para la extracción automática de curvas hipsométricas y sus momentos estadísticos asociados. El análisis realizado en las cuencas de drenaje de la parte este de Sierra Nevada pone de manifiesto que el frente norte de la misma muestra un estadio erosivo mucho más avanzado que el sur, probablemente relacionado con la actividad cuaternaria de las fallas que limitan este ultimo. Los estadísticos

de las curvas hipsométricas sugieren un decrecimiento de las tasas de incisión hacía el este, lo que podría estar debido a una menor actividad tectónica en esa dirección.

Con los índices geomorfológicos calculados para Sierra Nevada, se sugiere que el levantamiento más reciente de la misma está concentrado en su terminación oeste, y relacionado con la extensión producida por las fallas normales que limitan este frente oeste. Los pliegues más activos son los de dirección NNE-SSO, que tienen a su vez un origen isostático debido a la extensión producida en el frente oeste de la Sierra. La evolución Cuaternaria de las cuencas de Granada y Guadix-Baza es muy diferente, como se apunta por los análisis geomorfológicos realizados. Las diferencias entre el relieve y encajamiento de la red de drenaje de las mismas podría ser debido al hecho de que la cuenca Granada está localizada en el bloque de techo de un sistema extensional de dirección SO que limita el borde oeste de Sierra Nevada, y por lo tanto está sujeta a una mayor extensión. Por el contrario la cuenca de Guadix-Baza está localizada en el bloque de muro de dicho sistema, siendo levantada tectónicamente junto a Sierra Nevada en el Cuaternario.

EXTENDED ABSTRACT

1. INTRODUCTION

Geographic Information Systems constitute nowadays useful tools for representing, and analyzing spatial data. Its development at the end of the last century provided a powerful tool for spatial data analysis and management in almost all the earth science disciplines (mineralogy, structural geology, tectonics, geophysics, geochemistry, etc.). GIS allow not only representing data, but also performing geostatistical analysis and building models. These features make them very useful in earth sciences in general and in geology in particular. The number of geologic works using GIS has grown exponentially in the last decade. In geomorphology, the traditional use of GIS capabilities can be found in works that require multi-criterium analysis. The apparition of Digital Topographic Models (DTM) has contributed definitely to the integration of GIS in geology. In the field of tectonic geomorphology and landscape evolution, the use of GIS is relatively recent. The availability of the aforementioned DEM, in conjunction with the use of new geochronological methods valuables at time-scales below 1 Ma, has produced a great revolution in this field.

This thesis aims to present some new GIS tools and methodologies developed to analyze drainage networks with a view to constrain recent tectonic activity. These GIS-based geomorphic tools have been applied to the central part of the Betic Cordillera, an area with moderate present-day seismicity and tectonic activity. Two main features of rivers and catchments, namely river gradients and hypsometry will be the main focus of this study. Chapters 2, 3, 4 present some new concepts and methodologies that allow a more accurate analysis of river gradients and basin hypsometries by using geostatistic techniques. Chapter 4 presents a new GIS-based method to reconstruct the primary surface morphology of a sedimentary basin prior to be dissected by river entrenchment. Chapter 5 is a study of the drainage network and some geomorphic indexes of the highest mountain range in the Betic Cordillera, namely the Sierra Nevada, with the objective of establishing its Quaternary tectonic activity. This chapter shows the application of the GIS-based tools presented in the previous chapters to an area where all of the geological information available suggests the existence of the highest long- (Tortonian to present-day) and short-term (Quaternary) uplift rates.

All the methodologies proposed and developed in this Thesis have been applied to the Central Betic Cordillera, which is the biggest orographic unit in the Southern Iberian

Peninsula. This work is centered in three important areas, namely the Granada and Guadix-Baza Neogene basins, and the Sierra Nevada mountain range.

The topographic configuration of the internal zone of the Betic Cordilleras is characterized by a series of alternating mountain ranges (up to 3400 m high) and topographic depressions. The mountain ranges are composed of Palaeozoic–Mesozoic metamorphic rocks, while the topographic depressions correspond to basins filled with Neogene–Quaternary sediments. The uplift seems to be controlled by large-scale E-W trending open folds, which, in turn, are related to a dominant N–S compression. Quaternary normal faults and a relatively high concentration of earthquake epicenters characterize two main areas of active extension in the central Betic Cordillera. The first one corresponds to the Granada basin, where high-angle NW–SE striking normal faults are predominant, and the second is found to the west of the Sierra de Gádor, where N–S to NW–SE oriented high-angle normal faults delimit two large-scale eastward-tilted blocks.

2. SPATIAL ANALYSIS OF STREAM POWER USING GIS: SLK ANOMALY MAPS.

The stream length-gradient index (SL) shows the variation in stream power along river reaches. This index is very sensitive to changes in channel slope, thus allowing the evaluation of recent tectonic activity and/or rock resistance. Nevertheless, the comparison of SL values from rivers of different length is biased due to the manner in which the index is formulated, thus making correlations of SL anomalies along different rivers difficult. Therefore, when undertaking a comparison of SL values of rivers of different length, a normalization factor must be used. The graded river gradient (K) has already been used in some studies to normalize the SL index. In this work, we explore the relationships between the graded river gradient (K), the SL index, and the stream power, proposing the use of a re-named SLk index, which enables the comparison of variable-length rivers, as well as the drawing of SLk anomaly maps. In this chapter I present a GIS-based procedure to generate SLk maps and to identify SLk anomalies. In order to verify the advantages of this methodology, I compared a SLk map of the NE border of the Granada basin with both simple river profile-knickpoint identification and with a SL map. The results show that the SLk map supplies good results with defined anomalies and suitably reflects the main tectonic and lithological features of the study area.

3. DIFFERENTIATING GEOLOGY AND TECTONICS USING A SPATIAL AUTOCORRELATION TECHNIQUE FOR THE HYPSOMETRIC INTEGRAL.

Hypsometry is thought to be sensitive to tectonic uplift rates and lithology differences. In this study I calculated hypsometric integrals (HIs) using as topographic sources two digital elevation models of 10 and 90 m of pixel resolution in the Granada basin (SE of Spain). The HI spatial distributions do not show clear spatial patterns and do not correlate with basin parameters as mean elevation or relief amplitude. However, when exploratory spatial data analysis is applied to the data distributions through local indices of spatial autocorrelation (LISA) clear hot-spots are visible that improve the geologic meaning of the HI. The distributions are robust and independent of the model resolution but are scale influenced. The application of this new method to the Granada basin shows a strong correlation between the main distribution of active normal faults in the basin and the clusters of high or low HI values obtained in our analysis. Clusters with high HI values define the uplifted footwalls of these faults and regions uplifted in relation with rollover anticlines or where epeirogenic uplift has not been counteracted by local extension. Once the method was adjusted in the Granada basin I tested its applicability in an area of known contractive tectonic activity, Central Otago in New Zealand, showing that the meaning of HI values is improved by using the autocorrelation techniques.

4. CALHYPSO: AN ARGIS EXTENSION TO CALCULATE HYPSOMETRIC CURVES AND THEIR STATISTICAL MOMENTS. APLICATIONS TO DRAINAGE BASIN ANALYSIS IN SE SPAIN.

We present the GIS extension CalHypso to automatically extract multiple hypsometric curves from digital elevation models (DEM). This extension is programmed in Visual Basic 6 and uses the ArcObjects architecture of ArcGIS. It employs a new and easy methodology to extract the hypsometric curve by using the integer data-model properties of ArcGIS and summations algorithms. This provides an optimal integration within the program environment, allowing the representation and comparison of curves directly within the GIS main program. The CalHypso extension can also calculate the main statistics related to the hypsometric curve by applying polynomial fits. We have tested this tool in several basins of the eastern border of the Sierra Nevada dome in the Betic Cordillera (SE Spain), showing important differences in the north- and south-slope hypsometric curves. These variations are probably related to the tectonically-controlled drainage evolution of the southern border of Sierra Nevada. An eastward decrease in tectonic-driven erosion is also suggested by the hypsometric curves analysed.

5. QUARTERNARY LANDSCAPE EVOLUTION AND EROSION RATES FOR AN INTRAMONTANE NEOGENE BASIN (GUADIX-BAZA BASIN, SE SPAIN).

The landscape evolution in Neogene intramontane basins is a result of the interaction of climatic, lithologic, and tectonic factors. When sedimentation ceases and a basin enters an erosional stage, estimating erosion rates across the entire basin can offer a good view of landscape evolution. In this work, the erosion rates in the Guadix–Baza basin have been calculated based on a volumetric estimate of sediment loss by river erosion since the Late Pleistocene. To do so, the distribution of a glacis surface at ca. 43 ka, characterised by a calcrete layer that caps the basin infilling, has been reconstructed. To support this age, new radiometric data of the glacis are presented. The volume of sediment loss by water erosion has been calculated for the entire basin by comparing the reconstructed geomorphic surface and the present-day topography. The resulting erosion rates vary between 4.28 and 6.57 m3 ha-1 yr-1, and are the consequence of the interaction of climatic, lithologic, topographic, and tectonic factors. Individual erosion rates for the Guadix and Baza sub-basins (11.80 m3 ha-1 yr-1 and 1.77 m3 ha-1 yr-1 respectively) suggest different stages of drainage pattern evolution in the two sub-basins. We attribute the lower values obtained in the Baza sub-basin to the down-throw of this sub-basin caused by very recent activity along the Baza fault.

6. ACTIVE TECTONIC IN THE SIERRA NEVADA (BETIC CORDILLERA, SE SPAIN): INSIGHTS FROM GEOMORPHIC INDEXES AND DRAINAGE PATTERN ANALYSIS.

The Sierra Nevada mountain range, located in the central part of the Betic Cordillera, includes the highest peaks on the Iberian Peninsula (e.g., Mulhacén, 3482 m). It developed since the late Miocene by the interference between two orthogonal sets of NNE-SSW and E-W open folds. We carried out a geomorphologic study with the aid of evaluating the recent tectonic activity in this mountain range. On this purpose, we have calculated several geomorphic indexes in the Sierra Nevada. Mountain front sinuosity (Smf) varies from the southern and western mountain fronts (1.17-1.34) to the northern mountain front (2.10). Ratio of width of valley floor to valley height (Vf) shows the same variation pattern as the Smf, presenting the higher values in the northern mountain front. Hypsometric curves describe younger and more active basins along the southern border of the Sierra Nevada. These data suggest that active faulting is more important in the south and south-western borders of Sierra Nevada, as it is also evidenced by other geological features. The drainage network in the Sierra is tectonically controlled by booth NNE-SSW and W-E folds as is evidenced by basin asymmetries and river flow-directions. Nevertheless, river profiles indicate that maximum linear erosion is concentrated in the western border of the sierra, thus

pointing to maximum uplift related with the NNE-SSW isostatic folds. All these indexes indicate that the recent tectonic activity in the Sierra is mainly controlled by the extensional tectonics in the west and contractional tectonic in the east, where the extensional system became inactive.

7. CONCLUSSIONS

In this thesis new methods for the relief analysis and the recent tectonic evaluation have been presented. We improved previously defined geomorphic indexes basically in two aspects; we adapted their calculation to GIS software, and we applied geostatistic techniques in order to perform better spatial analyses. We also presented a new method to restore the morphology prior to the river entrenchment of a neogene intercontinental basin.

A re-defined and normalized SLk index has been presented in the chapter 2.We proposed a new procedure to generate SLk anomaly maps by using geostatistic techniques. The anomalies of SLk found in the NE border of the Granada basin faithfully reflect the main tectonic and lithological features of this area.

We introduced the application of Local Indicators of Spatial Autocorrelation (LISA) to HI value distributions. The use of such local indices permits the extraction of clusters of high or low HI values that reflect tectonic processes occurring in a region from otherwise highly variable, uninterpretable HI values

We presented a new ArcGIS extension to automatically extract hypsometric curves from Digital Elevations Models. It allows extracting some curve-related statistic parameters such as kurtosis, density kurtosis, skew, density skew, and the hypsometric integral. A study in the eastern part of the Sierra Nevada reveals differences between its northern and southern mountain fronts, being the southern front tectonically inactive. The curve-related statistics suggest an decreasing of the erosion rates eastwards, that could be caused by a decreasing in the tectonic activity in the same direction.

The geomorphic indexes calculated in this thesis for the Sierra Nevada suggest that the more recent uplift is concentrated along its western mountain front, where Smf and Vf present the lowest values. The southern and western mountain fronts of the Sierra Nevada rare fault controlled, while the northern front corresponds to an unconformity between the Neogene-Quaternary sedimentary infill of the Guadix-Baza basin and the metamorphic rocks of the Sierra Nevada. The Quaternary landscape evolution of the Granada and Guadix-Baza basins are very different, and are strongly conditioned by tectonics. The Granada basin located to the west of the Sierra Nevada has a mean altitude of 600 m, being scarcely

incised by the fluvial network. The Guadix-Baza basin located to the north of the Sierra Nevada has a mean altitude of 1000 m, with the fluvial network deeply incised (down to 200 m) into the Neogene-Quaternary infill. These topographic and geomorphic differences are probably due to the different tectonic location of the two basins: The Granada basin is located in the hanging wall of the SW-directed extensional system bounding to the west the Sierra Nevada. On the contrary, the Guadix-Baza basin is located in the footwall of the above-mentioned extensional system, being part together with the whole Sierra Nevada of a single block suffering tectonic uplift during the Quaternary.

1

INTRODUCTION

1. GEOGRAPHIC INFORMATION SYSTEMS (GIS) AS TOOLS FOR TECTONIC GEOMORPHOLOGY

1.1 GIS: Definition, key concepts, brief history, and evolution

1.1.1. Definition and key concepts

Geographic Information Systems (GIS) integrate hardware, software and data for capturing, managing, analyzing and displaying all forms of geographically referenced information. GIS can be viewed as a model of part of the reality referred to a coordinate system built for a specific need of information. GIS allow viewing, understanding, questioning, interpreting and visualizing data in many ways and, therefore, reveal relationships, patterns, trends, etc.

GIS organize geographic data into a series of thematic layers and tables (Fig. 1). Since these geographic datasets are georeferenced, they have real-world locations and overlay each other. Spatial relationships between layers can be derived and analyzed. These layers or datasets can represent raw measurements, compiled and interpreted information or data derived through geoprocessing operations for analysis and modeling. As discussed later, these geoproccesing operations are key tools for relief analysis.

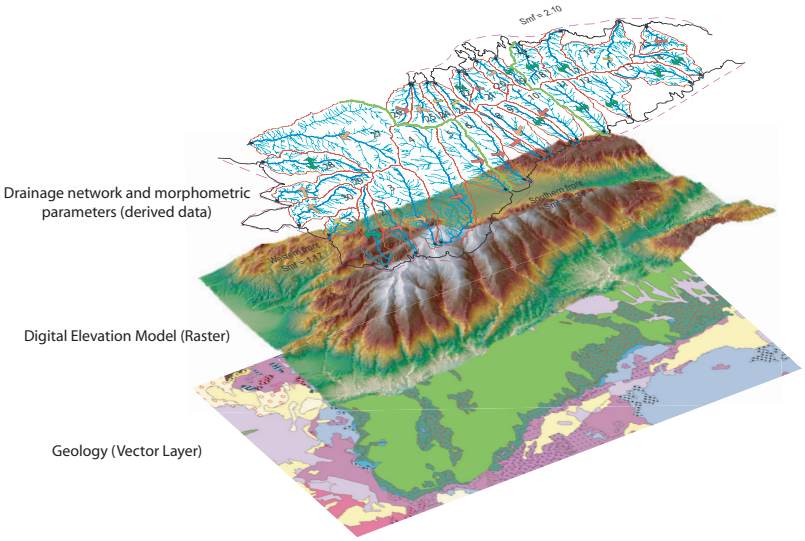

Figure 1. Example of different kinds of GIS layers.

GIS are often associated with a map. A map is, however, only one way to work with geographic data in a GIS and only one type of product generated by GIS. Furthermore, GIS can provide more problem-solving capabilities than simple mapping programs.

GIS can be viewed in three different ways: the database view, the map view and the model view. The database is the common data storage and management framework for GIS data and can be utilized to store, access, relate, and/or manage these data. The map view is a set of intelligent maps and other views that show features and feature relationships on the earth's surface. Maps of the underlying geographic information can be constructed and used as "windows into the database" to support queries, analysis and editing the information. Finally, the model view comprises a set of information transformation tools that derive new geographic datasets from existing datasets. These geoprocessing functions take information from existing datasets, apply analytic functions and store results in new derived datasets (Fig. 2). By combining data and applying some analytic rules, it is possible to create a model that helps to answer specific questions. This GIS capability is a key tool for relief analysis, since they are able to process topographic information obtained from Digital Elevation Models (DEM), constrain model parameters and integrate measured data (as radiometric measurements, geophysical information, etc.).

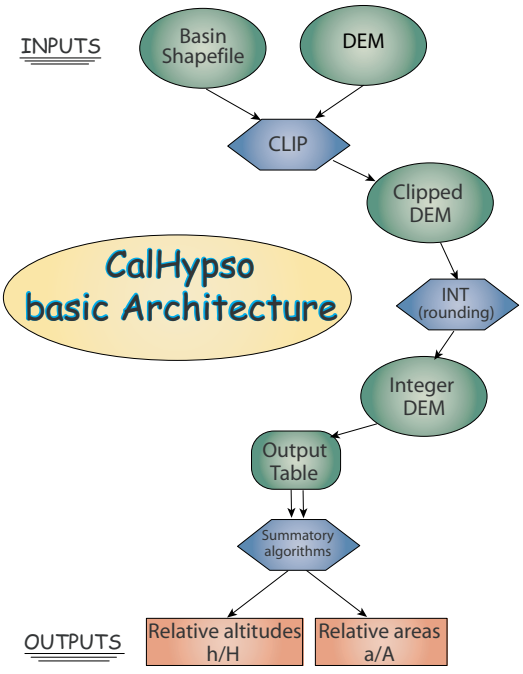

Figure 2. Flow diagram showing a model with the main processes of the CalHypso program (see chapter 4).

The information can be stored in a GIS system as raster or vector format. Raster models emphasize space properties rather than the accuracy of the representation. They store the information in regular cells or pixels representing unique values. Vector models give priority to the accuracy of localization of elements in the space and the representation of elements with defined limits. They use three main objects: the point, the line and the polygon.

1.1.2. Brief history and evolution

Dr John Snow, pioneer of the epidemiology, is considered the first person to create a proto-GIS in 1854. He performed pioneering data analysis to prove his hypothesis that cholera was spreaded via the drinking water (Fig. 3). Some have claimed his Broad Street Map as the first example of GIS, even though it was performed with pen and paper. Although this is an exaggeration, the Broad Street Map is an excellent example of the power of maps to clearly demonstrate relationships in complex scenarios.

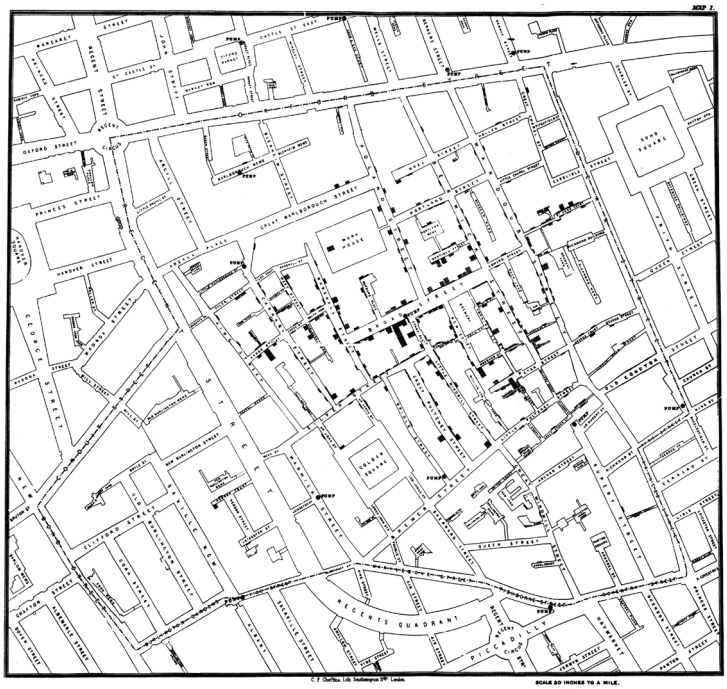

Figure 3. Snow's famous cholera map (London in 1859). Dr. Snow stopped a major cholera epidemic by closing the Broad Street pump, and thus demonstrated that cholera is a water borne disease. This was not previously understood. The map is the most famous and classical example in the field of medical cartography and it is considered the first proto-GIS example.

The evolution of GIS has occurred over a series of stages. The first stage began with the first approximations in the 1950s and lasted until the mid 1970s. It is characterized for individual efforts in development and system applications. The birth of GIS is clearly linked with the development of other programs, such as the computer assistant drawing one (CAD). Institutions and governments created programs and initiatives to solve the problems related to the treatment of geographic information, which were previously solved with manual methods. The USA, Canada and United Kingdom led the first initiatives. The most significant evolutions of GIS were carried out in the USA, though Canada is a world referent in GIS history because of the Canadian Geographic Information System (CGIS) conceived in 1964 and developed since 1966. CGIS was the first to use this name. Noteworthy, among the milestones in the evolution of GIS in the USA is the creation of the Environmental Systems Research Institute (ESRI), as a case of commercial contribution to GIS development. The main contribution of ESRI was the creation of the world standard ArcInfo, which marks a second stage in GIS evolution, namely the "commercial phase", occurred in the 1980s and 1990s. This period is characterized by the interest of big industries related to GIS technologies grew due to the revolution of the informatics. After this commercial phase, GIS began to expand to the "domestic user level" with the development of personal computers. Nowadays, the improvement of computers, together with the expanded use of the internet, allows the distribution of cartography worldwide (Google maps, NASA imaginary, digital terrain models GTOPO30 from the USGS, SIGPAC from the Junta de Andalucía regional government, etc.).

1.2. GIS in geology and tectonic geomorphology

The development of GIS at the end of the last century provided a powerful tool for spatial data analysis and management in almost all the earth science disciplines (mineralogy, structural geology, tectonics, geophysics, geochemistry, etc.). The number of geologic works using GIS has grown exponentially in the last decade. But, GIS is a tool primarily designed for geography, thus requesting some specific applications and skills when applied to geology.

GIS allow not only representing data, but also performing geostatistical analysis and building models. These features make them very useful in earth sciences in general and in geology in particular. For example, GIS in hydrogeology can aid to make complex maps with a lot of information, but also to extract specific information through precise queries. GIS can be used at very different scales, from wordlwide ones (e.g. the hypsometry of the whole earth), to very local ones (statistical analysis in thin sections; Fig. 4).

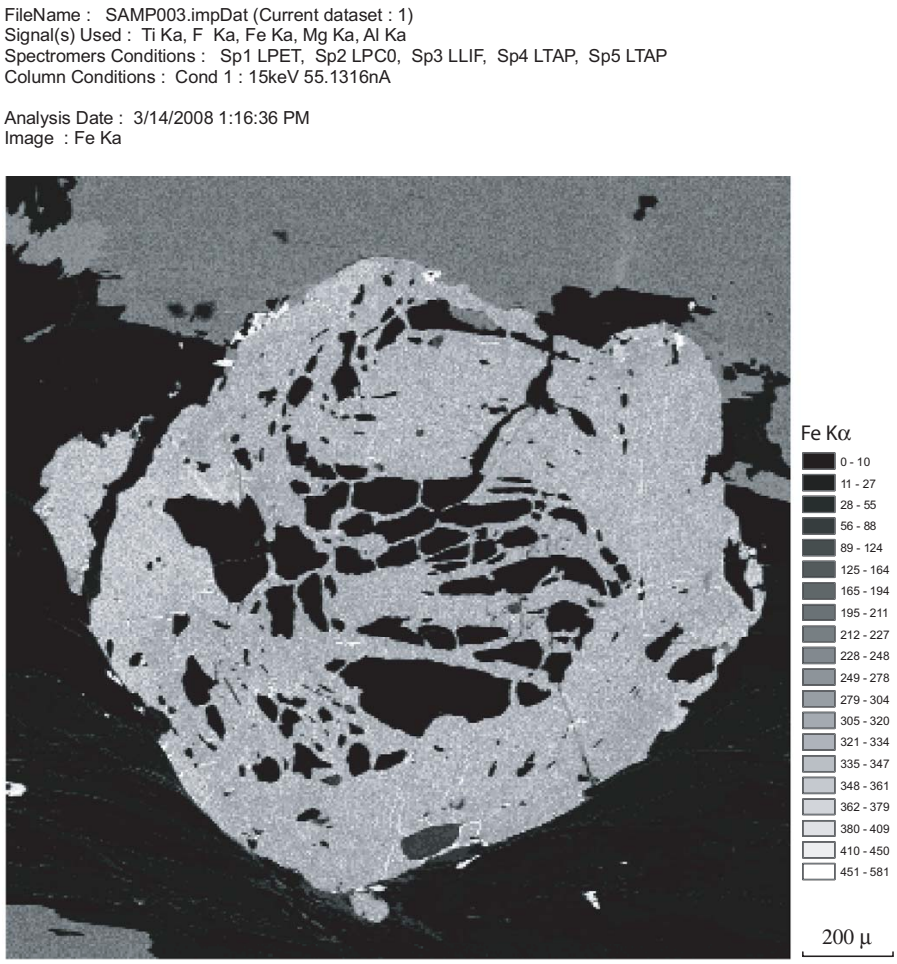

Figure 4. Raster dataset with FeKα intensity values for a garnet porphyroblast acquired by electron microprobe mapping represented in ArcGIS. Since the values are represented in a matrix, it is possible perform geostatistical analysis.

In geomorphology, the traditional use of GIS capabilities can be found in works that require multi-criterium analysis. There is a widespread use of GIS in landslide hazard evaluation (e.g., Carrara et al., 1991 and 1993; Dai and Lee, 2002), flooding hazard maps (Townsend and Walsh, 1998; Liu et al., 2003.), etc. All of these analyses require the combination of different spatial data in conjunction with statistical analysis. These disciplines have benefited from the apparition of Digital Topographic Models (DTM; Fig. 5), which include elevation data at very different scales, bathymetry of marine basins and even data from other planets obtained in spatial missions (Luo, 2002).

In the field of tectonic geomorphology and landscape evolution, the use of GIS is relatively recent. The availability of the aforementioned DEM (Fig. 5), in conjunction with the use of new geochronological methods valuables at time-scales below 1 Ma, has produced a great revolution in this field. DEM have replaced old topographic maps, allowing for better and faster analysis of topographic parameters (Fig. 5). One of the most important features of DEM is the possibility of extracting river networks with stream gradients and catchment areas. Actually, the analysis of drainage networks with the purpose of evaluating recent tectonics has experienced a rebirth, as seen in the number of recent publication on this topic.

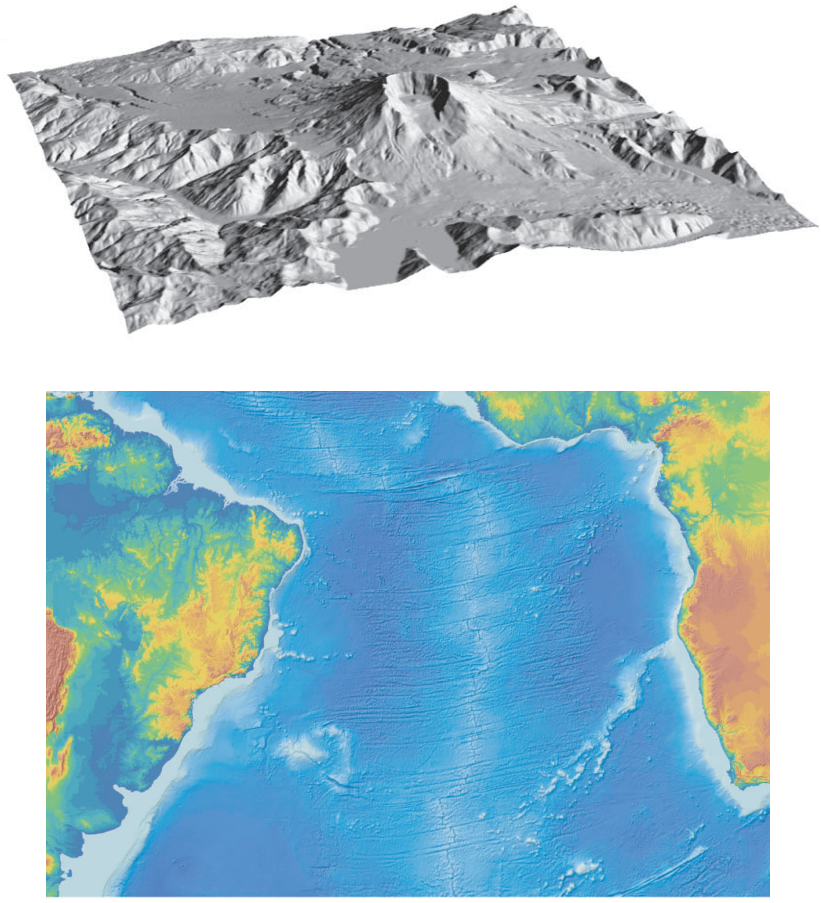

Figure 5. Examples of digital elevation data. **a)** Digital Elevation Model of Mt. St. Helens, Washington State, generated from Shuttle Radar Topography Mission (SRTM-30) digital elevation data (Modified from Finlayson and Montgomery, 2003). **b)** Bathimetric digital model for the Atlantic Ocean generated from GEBCO 97 (IOC-IHO) database (Modified from Bishop, 2008).

2. OBJECTIVES OF THIS THESIS

This thesis aims to present some new GIS tools and methodologies developed to analyze drainage networks with a view to constrain recent tectonic activity. These GIS-based geomorphic tools have been applied to the central part of the Betic Cordillera, an area with moderate present-day seismicity and tectonic activity. Two main features of rivers and catchments, namely river gradients and hypsometry will be the main focus of this study. Chapters 2 and 3 present some new concepts and methodologies that allow a more accurate analysis of river gradients and basin hypsometries by using geostatistic techniques. Chapter 5 presents a new GIS-based method to reconstruct the primary surface morphology of a sedimentary basin prior to be dissected by river entrenchment. The reconstructed surface marking the end of sedimentation, together with present-day topography and numerical ages of initial present-day drainage formation, is used to estimate erosional rate distribution within the basin and evaluate present-day tectonic activity. Chapter 6 is a study of the drainage network and some geomorphic indexes of the highest mountain range in the Betic Cordillera, namely the Sierra Nevada, with the objective of establishing its Quaternary tectonic activity. This chapter shows the application of the GIS-based tools presented in the previous chapters to an area where all of the geological information available suggests the existence of the highest long- (Tortonian to present-day) and short-term (Quaternary) uplift rates.

3. GEOLOGICAL SETTING

3.1. The Betic Cordillera

The Betic Cordillera is the biggest orographic unit in the Southern Iberian Peninsula (Fig. 6). It is bounded to the north by the Iberian Massif and to the south by the Mediterranean Sea and the Atlantic Ocean. However, this cordillera continues below the Alboran Sea to connect with the Rif in northern Morocco forming the Betic-Rif Cordillera, the westernmost Alpine orogenic belt in the peri-Mediterranean region (Fig. 7). The mean altitude for the Betic Cordillera is approximately 800 metres, although in its central part the elevations are higher (Fig. 6). The highest elevations are located in mountain ranges striking East-West (Sierra Nevada, Sierra de los Filabres). The lowest altitudes are located in the Guadalquivir basin.

The Betic Cordillera can be divided in three major domains (Fallot, 1948; Julivert et al., 1974): i) the South-Iberian domain, ii) the Campo de Gibraltar domain, and iii) the Alboran domain. The Betic Cordillera also includes an important volume of Neogene-Quaternary sediments in intra-montane basins.

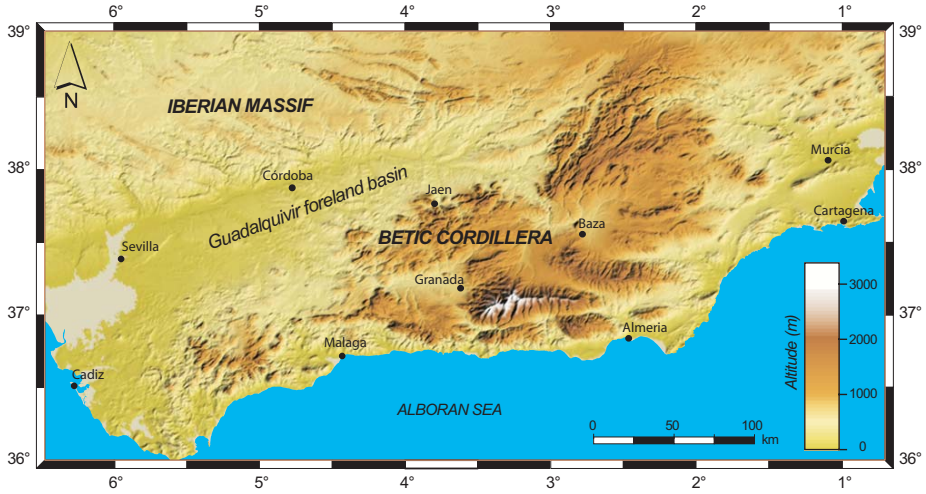

Figure 6. Topographic map of the Betic Cordillera.

3.1.1. South-Iberian Domain (External Zone)

The South-Iberian Domain (García-Henández et al., 1980; Vera, 2001) is formed by Mesozoic and Tertiary sediments that were deposited over the Variscan basement of the Iberian Massif. It constitutes the southern palaeo-margin of Iberia. These sediments are deformed by thin-skinned tectonics, lacking metamorphism and penetrative foliations.

3.1.2. Campo de Gibraltar Domain

The Campo de Gibraltar Domain (Duran-Delga et al., 2000) is formed by deep-water flysch sediments (mainly turbidites) of Cretaceous to Paleogene ages and detached from their substratum, which was probably oceanic crust or thinned continental crust. This domain is located between the Internal and External Zones, showing intense deformation but no metamorphism.

3.1.3. Alboran Domain (Internal Zone)

The Alboran Domain (Balanyá and García-Dueñas, 1988) is is formed by an anti-formal stack of three tectonometamorphic units, which, from bottom to top, are: the Nevado-Filabride (Egeler, 1963), the Alpujarride (Van Bemmelen, 1927) and the Malaguide (Blumenthal, 1927) complexes. The contacts between these units were first interpreted as thrusts, but nowadays they are considered as low-angle normal faults (García-Dueñas et al., 1988; Galindo-Zaldívar et al., 1989; Platt and Visser, 1989; Martínez-Martínez et al., 1997).

The Malaguide complex is formed by a Palaeozoic substratum composed of deep marine sediments of Ordovician-Carboniferous ages and a discordant sediment cover of continental conglomerates and quartzites of Triassic-Lower Miocene ages (Didon et al., 1973). The palaeozoic rocks preserve deformations and metamorphism of Variscan age.

The Alpujarride complex is geographically the most extended unit in the Internal Zone. It occupies the middle position in the stack,and suffered a low- to high-grade Alpine metamorphism. this comples is formed by different superposed units with a similar lithological sequence (Azañón et al., 1994): i) a metapelitic formation composed of graphitic schists and gneisses (Palaeozoic), ii) a succession of schists with inter-bedded quarztites (Permian-Triassic), and iii) a carbonate succession with dolomitic and calcitic marbles (Middle-Upper Triassic).

The Nevado-Filabride complex crops out in the core of the antiforms of the Sierra Nevada and Sierra de los Filabres. It is formed by three different units (García-Dueñas et

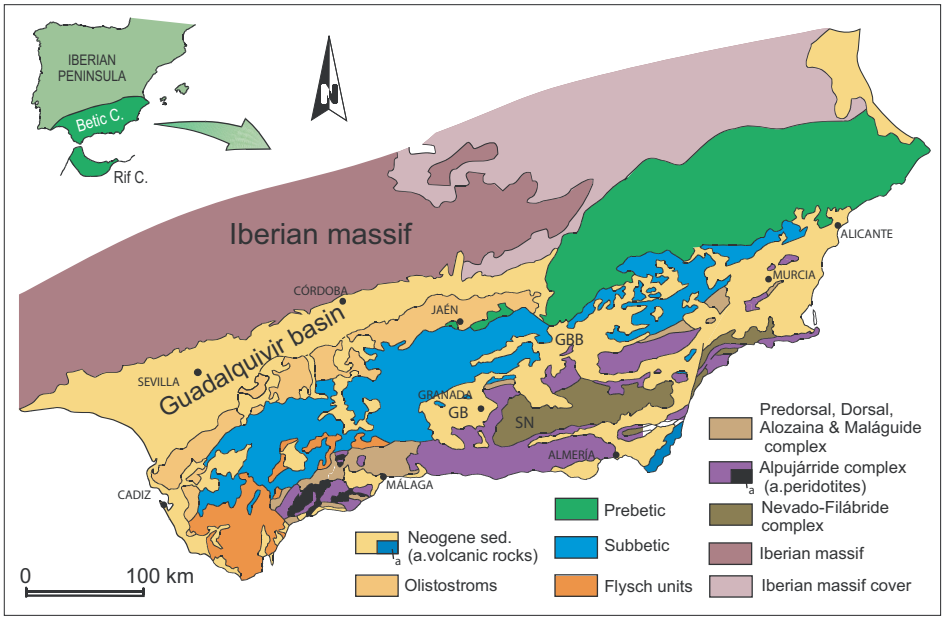

Figure 7. Tectonic map of the Betic Cordillera in the western Mediterranean with the main geological domains (modified from Ruano, 2003).

al., 1988; Martínez-Martínez et al., 2002): Bédar-Macael, Calar Alto, and Veleta unit. These internal units have a lithostratigraphic sequence made up of graphitic schists with quartzites (pre-Permian?), lighted schists (Permian-Triassic?), and marbles (Triassic-Cretaceous?).

3.1.1.4. Neogene-Quaternary basins

During the Tortonian, the sea covered most of the Cordillera. Later uplift produced a series of emergent areas (sierras) separated by sedimentary basins. The largest of these Neogene basins is the Alboran basin, which separates the Betic Cordillera and the Rif.

The basins located in intra-montane depressions show a wide variety of structures and tectonic settings. They are commonly affected by faults and sometimes also folded. These basins were formed in the hanging-wall of a crustal-scale detachment and have been interpreted as piggy-back basins (Jabaloy et al., 1992).

The basins, located in the western sector of the Betic Cordillera (Gulf of Cadiz, Algeciras, Ronda and Alora) are generally affected by tilting and normal faulting. In the cen-

tral sector, the basins generally were formed on open synforms (locally bounded by faults). An example of such kind of basins is the Almazora basin (Pedrera et al., 2009), which developed on an open synform northward of the Sierra de los Filabres antiform. Other basins, such as the Alcalá la Real, Orgiva, and Ugíjar basins, show more complex evolutions. In the eastern Betic Cordillera, most of the basins are controlled by strike-slip fault systems, such as the Sorbas-Tabernas, Vera-Garrucha, Níjar-Carboneras, Lorca, and Totana basins.

The Granada basin and the Guadix-Baza basins, located in the central sector of the Betic Cordillera, are the largest intra-montane basins. The Granada basin is a large half-graben, with a sedimentary record thickening northwards and bounded to the north and east by normal faults dipping to the south and southwest, recpectively (Rodríguez-Fernández and Sanz de Galdeano, 2006). The Guadix-Baza basin developed to the north of the Sierra Nevada antiform (Vera, 1970; Viseras, 1991; Fernández et al., 1996). The Granada and Guadix-Baza basins were opened in upper Pleistocene time to an external drainage towards the Guadalquivir river, having undergone since then different landscape evolutions, which have been partially controlled by Quaternary tectonics as discussed in this thesis.

Finally, the Guadalquivir basin represents the foreland basin of the Betic cordillera, having been formed due to flexure of the lithosphere under the weight of the orogen (Flinch 1996; García-Castellanos et al., 2002). It has an asymmetrical geometry with sediment thicknesses increasing southwards (Iribarren et al., 2007).

3.5. Tectonic models for the Betic Cordillera

The Betic cordillera was formed during the Neogene, in a general Eurasian-African plate convergence setting (e.g., Dewey, 1988; Platt and Vissers, 1989; Jolivet and Faccena, 2000). A late orogenic extension, superimposed on an earlier collisional orogen (e.g., Platt and Vissers, 1989; García-Dueñas et al., 1992; Azañón and Crespo- Blanc, 2000; Martínez-Martínez et al., 2002), was responsible for low- and high-angle normal faults, the formation of the Alboran basin (interpreted as a back-arc basin of the orogen) and the initial development of other Neogene-Quaternary sedimentary basins. This extensional tectonics seems to have occurred simultaneously with a general N-S compressional stress field.

The issue of whether or not extension has ceased is very controversial. For some authors, the extension ceased in the Betic Cordillera and the Alboran basin during the upper Miocene (Tortonian), though thermal subsidence continued in the Alboran basin (Comas et al., 1992 and 1999). However, the existence of active normal faulting, together with the distribution of the seismicity and the focal mechanism solutions, reveals present-day

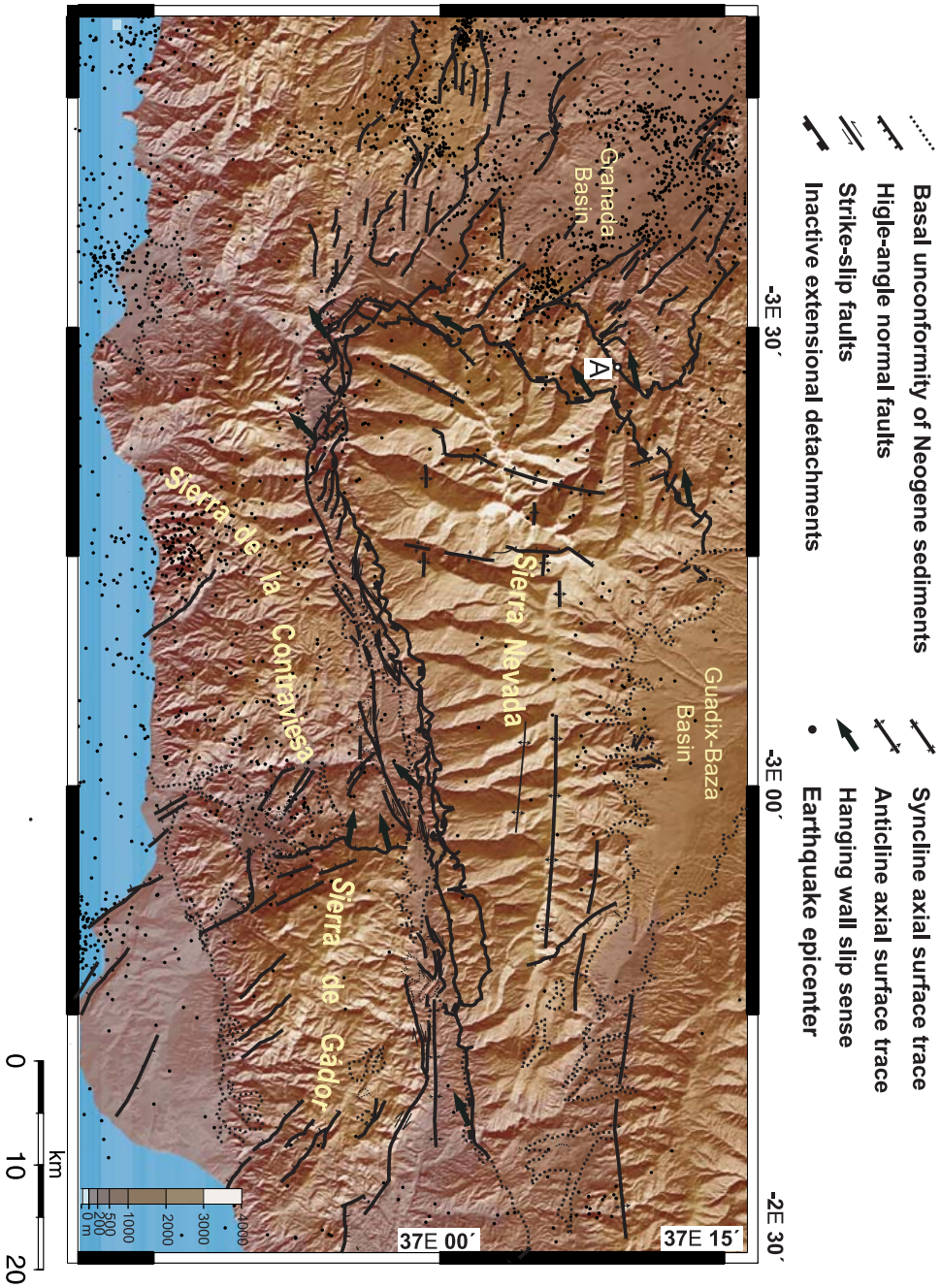

Figure 8. Neotectonic and seismotectonic map of central Betic Cordillera. Small black dots represent earthquake epicenters. (Modified from Martínez-Martínez, et al., 2006).

extension in the upper crust (Morales et al., 1997; Galindo-Zaldívar et al., 1999; Muñoz et al., 2002; Stich et al., 2003; Buforn et al., 2004). Some authors interpret this extension to be coeval and perpendicular to the regional compressional setting established since late Tortonian (Galindo-Zaldívar et al., 2003; Martínez-Martínez et al., 2006.

3.2. Active tectonics and Quaternary landscape evolution in the Central Betic Cordillera.

The topographic configuration of the internal zone of the Betic Cordilleras is characterized by a series of alternating mountain ranges (up to 3,400 m high) and topographic depressions. The mountain ranges are composed of Palaeozoic–Mesozoic metamorphic rocks, while the topographic depressions correspond to basins filled with Neogene–Quaternary sediments. Tectonics has been a major controlling mechanism on landscape development. Tectonic uplift started in late Miocene time, provoking the progressive exhumation of both the sierras and the sedimentary basins. The uplift seems to be controlled by large-scale E-W trending open folds, which, in turn, are related to a dominant N–S compression. This compression is a regional phenomenon related to ongoing collision between the African and Iberian plates which converge in a NW-SE direction at approximately 5 mm/yr (Argus et al., 1989; de Mets et al., 1994).

Apart from the large-scale open folds, high-angle normal faults have played an important role in landscape evolution. Quaternary normal faults and a relatively high concentration of earthquake epicenters characterize two main areas of active extension in the central Betic Cordillera (Fig. 8). The first one corresponds to the Granada basin, where high-angle NW–SE striking normal faults are predominant, but E–W and NE–SW normal faults also occur locally (Galindo-Zaldívar et al., 1999; Muñoz et al., 2002). Evidence for the activity of both E–W and NW– SE oriented normal faults is well documented from seismicity and offset of Holocene sediments (e.g. Alfaro et al., 2001; Reicherter et al., 2003; Azañón et al., 2004). The NW– SE striking faults form a segmented system with the en-echelon normal faults linked by relay ramps or transfer faults. The second area of active extension is found to the west of the Sierra de Gádor, where N–S to NW–SE oriented high-angle normal faults delimit two large-scale eastward-tilted blocks. Pliocene and Pleistocene sediments are tilted by some of these faults, which control Holocene fluvial sedimentation (Martínez-Díaz and Hernández-Enrile, 2004; Marín-Lechado et al., 2005).

2

Spatial analysis of stream power using GIS: SLk anomaly maps

J. V. Pérez-Peña [(1)]*, J. M. Azañón [(1, 2)], A. Azor [(1)], J. Delgado [(3)] and F. González-Lodeiro [(1)]

(1) Departamento de Geodinámica, Universidad de Granada, Granada, Spain
(2) Instituto Andaluz de Ciencias de la Tierra (UGR-CSIC)
(3) Departamento de Ingeniería Cartográfica, Geodésica y Fotogrametría, Universidad de Jaén, Jaén, Spain
* Correspondence to: JV Pérez-Peña, Departamento de Geodinámica, Campus Fuentenueva s/n, Universidad de Granada, 18071 Granada, Spain. E-mail: vperez@ugr.es

ABSTRACT: The stream length-gradient index (SL) shows the variation in stream power along river reaches. This index is very sensitive to changes in channel slope, thus allowing the evaluation of recent tectonic activity and/or rock resistance. Nevertheless, the comparison of SL values from rivers of different length is biased due to the manner in which the index is formulated, thus making correlations of SL anomalies along different rivers difficult. Therefore, when undertaking a comparison of SL values of rivers of different length, a normalization factor must be used. The graded river gradient (K) has already been used in some studies to normalize the SL index. In this work, we explore the relationships between the graded river gradient (K), the SL index, and the stream power, proposing the use of a re-named SLk index, which enables the comparison of variable-length rivers, as well as the drawing of SLk anomaly maps. We present here a GIS-based procedure to generate SLk maps and to identify SLk anomalies. In order to verify the advantages of this methodology, we compared a SLk map of the NE border of the Granada basin with both simple river profile-knickpoint identification and with a SL map. The results show that the SLk map supplies good results with defined anomalies and suitably reflects the main tectonic and lithological features of the study area.

Keywords: Geomorphic indices; Rivers; Tectonic geomorphology; SLk maps; GIS

Earth Surface Processes and Landforms (2009)
DOI: 10.1002/esp.1684
Received 18 May 2006
Revised 28 January 2008
Accepted 7 February 2008

1. INTRODUCTION

The analysis of drainage networks is a powerful tool to detect recent tectonic activity and uplift (e.g. Ouchi, 1985; Clark et al., 2004) as river channels are very sensitive to changes in the parameters that control their shapes and gradients (e.g. Whipple and Tucker, 1999; Korup, 2006). Climate changes, tectonics, and lithology affect river equilibrium conditions and, hence, river geometry (e.g. Jackson and Leeder, 1994; Schumm et al., 2000; Burbank and Anderson, 2001; Keller and Pinter, 2002).

A river is in dynamic equilibrium when erosion keeps pace with sedimentation and under these conditions a river can be considered to be graded (Mackin, 1948; Leopold and Maddock, 1953; Schumm et al., 2000). Field observations and theoretical calculations show that river networks approach equilibrium over a long period (10^4–10^6 yr), even in tectonically stable areas (Knox, 1976; Pizzuto, 1992; Brookfield, 1998). Nevertheless, rates of response increase exponentially from equilibrium and, therefore, gross deviations from equilibrium (when related to changes in uplift rates) must reflect relatively recent events (Brookfield, 1998; Bull, 1991). In bedrock rivers, adjustment to new equilibrium conditions is reached by changes in the incision rate, which is thought to be a function of either shear stress (Howard and Kerby, 1983) or total stream power (Summerfield, 1991; Finlayson and Montgomery, 2003). Morphologically, changes in incision rates along a river produce changes in river gradient.

The stream length-gradient index (or SL index) (Hack, 1973; Keller and Pinter, 2002) highlights gradient changes in river channels. This geomorphic index is very sensitive to changes in lithology and/or tectonic uplift. Hence, SL variations have been recognised as a useful reconnaissance tool in tectonically active areas for many years (Hack, 1973; Seeber and Gornitz, 1983; Merritts and Vincent, 1989; Brookfield, 1998; Carvajal and Sanz de Galdeano, 2001; Azor et al., 2002; Chen et al., 2003; Pérez-Peña et al., 2004, Goldrick and Bishop, 2007). Most of these studies were based on comparisons of SL profiles along different rivers. However, the fact that the SL index is strongly influenced by river length makes comparing SL values in rivers of different length difficult. To overcome this problem, some authors have proposed using the graded river gradient (K) as a normalization factor for the SL index (Seeber and Gornitz, 1983; Chen et al., 2003).

In this work, we examine the use of K as an SL normalization factor, as well as the relationships between the graded river gradient, the SL index, and stream power. We present a GIS-based methodology to extract normalized stream-length maps. We have focused this work on the following goals; a) to present the advantages of "graded gradient norma-

lization" with regard to river power, and b) to combine different approaches using GIS and geostatistical analysis to obtain a valuable anomaly stream-length map. Our analysis centres on the northeastern border of the Granada basin area (Betic Cordillera, SE Spain), where we have compared a normalized stream-length map against a stream-length map and against a knickpoint analysis.

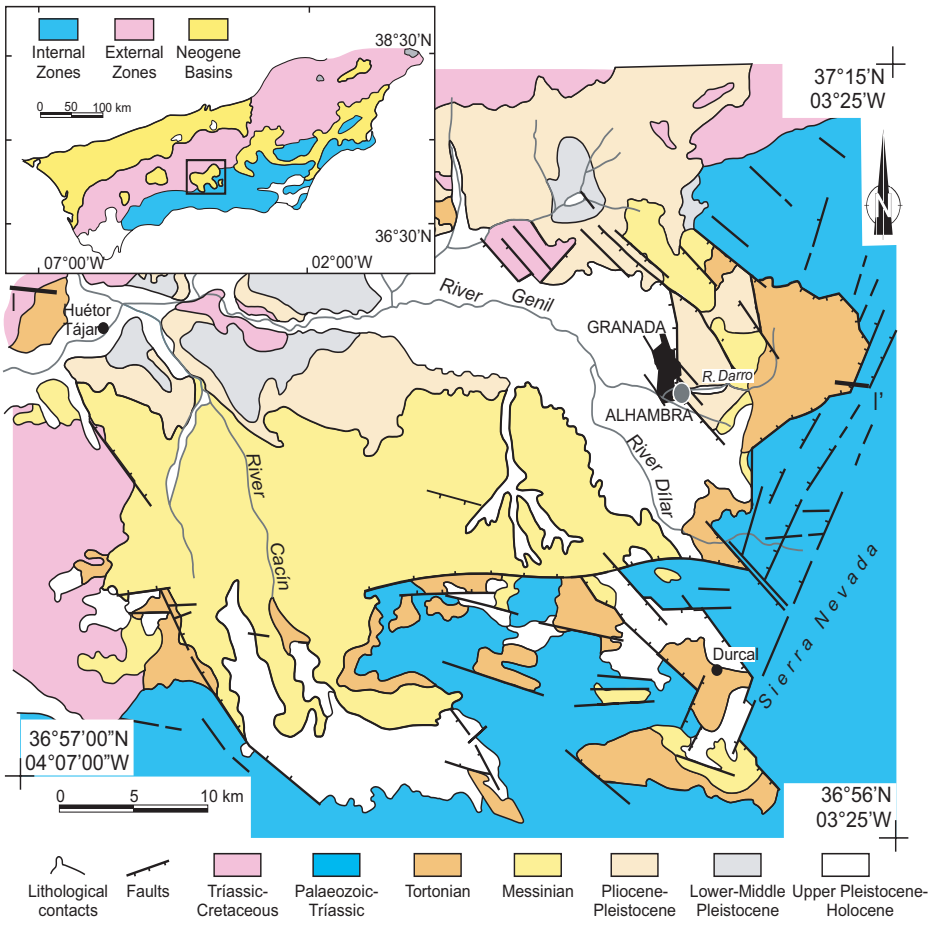

Figure 1. Geological sketch of the Granada basin. Inset shows its location within the Betic Cordillera.

2. GEOLOGICAL AND GEOMORPHOLOGICAL SETTING OF THE GRANADA BASIN

The Granada basin (Fig. 1) is located within the Betic Cordillera (SE Spain), which is the result of the collision between the African and Eurasian plates, with present-day convergence rates of approximately 5 mm/yr (de Mets et al., 1994). This convergence is responsible for a NW-SE compression with associated NE-SW extension that is accommodated by normal faults (Sanz de Galdeano, 1980; Galindo Zaldívar et al., 1999; Azañón et al., 2004; Rodríguez-Fernández and Sanz de Galdeano, 2006). Most of these faults have been active since the Pleistocene and have low to moderate (≤5Mb) associated seismicity (Sanz de Galdeano et al., 2003). The basin comprises Neogene–Quaternary sediments lying over the NE-SW striking contact between the External and Internal zones of the Betic Cordillera. Schist, phyllites, and marbles of Palaeozoic to Mesozoic age, and sedimentary rocks of Triassic to Cretaceous age form the basement of the Granada basin. The sedimentary fill is up to 2 km thick (Rodríguez-Fernandez and Sanz de Galdeano, 2006).

The present-day relief and the drainage pattern of the NE margin of the Granada basin are strongly influenced by the local tectonics. The most prominent morphological features are two fault-generated mountain fronts that form conspicuous breaks in the landscape (Azañón et al., 2004) (Fig. 2a). The first front is located between the metamorphic basement and the sedimentary infilling of the Granada basin. This mountain front is formed by NW-SE striking normal faults that change northwards to strike NNE-SSW (Fig. 2a). The present-day activity of this front is still in contention due to its strong lithologic controls and the lack of seismicity observations. Therefore, the study of the drainage network may be a useful tool to determine possible activity of this mountain-front. The second front is located between the Tortonian to Pliocene basin-margin sediments and the Quaternary sediments of the current floodplain of the Genil river (Fig. 2a). This mountain front is thought to be a product of the Granada fault (Sanz de Galdeano et al., 2003), which is a normal fault with associated moderate–low seismicity, although it lacks well-exposed fault scarps. Between these two mountain fronts, the drainage network consists of rivers deeply incised into the Tortonian to Pliocene sediments and therefore flowing over bedrock (Fig. 2a). Southwest of the Granada fault, the rivers scarcely incise into Upper-Pleistocene to Holocene sediments and consequently flow over their own alluvium deposits.

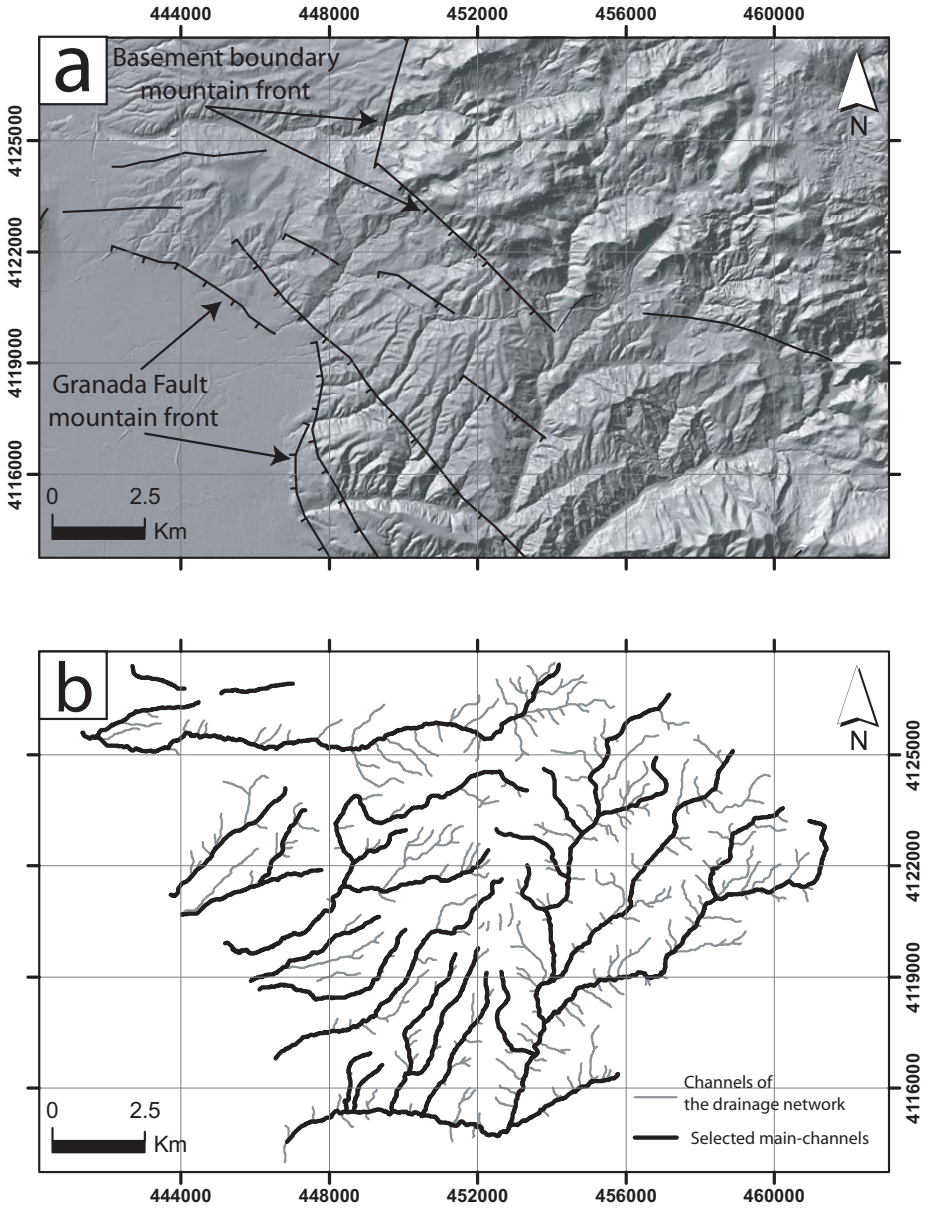

Figure 2. a) Shaded relief map of study area (NE border of Granada basin). This map was extracted from a DEM with 10 m of pixel resolution. **b)** Detailed drainage network of the study area. The main channels used for the analysis are indicated.

3. METHODOLOGY

3.1. Stream-length gradient index and stream power

The SL index in a river reach is defined as follows (Hack, 1973; Fig. 3a):

$$SL = \frac{dh}{dl} L \quad (1)$$

Where dh/dl is the slope or gradient of the reach (dh is the change in elevation and dl is the length of the reach) and L is the channel length upstream from the midpoint of the reach to the river head.

The SL index can be deemed as a proxy to the stream power per unit length (Ω). The stream power per unit length (Ω), measured in W/m is defined as (Summerfield, 1991):

$$\Omega = \gamma Q s \quad (2)$$

Where γ is the unit weight of water per unit length (9800 N/m^3), is the discharge (m^3/s), and s is the slope of the water surface, which is generally approximated by the slope of the channel bed. If uniform climatic factors can be assumed (i.e. that rainfall and evapotranspiration do not vary within the study area), then discharge can be related by means of a power law to drainage area (A) as:

$$Q = aA^b \quad (3)$$

Where a and b are positive constants (Finlayson and Montgomery, 2003; Jain et al., 2006).

Hack (1957) showed that A and L are related by means of an empirically calibrated power relation, namely Hack's law:

$$L = 1{\cdot}4\, A^{0{\cdot}6} \quad (4)$$

Many other works have corroborated this power relation and, although the exponent in Equation (4) varies in different areas and in basins of different size, it is generally accepted to be slightly below 0.6 (Rigon et al., 1996).

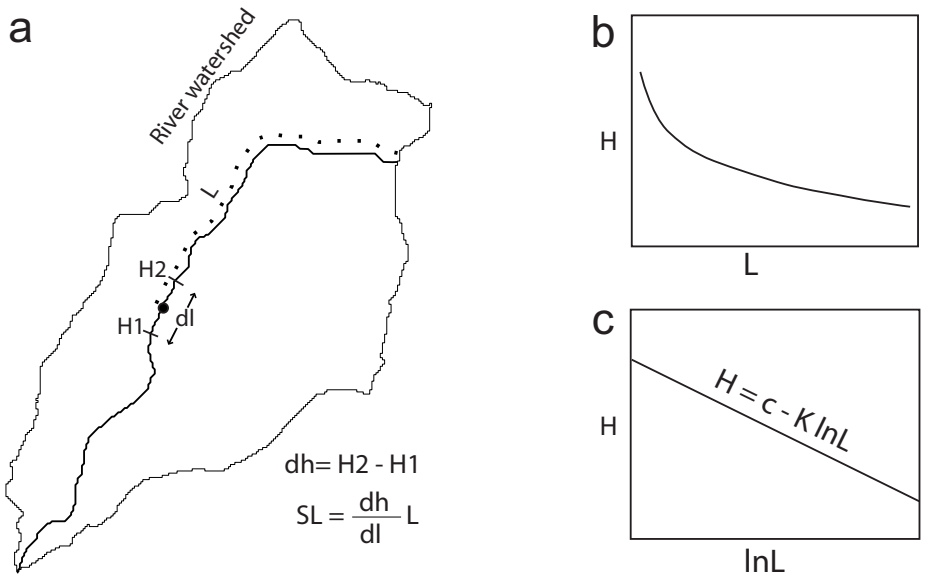

Figure 3. a) Schematic diagram showing SL index calculation according to Keller and Pinter (2002). **b)** Idealized concave-shaped profile for a graded river. **c)** Plot of the idealized profile in a semi-logarithmic scale.

From Equations (3) and (4), we can express discharge as a function of L (Jain et al., 2006):

$$Q = cL^{d} \tag{5}$$

Where c and d are empirical constants for the area.

Equation (5) allows us to rewrite Ω as a function of L

$$\Omega = \gamma cL^{d}s \tag{6}$$

And, as the slope is

$$s = \frac{dh}{dl} \tag{7}$$

we can relate the SL index to the stream power per unit length as

$$\Omega = SL\gamma cL^{d-1} \tag{8}$$

Since γ, c, and d are constants, the SL index and Ω are directly proportional.

3.2. Rivers in equilibrium conditions

A river can be considered graded when the gradient, width, and depth are in dynamic equilibrium with discharge and load (Mackin, 1948). Graded rivers typically develop a smooth concave profile and, hence, a semi-logarithmic plot of those profiles will yield a straight line (Fig. 3b) (Hack, 1973; Brookfield, 1998; Chen et al., 2003):

$$H = C - k\ln(L) \tag{9}$$

Where H is the elevation above a given datum, L is the length from the river head, C is the river head elevation, and k is the slope of the line. The derivation of this equation with respect to L (Burbank and Anderson, 2001) yields the following formula for the stream slope, s:

$$s = \frac{dh}{dl} = \frac{d(k\ \ln(L))}{dl} = \frac{k}{L} \tag{10}$$

Thus, parameter k has the same formulation as the SL index since it is a product between slope and river length, and it can be used to characterise either an entire river profile or any reach of it. When this parameter is applied to the whole river profile, it is referred to as K. This graded river gradient represents the equilibrium conditions for a given river:

$$K = \frac{C - h_f}{\ln L_t} \tag{11}$$

Where hf is the elevation at the river mouth and Lt is the total length of the river.

As K represents the SL index calculated for the entire river (Equation (10)), it will correlate with the total (or available) stream power (Ω_T):

$$\Omega_T = K\gamma c L_t^{d-1} \tag{12}$$

Where L_t is the total river length.

4. STREAM-LENGTH ANALYSIS

4.1. K- Ω_T relationship for the study area

In order to empirically calibrate the K-Ω_T relation, we have calculated these two parameters for each river. To obtain the total stream power Ω_T, the discharge Q must be correlated with the upstream area A (Equation (3)). In our study area, there is no gauging discharge data to perform a regression analysis and, consequently, we have to use empirical values to estimate parameters a and b of Equation (3). Previously published values of these coefficients are around 0.7 for b and around 1 for a (Jain et al., 2006; Finlayson and Montgomery 2003; Dunne and Leopold, 1978). The plot of K versus Ω_T shows a good correlation using the a and b values mentioned above (Fig. 4a). However, as we know that K and Ω_T have a direct correlation, we can re-calibrate the a and b parameters without using discharge measurements. It is worth remarking that K has been calculated with river slope and length data, whereas Ω_T has been calculated with river slope and area data. The best values will be those providing the best fit between K and Ω_T. For this purpose, we have calculated Ω_T iteratively with values of b between 0.4 and 0.8 (with a step of 0.01) and with values of a between 0.1 and 2 (step of 0.01), and tested the relation with K values for the rivers. The best fit between Ω_T was obtained with a=0.98 and b=0.62 (Fig. 4b). These parameters offer a better discharge-area proxy for our study area.

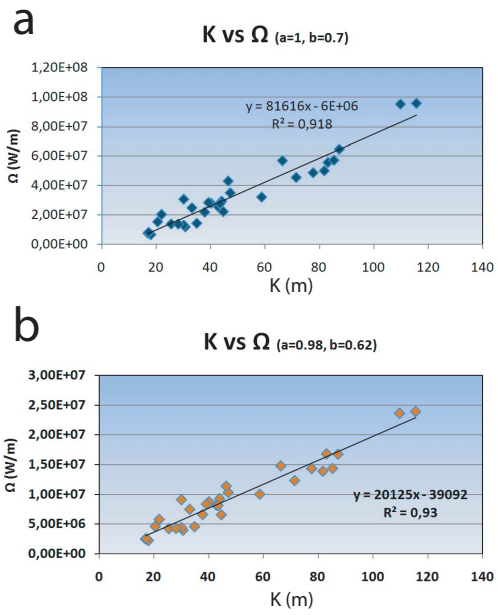

Figure 4. a) K versus Ω_T for rivers in the study area. Ω_T has been calculated with the area-discharge proxy; **b)** K versus Ω_T for rivers in the area, in which Ω_T is calculated with the calibrated area-discharge proxy; $Q = 0.98A^{0.62}$.

4.2. SLk analysis

4.2.1. Selection of river channels

The drainage network for the analysis was extracted from a Digital Elevation Model with 10 m pixel resolution (Fig. 2a). We computed for each DEM cell a single flow drainage direction using the D8 (8-directions) method (O'Callaghan and Mark, 1984). This method assigns flow from each grid cell to one of its eight neighbours, either adjacent or diagonal, in the direction of the steepest downward slope. We selected a threshold area of 0.5 km^2 in the flow accumulation to obtain the final drainage network. From this drainage network, we have selected 28 main channels to perform the stream-length analysis (Fig. 2b).

Alluvial channels behave differently and, as a result, have different equilibrium parameters than bedrock channels (Schumm et al., 2000; Burbank and Anderson, 2001). Consequently, stream-length anomalies could reflect different factors in these two channel types. In this work, we focus northeastwards of the topographic front of the Granada fault, where the channels are incised into bedrock.

The correct determination of the river head (C in Equation (9)) plays a crucial role for K estimation and, therefore, for SL normalization. When the drainage network is extracted from a DEM, it is difficult to correctly estimate the river head. In order to apply a homogeneous criterion to all rivers and avoid subjectivity, we have assumed the river heads to be on the watershed divide. Therefore, we have projected the heads of selected trunk channels to the local watershed divide following the steepest path upstream. This path upstream was also derived by using the D8 algorithm.

4.2.2. SLk map

A brief methodology to produce SL maps was proposed by Keller (1986) and Keller and Pinter (2002). This methodology was designed to work essentially with large-scale topographic maps (1:50,000 to 1:250,000). One disadvantage derives from the fact that this methodology takes as dh (Equation (1)) the contour line equidistance, providing in consequence an irregular distribution of SL values with higher point density near river-heads, where the contour lines are more closely spaced. Geostatistically, constant point spacing will yield better results in the interpolation of values in a horizontal plane. Moreover, the comparison of SL values from rivers of different length, without prior normalization, provides non-weighted results.

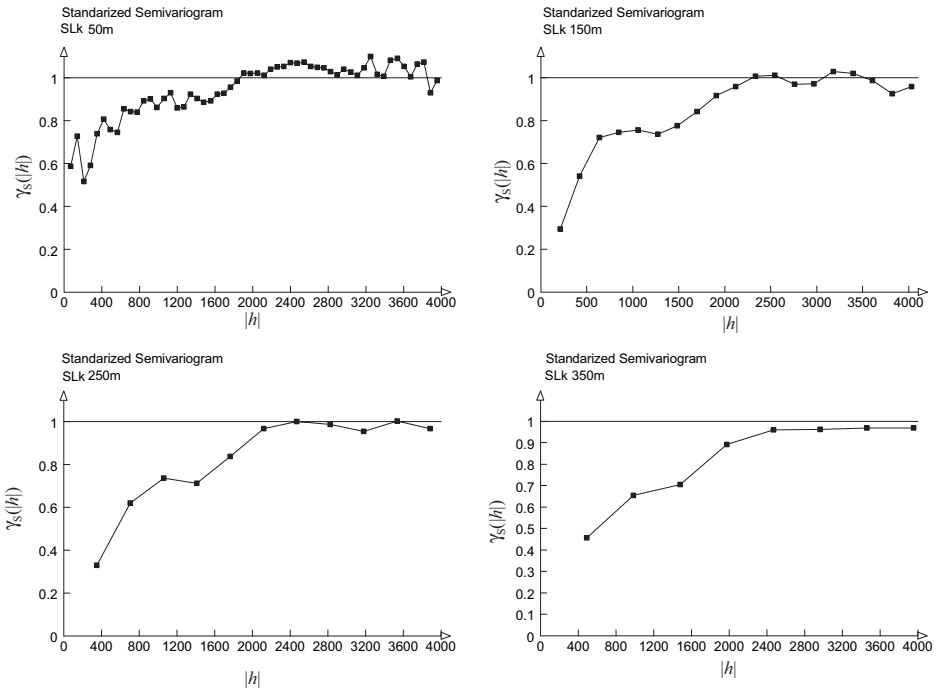

Figure 5. Standardized semivariograms for SLk data calculated with different point spacing (50, 150, 250, and 350 m).

To obtain constant value spacing within rivers, dl (Equation (3)) must be fixed. This dl represents density of data because it marks the distance between values, and it must be defined according to the features (basically, spacing and accuracy) of the digital elevation model. If the spacing is too small, the errors associated to the DEM can introduce noise in the SLk value distribution. For this reason, in order to avoid these errors this distance needs to sufficiently exceed that of DEM resolution.

In order to determine the optimum spacing for the study area, four segment lengths have been used (50, 150, 250, and 350 m) to obtain SLk data for the 26 streams. In order to test the autocorrelation of the data and choose the optimal segment length for the SLk data, four variograms have been calculated considering the different segment lengths (Fig. 5). This approach has been applied in a 2-D space and all the variograms obtained produce quite similar results (except the one with 50 m spacing), indicating that the results are geostatistically robust. The noise in the variogram made with 50 m spacing is due to the error associated with the DEM accuracy that produces a nugget increase (local-scale discontinuity). On the basis of this variogram analysis, we can conclude that the SLk variable shows

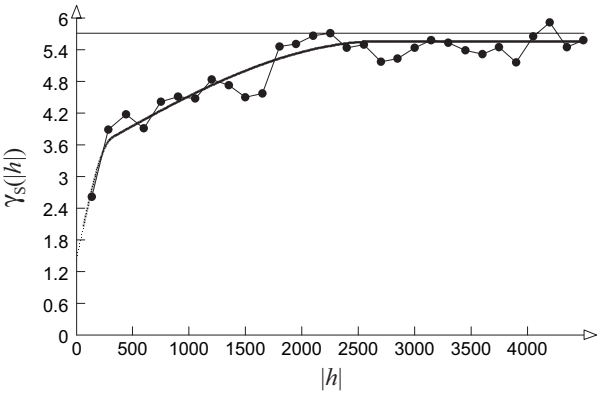

Figure 6. Omnidirectional variogram for SLk data calculated with 150 m spacing.

a considerable autocorrelation structure. Finally, we have used the 150 m spacing because this distance does not present the noise visible in the 50 m spacing variogram and provides more data in order to analyse the anomalies.

Once the spatial variability structure of the SLk variable has been characterised by means of the variogram functions, it is possible to estimate the SLk values in an unmeasured location. For the estimation, we have used the ordinary kriging method considering these variogram models (Fig. 5). Nevertheless, the procedure used in anomaly detection (and characterization) is based on the cross-validation method (Davis, 1986; Journel, 1986; Isaaks and Srivastava, 1987). Using cross-validation, the anomalies have been detected by comparing the real values (experimental data) with local estimated data (obtained by kriging and logically affected by the smoothing effect). It is important to point out that the cross-validation methodology has traditionally been used for anomaly detection (geochemical, geophysical, etc.).

4.2.3. Identification of SLk anomalous values

In order to characterise SLk anomalous values, we have performed a cross-validation analysis using ordinary kriging (Goovaerts, 1997). Of course, the usage of any estimation procedure introduces a smoothing effect that could introduce undesirable effects in our dataset. In order to circumvent this smoothing, we have used a cross validation analysis. The cross-validation analysis is a well-known geostatistical method for the characterisation of anomalous values. It consists in removing each data location from the data set, one at a time, and re-estimating its value from the remaining data by using the semivariogram model. The estimates are compared to the original observations in order to establish whether the data are coherent with their neighborhood or not (anomalous data). This comparison is

established in a probabilistic approach using a Z-score parameter. This Z-score parameter is defined as the estimation error divided by the standard kriging deviation. By using only the estimated data as a base map to present the anomaly detection results, the effect of the smoothing is reduced and therefore is less crucial.

To apply the cross-validation method, a semivariogram of the SLk values (150 m spacing) has been obtained. The SLk values show good corregionalization and isotropic behaviour in the four main directions considered (N-S, NE-SW, E-W, NW-SE), with an angular tolerance of 22.5º. Therefore, the omnidirectional variogram has been used (Fig. 6). This variogram has been fitted to a theoretical model composed of three imbricated structures: a) a nugget effect equal to 1.45; b) a spherical structure with a range equal to 315 m and a sill of 1.914; and c) a spherical structure with a range equal to 2,700 m and a sill of 2.204. The resulting model shows three different variation scales: a nugget effect (local variability) due to the DEM errors and spacing that represents 26% of the total variance, a medium scale (300 m) that represents 34% of the total variance, and a regional scale (2,700 m) that represents 20% of the total variance. Using this variogram model, the cross-

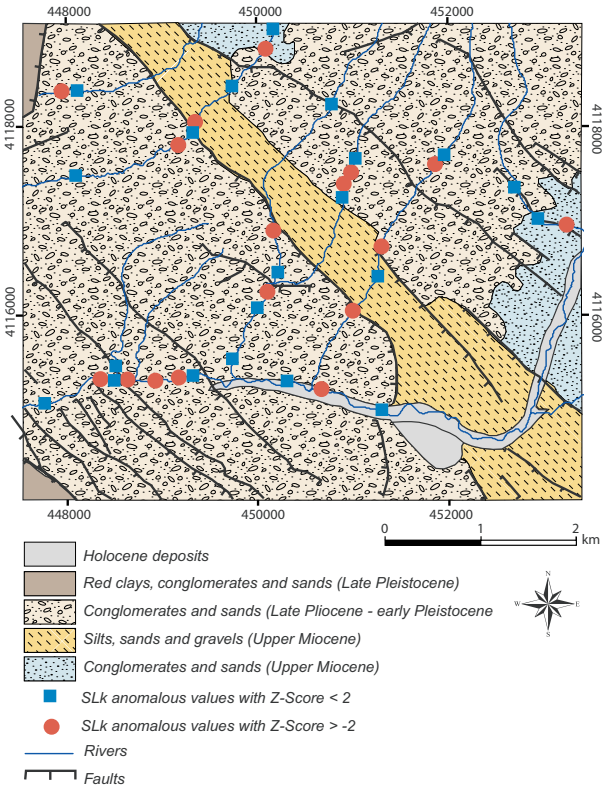

Figure 7. Detailed geological map of area NE of Granada city with the location of anomalous SLk data values

validation analysis with ordinary kriging has been carried out considering a 500 m search radius and the minimum number of data to make the estimation.

5. DISCUSSION

5.1. Limitations of geostatistical analysis

One essential advantage of geostatistics is the capability of quantifying any prediction errors, but it is important to point out that the prediction errors obtained from this geostatistical estimation procedure are theoretical and, as a result, any correlation with real anomalies may not be straightforward. The problem arises with the kriging variance, since it is not conditional on the data values used. This variance is only the average over all possible realizations of the n-data. If the configuration of the n-data estimated at many different places were the same, then the kriging variance would be an estimate of the variance of the L errors. Because of the averaging over the L realizations of data values, the kriging variance obtained is only geometrical. In this sense, the kriging variance is only a ranking index of data geometry (and size) and not a measure of the local spread of errors (Journel, 1986; Deutsch and Journel, 1992; Goovaerts, 1997).

5.2. Relations of anomalous SLk values to lithology and tectonics

In order to interpret anomalous SLk values, a detailed study has been undertaken in a small area northeast of the city of Granada (S Spain; Fig. 7). A detailed map showing the main faults and lithological contacts is available for this zone (Azañón et al., 2004), allowing us to superpose the anomalous SLk values (Z-score absolute value higher than 2) obtained from the cross-validation process onto the geological map of the area.

In this study, 230 SLk values were obtained, with 38 anomalous data according to the Z-score absolute limit value of 2. Figure 7 shows the relationship between the anomalous data and the presence of lithological contacts or faults. We have performed a geostatistical analysis to relate the anomalous data with the linear features representing faults and lithological contacts. We have found that 81% of the anomalous values are located at a distance less than 150 m from a lithological contact or fault. This fact shows that the anomalous SLk data have a clear correlation with tectonic (faults) and lithological contacts of formations with contrasting resistance to erosion.

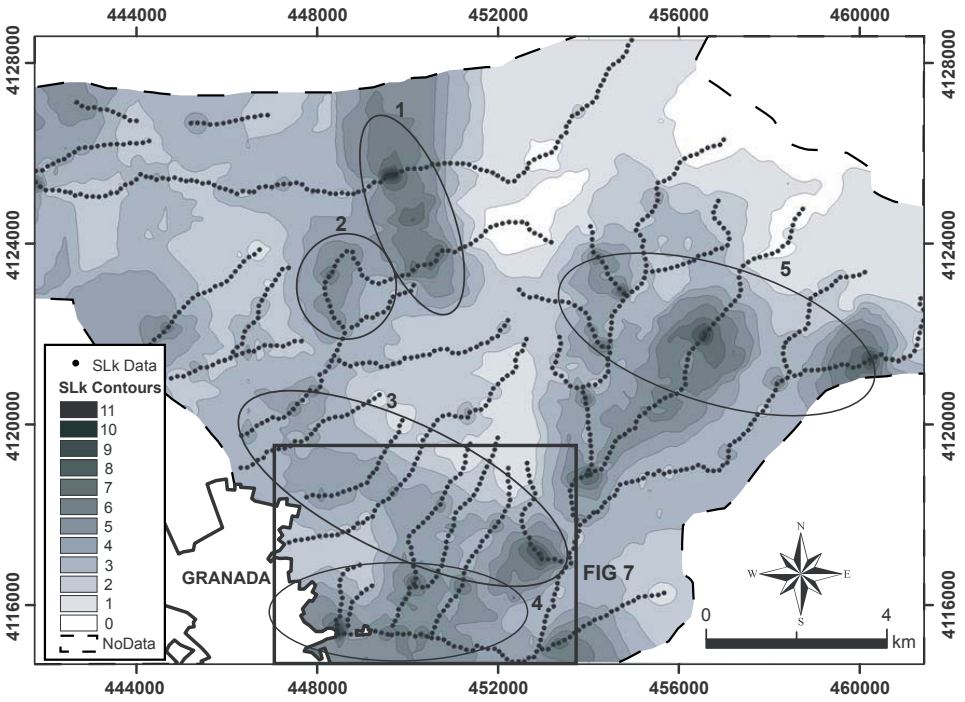

Figure 8. SLk map for the NE border of the Granada basin obtained with a fixed dl of 150 m. The main anomalies are highlighted and numbered (see text). The inset shows the location of Figure 7.

5.2.1. Significance of the SLk anomalies

Anomalies 1 and 5 (Fig. 8) correspond to the tectonically controlled border of the Granada basin. The sediment infilling of the basin is more easily eroded by the drainage network than the crystalline basement. Therefore, these two anomalies are influenced by both lithological and tectonic factors, although the two effects cannot be separated.

Anomaly 2 is constrained to an arc-shaped diversion in the Arroyo del Puerto Stream (Fig. 8), which has been related to a capture process (Carvajal and Sanz de Galdeano, 2001). River piracy may cause changes in local base level and, hence, in channel gradient, thus generating high SLk values.

East of Granada city, anomaly 3 (Fig. 8) matches very well with a Middle Miocene siltstones that crops out from hard Pliocene–Pleistocene conglomerates (Fig. 7). This silty formation is bounded southwards by normal active faults with some associated seismicity (Sanz de Galdeano, 1980; Peláez Montilla et al., 2001; Sanz de Galdeano et al., 2003).

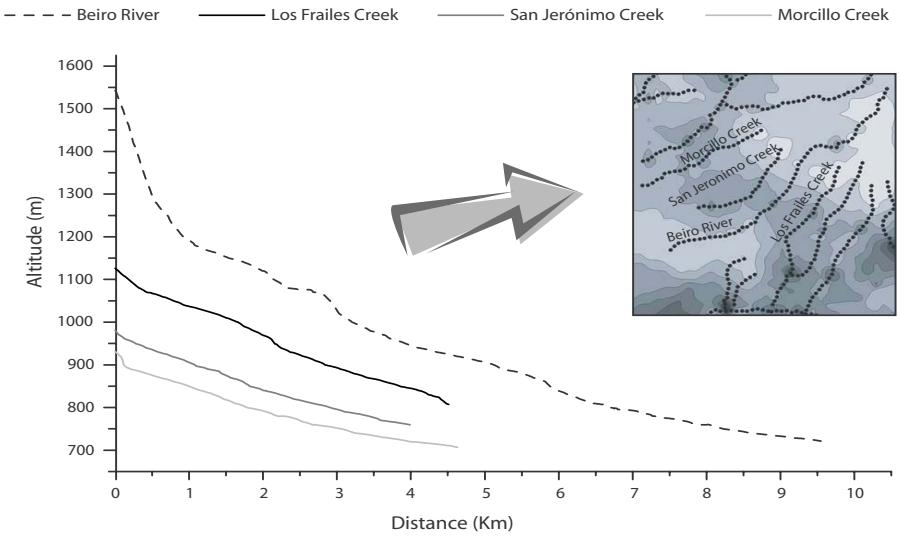

Figure 9. Longitudinal profiles of rivers defining anomaly 3 in Figure 8; the knickpoints are well defined in the Beiro River but not in shorter rivers.

The most prominent features indicating fault activity are changes in river gradients, which are not related to lithological changes or river piracy. This is well discernible southeast of Granada (anomaly 4) (Fig. 8), where high SLk values are depicted. These high values are located within the same materials (Fig. 7) in an area with documented present-day fault activity; these faults have been active throughout the Holocene and could be responsible for historical earthquakes (Azañón et al., 2004).

5.3 Advantages and limitations of SLk maps

The main advantage of the SLk index is that it can be easily estimated in an area with rivers of different length. In a simple analysis of river knickpoints, it is difficult to quantify the location of knickpoints and compare their significance between rivers. The SLk index quantifies the changes in river gradient and also identifies steeper river segments that do not have well-defined knickpoints.

In order to highlight this fact, four river profiles were extracted in order to relate their knickpoints to the SLk values. These four rivers have very well-defined SLk anomalies, but do not present comparable knickpoints (Fig. 9). The Beiro river profile, for instance, is the only one with well-defined knickpoints (Fig. 9). The different lengths of the rivers

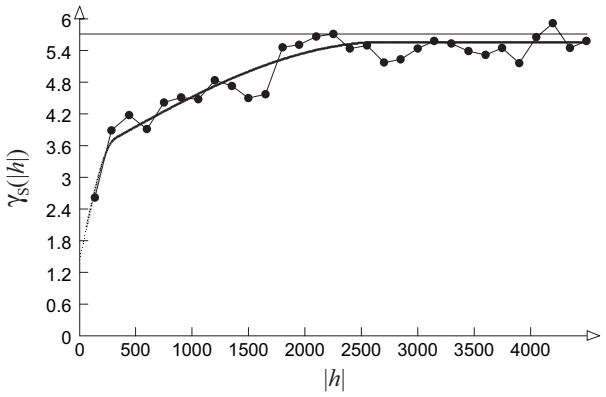

Figure 10. Omnidirectional variogram for SL data calculated with a contour interval of 50 m.

also hampers correlation between knickpoints. In the SLk map for this area, we can directly observe high-gradient values and view their distribution (anomaly 3 in Fig. 8).

The original SL index is limited in that a value comparison is impossible without prior normalization. The anomalies in long rivers will, by definition, be greater than in short rivers, even when they can be related to the same geomorphic feature. Therefore, in these maps anomalies in long rivers will mask anomalies in short rivers.

In order to compare the differences between the SL and the normalized SLk index, we have derived for the same area a SL map made with a contour line interval of 50 m (Fig. 11). Since we use contour spacing as sampling intervals in this map, the SL values are denser along the steeper channel headwaters. In contrast, at river mouths the SL values are more dispersed. Geostatistically, it is better to have an equally-spaced point-distribution in order to analyse patterns. The spatial variability structures were obtained and adjusted into a theoretical model composed of two spherical structures, one short scale (450 m) with a variability equal to 16,500 and another large scale (2,880 m) with a sill equal to 15,840 (Fig. 10). The estimation has been made using the same parameters (search distance, number of data in the estimation, grid size) as the SLk estimation process in order to compare the results. Both maps show roughly the same main anomalies along the longer rivers, but in the SL map there are almost no anomalies in shorter rivers (Fig. 11). Moreover, in the SL map, the anomalies have different shapes than in the SLk map (Fig. 8).

Due to the recent popularity of slope-area analysis, we also present our point of view on its advantages and disadvantages versus SLk analysis. Kobor et al. (2004), for example, carried out a slope-area analysis for several small sub-basins in the central Oregon Coast

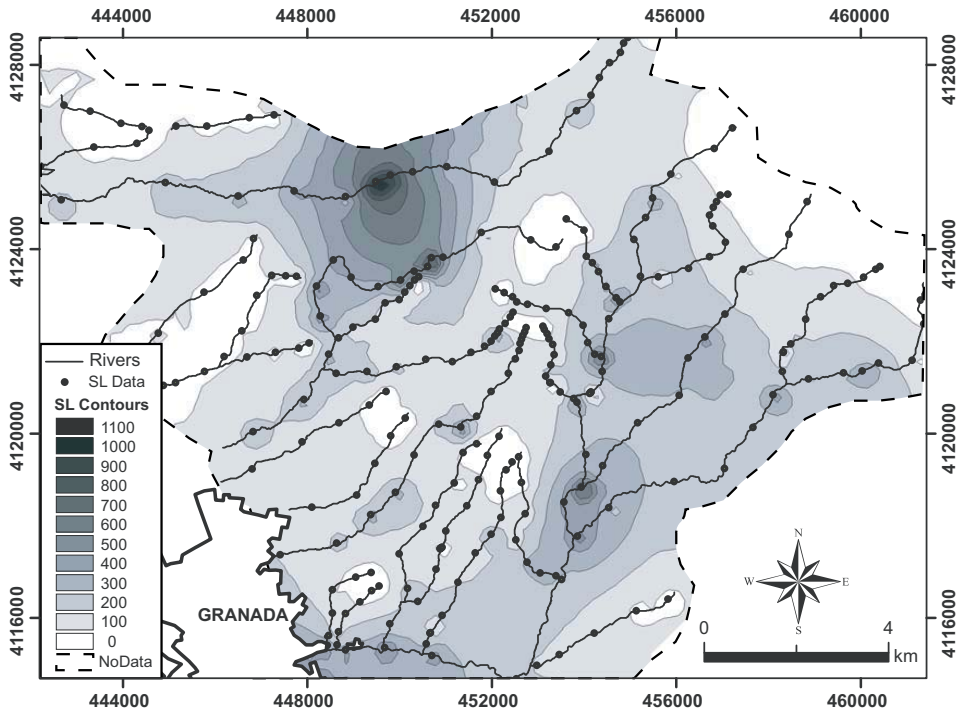

Figure 11. SL map of the NE border of Granada basin obtained according to methodology proposed by Keller and Pinter (2002). The kriging was made using the same parameters (search distance, number of data in the estimation process, grid size) as the SLk estimation process.

Range. This analysis was very useful in determining the parameters in those small sub-basins but not for inflection analysis of the main streams. Kirby et al. (2003) made a very valuable analysis of the concavity index and the steepness index (both extracted by this well established area-slope relation) in streams of the Tibetan Plateau. In their study, Kirby et al. (2003) needed to perform different regression analyses in the rivers that presented clear breaks in the slope-area line regression. So, these results suggest that slope-area analysis is not the best way to examine gradient differences within the same river but may be a very valuable tool for the analysis and comparison of individual basins. In this regard, the SLk index is not an appropriate geomorphic tool for the analysis of small basins, but is suitable for the analysis of long river profiles. Moreover, it is noteworthy that the drainage pattern plays an important role in the applicability of the SLk index. Poorly organized parallel or sub-parallel drainage patterns with long main channels provide better correlations among rivers and thus are very suitable for SLk analyses; in contrast, well-organized dendritic river networks are less suitable for the SLk analysis but are good material for slope-area analyses.

6. CONCLUSIONS

In this paper a methodology for GIS analysis of drainage networks has been presented. This analysis is particularly useful in areas that lack other tectonic, structural, or seismic data. The SL index has been normalized via the graded river gradient K. This graded river gradient characterises the equilibrium profile and correlates with the total stream power. In light of this relation, the discharge-area proxy can be calibrated. We propose the use of a normalized SL index (SLk index), to allow comparisons among rivers of different length and the production of SLk maps. The anomalous values of the SLk index were identified by means of a cross-validation method and related with faults and lithological contacts. The SLk map presented has advantages with respect to a simple profile-knickpoint analysis in the visualisation, definition, and comparison of knickpoints along different rivers. The comparison of an SLk map with a SL map shows the main pitfalls of the previous approach due to the lack of value normalization. The anomalies in the SLk map faithfully reflect the main tectonic and lithological features of the study area. A closer comparison with other studies, namely those performed with the slope-area proxy, shows that the SLk index is more reliable in poorly organized sub-parallel drainage patterns, whereas slope-area analyses are a better approach in well-organized dendritic river networks.

Acknowledgements: This study was supported by the grants BTE2003-01699 and CGL2004-03333/BTE of the Spanish Ministry of Education. We thank Dr. Oliver Korup and an anonymous reviewer for their thorough reviews of the manuscript and their positive comments. We also thank Christine Laurin for editing the English text.

3

Differentiating geology and tectonics using a spatial autocorrelation technique for the hypsometric integral

J. V. Pérez-Peña [(1)*], J. M. Azañón [(1, 2)], G. Booth-Rea [(1)], A. Azor [(1)] and J. Delgado [(3)]

(1) Departamento de Geodinámica, Universidad de Granada, Granada, Spain
(2) Instituto Andaluz de Ciencias de la Tierra (UGR-CSIC)
(3) Departamento de Ingeniería Cartográfica, Geodésica y Fotogrametría, Universidad de Jaén, Jaén, Spain
* Correspondence to: JV Pérez-Peña, Departamento de Geodinámica, Campus Fuentenueva s/n, Universidad de Granada, 18071 Granada, Spain. E-mail: vperez@ugr.es

ABSTRACT: Hypsometry is thought to be sensitive to tectonic uplift rates and lithology differences. In this study we calculated hypsometric integrals (HIs) using as topographic sources two digital elevation models of 10 and 90 m of pixel resolution in the Granada basin (SE of Spain). The HI spatial distributions do not show clear spatial patterns and do not correlate with basin parameters as mean elevation or relief amplitude. However, when exploratory spatial data analysis is applied to the data distributions through local indices of spatial autocorrelation (LISA) clear hot-spots are visible that improve the geologic meaning of the HI. The distributions are robust and independent of the model resolution but are scale influenced. The application of this new method to the Granada basin shows a strong correlation between the main distribution of active normal faults in the basin and the clusters of high or low HI values obtained in our analysis. Clusters with high HI values define the uplifted footwalls of these faults and regions uplifted in relation with rollover anticlines or where epeirogenic uplift has not been counteracted by local extension. Once the method was adjusted in the Granada basin we tested its applicability in an area of known contractive tectonic activity, Central Otago in New Zealand, showing that the meaning of HI values is improved by using the autocorrelation techniques.

Keywords: Hypsometric integral; GIS; LISA; Active tectonics; Granada basin

Journal of Geophysical Research-Solid Earth (2009)
DOI:10.1029/2008JF001092
Received 20 June 2008
Revised 21 January 2009
Accepted 10 February 2009

1. INTRODUCTION

Morphometry, defined as quantitative measurements of landscape shape, is one of the key tools of tectonic-geomorphology. The distribution of elevations within a region provides information on the balance between external processes (which tend to lower the landscape) and internal processes (which tend to create relief). One of the most useful parameters that describe and analyze the distribution of elevations in an area is hypsometry.

Hypsometry describes area distribution at different elevations (Strahler, 1952; Schumm, 1956) and can be estimated using the hypsometric curve or the hypsometric integral (HI). The hypsometric curve represents the relative proportion of area below (or above) a given height (Fig. 1a). The hypsometric integral corresponds to the area below the hypsometric curve and, therefore, is correlated with the shape of this curve (Pike and Wilson, 1971; Keller and Pinter, 2002). The hypsometric integral can be approximated by means of the following equation:

$$H = \frac{\text{mean elevation} - \text{minimum elevation}}{\text{maximum elevation} - \text{minimum elevation}} \quad (1)$$

The hypsometric curve and the hypsometric integral are valuable tools in characterizing topography because they are correlated with the stage of geomorphic development of the landscape. Strahler (1952) correlated convex hypsometric curves with a youthful stage, S-shaped curves with a mature stage, and concave curves with a peneplain stage (Fig. 1b). This evolution is based on the assumption that a mountain is rapidly uplifted without serious denudation, and then increases in dissection with a lowering in mean elevation (Davisian scheme). However, subsequent works have proposed different alternatives to this hypsometric curve evolution. Willgoose and Hancock (1998) modeled the evolution of simulated basins and found that, in the case of declining equilibrium, hypsometric curves converged to a constant S-shaped form and not to the concave form proposed by Strahler (1952) for the peneplain stage. Ohmori (1993) analyzed several large-scale natural drainage basins in Japan (up to 10,000 km^2) and made a study of simulated basins based on empirical laws deduced from Japanese mountains. The resulting hypsometric curves were concave or S-shaped but never convex. In this case, the assumption of the Davisian scheme (an initial rapid uplift without erosion) is not valid; the Japanese mountains, although young, have been strongly eroded during uplift (Ohmori, 1993).

Hypsometry is affected principally by tectonic, lithologic, and climatic factors. Masek et al. (1994) proposed a climatological effect on hypsometry by comparing two large-scale drainage basins in the central Andean plateau. Lifton and Chase (1992) pointed to the

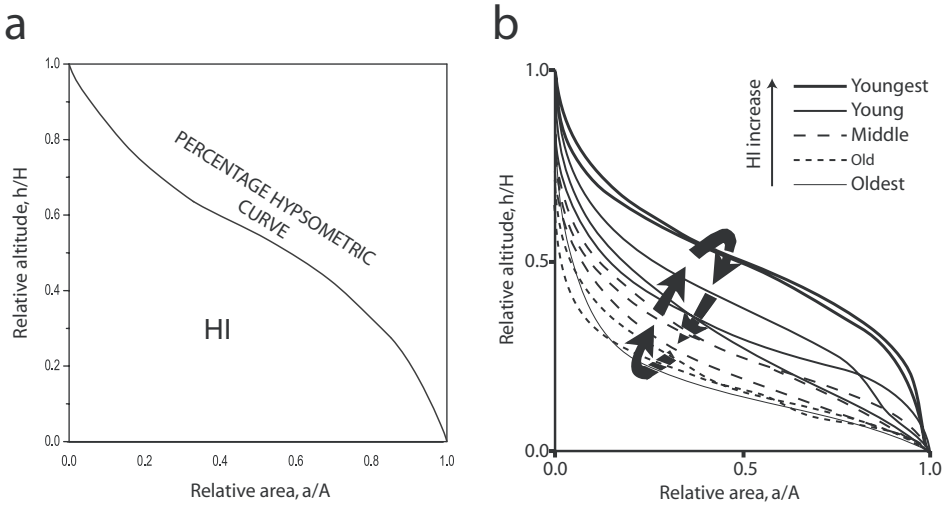

Figure 1. a) Hypsometric curve after Strahler (1952). Area of the region under the curve is known as the hypsometric integral (HI). Total elevation (H) is the relief within the basin (maximum elevation minus the minimum elevation), total area (A) is total surface area of the basin, and area (a) is surface area within the basin above a given altitude (h). **b)** Changes in hypsometric curves (Modified from Ohmori, 1993). Convex curves and high HI values are typical for youthful stages of maturity and s-shaped curves and concave curves together with low HI values are typical for mature and old stages. Arrows indicate a direction of change in the curves according to change in mountain altitude during the geomorphic cycle.

influence of lithology in the hypsometric integral at small scales (100 km^2) and an influence of tectonics at larger scales (1,000 km^2). They also showed, through a numerical model, that the hypsometric integral is positively correlated with the uplift rate. Chen et al. (2003) used values of the hypsometric integral to differentiate morphotectonic provinces in the foothills of Taiwan.

The hypsometric integral (HI) is thought to be influenced by basin parameters such as basin geometry, drainage area, and basin elevation drop (Lifton and Chase, 1992; Masek et al., 1994; Hurtrez et al., 1999; Chen et al., 2003). Nevertheless, Walcott and Summerfield (2008) demonstrated that HI values obtained for several basins and sub-basins along the southeast margin of southern Africa did not correlate with basin area or basin shape. Their HI values showed complex relationships with indices of vertical scale as relief and dissection.

In this study we obtain HI values for regular squares of an analysis grid instead of values for basins and sub-basins. This way, we obtain a regular HI value distribution that is independent of basin geometry and drainage area. Since we do not use drainage basins, HI

values do not strictly represent a measure of dissection but instead, how rapidly elevation changes within each square (van der Beek and Braun, 1998).

We examine variations in the hypsometric integral for different-sized analysis-grids obtained for a drainage basin in the south of Spain, the Genil river. This river drains the sediments of the Granada basin, one of the largest intramontane basins of the Betics. Its Quaternary evolution is marked by its capture by the external drainage of Genil-Guadalquivir river system and the segmentation of the basin by active normal faults. These faults show some of the highest slip rates in the Betics. Therefore, this Neogene to Quaternary sedimentary basin provides a good scenario to evaluate fault activity and related erosion processes. In our study, we performed the analysis using two different Digital Elevation Models (DEM) of 10 and 90 m resolution, and one DEM of 90 m resolution obtained by re-sampling the 10 m DEM. We focused on the HI value distributions and use local indicators of spatial autocorrelation (LISA) in order to differentiate clusters of high or low values and evaluate their significance. Once the method was adjusted in the Granada basin we probed its applicability elsewhere, by performing an analysis in the Central Otago region in New Zealand, an area of known contractive tectonic activity.

2. GEOLOGICAL AND GEOMORPHOLOGICAL SETTING

The Granada basin (Fig. 2) is one of largest Neogene basins of the Betics. It formed since the late Miocene in the hanging wall of a core-complex-type extensional detachment system related to the extensional collapse of the Betic-Rif orogenic belt. This extension and coeval NW-SE convergence between Africa and Iberia (de Mets et al., 1994) resulted in the development the Sierra-Nevada elongated dome, characterized by folding of the unloaded footwall (e.g. Martínez-Martínez and Soto, 2002; Martínez-Martínez et al., 2004). The basin infilling began in the late Tortonian (ca. 8.5 Ma) with marine calcarenites that intefinger distally with calcareous marly facies (Rodríguez-Fernández and Sanz de Galdeano, 2006). These sediments sealed the continental subduction contact between the metamorphic Alboran crustal domain and the South Iberian thrust belt formed by detached Mesozoic to Tertiary passive margin sediments (Platt et al., 2003). During the latest Tortonian (ca. 7.2 Ma), thick evaporitic deposits (gypsum and salts) and associated coarse clastic sediments in the basin margins indicate the transition from marine to continental conditions. Further epeirogenic uplift of the basin during the Messinian (e.g. Braga et al., 2003; Duggen et al., 2003) resulted in the deposition of thick and coarse detrital deposits that interfinger with lacustrine turbiditic sequences related to deep lakes. Lacustrine limestones deposited in central areas of the basin in the late Messinian (e.g. Rodríguez-Fernández and Sanz de Galdeano, 2006). Continental conglomerates, sands, and clays characterize the Pliocene to Pleistocene sedimentary sequences, locally interfingered with palustrine carbonate sediments.

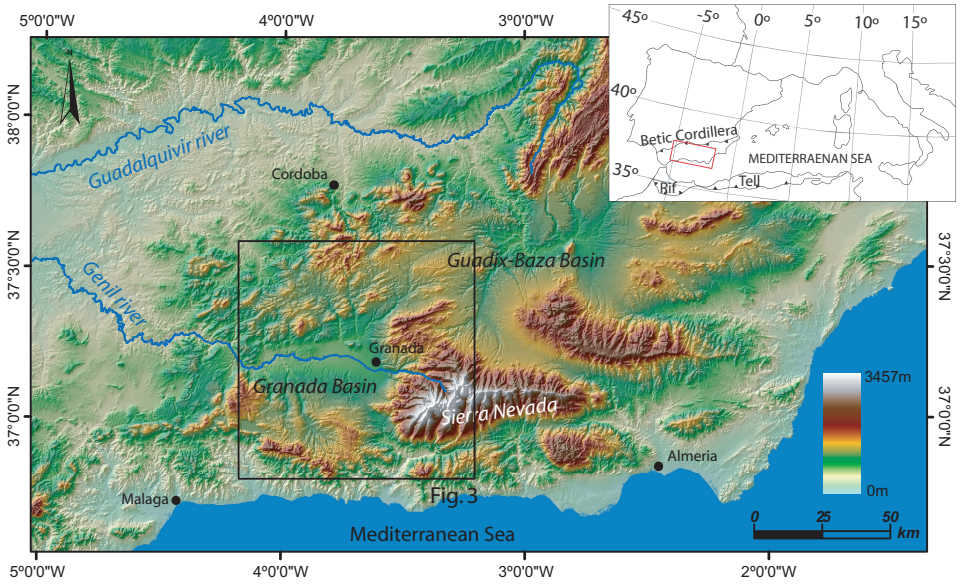

Figure 2. General location of the Granada sedimentary basin. The location of the figure 3 is indicated.

Accommodation space for the Granada basin Plio-Quaternary continental sediments was produced in a general context of epeirogenic uplift by NW-SE trending normal faults (Fig. 3) that bound the eastern and northern margins of the basin (Rodríguez-Fernández and Sanz de Galdeano, 2006). Most of these faults were active in the Pleistocene and have associated seismicity (Sanz de Galdeano et al., 2003; Azañón et al., 2004). Sanz de Galdeano et al. (2003) carried out an analysis to elucidate the seismic potential and the slip rate for some of these normal faults obtaining moderate slip rates (more than 0.25 mm/yr) for the most active faults in the basin (Fig. 3). These slip rates are long term, averaged since the Late Miocene. Nevertheless, more recent works using Quaternary dating methods point to larger slip rates for some of these faults. Reinhardt et al. (2007b) studied the transient response to a recent rapid fall in base level of a small mountain catchment that is bordered in its mouth by one of these faults in the eastern margin of the Granada basin. In order to explain the very high erosion rates recorded in this catchment they proposed a 50 m base-level fall in the last 21 ka.

The internal drainage of the Granada sedimentary basin was captured by the Guadalquivir river in the Late Pleistocene as occurred in the neighboring Guadix-Baza basin (Calvache and Viseras, 1997; Pérez-Peña et al., 2009b). Since then, the drainage network has eroded the sediments of the basin, although not with a headward erosion pattern as ob-

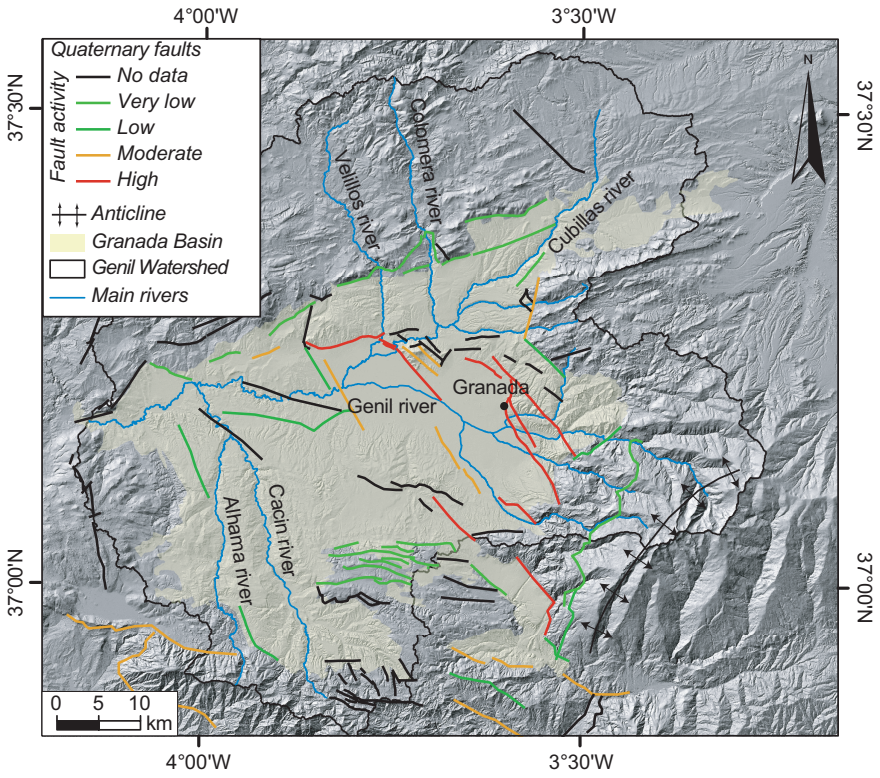

Figure 3. Digital Elevation Model (10 m pixel resolution) for the Genil watershed. The figure shows the main rivers and sediments of the Granada basin and the Quaternary structures. The relative activity of the faults has been taken from Sanz de Galdeano et al. (2003).

served in the Guadix-Baza basin (Pérez-Peña et al., 2009b). River incision in the Granada sedimentary basin is more pronounced in its northeastern border and in a wide area south of the Genil river (Fig. 3), but not near the basin capture point, where the Genil river shows practically no incision. The morphology of the basin is conditioned by the segmentation pattern of active faults that compartmentalize it, with a pronounced river incision in the normal-fault footwalls and practically no erosion in the hanging walls.

3. METHODOLOGY

We propose calculating HI values not for basin and sub-basins but for regular squares in order to obtain a regularly-spaced value distribution for the area. To obtain HI values for a grid of regular squares (analysis grid), we used zonal statistics over a Digital Elevation

Model to extract maximum, minimum, and mean elevations. With the aid of GIS software, this procedure becomes almost direct.

The distribution of HI values thus estimated can vary considerably across neighboring squares due to cell allocation or lithology differences. In dissected landscapes, since we do not work with drainage basins, high values can occur together with low values depending only on the location of the squares (Fig. 4). Where tectonics play an important role, HI values should follow a general trend—that is, high and low values will tend to group together in clusters despite having local (and even high) variations. To discern whether HI values present such patterns, we have to test the spatial autocorrelation of the data. Exploratory spatial data analysis (ESDA) techniques can identify the spatial association and autocorrelation in georeferenced data sets (Anselin, 1995; Ratcliffe and McCullagh, 1998).

Moran's I (Moran, 1950) is probably the best-known measure to test for spatial autocorrelation. Formally, Moran's I is defined as:

$$I = \left(\frac{N}{\sum_i \sum_j w_{ij}} \right) \cdot \left(\frac{\sum_i \sum_j w_j (x_i - \mu) \cdot (x_j - \mu)}{\sum_i (x_i - \mu)^2} \right) \quad (2)$$

Where N is the number of observations, is the element in the spatial weights matrix corresponding to the observation pair (i, j), x_i and x_j are observations for locations i and j (with mean). The spatial weights matrix records a specific weight for each observation pair (i, j) that is $1/d_{ij}$ (d_{ij} is the distance between the two considered points). Moran's I is similar but not equivalent to a correlation coefficient in that it compares the sum of the cross-products of values at different locations, two at a time weighted by the inverse of the distance between the locations, with the variance of the variable (Moran, 1950). The value of Moran's I for lack of spatial dependence (E(I)) is not zero, but instead a number which is negative but very close to zero. E(I) is obtained when there is no spatial autocorrelation, and its value can be calculated as the mean value after a randomization of the data. A Moran's I value greater than E(I) indicates a significant autocorrelation. Instead of using the Moran's I statistics, inference is typically based on a standardized Z-score with a p-value (Anselin, 1995):

$$Z = \frac{I - E(I)}{S_{E(I)}} \quad (3)$$

Where I is the empirical value calculated from a sample, E(I) is the theoretical mean of a random distribution and SE(I) is the theoretical standard deviation of E(I). The Z-score

is a test of statistical significance that helps us to decide whether or not to reject the null hypothesis (the data are randomly distributed and there is no autocorrelation). The p-value is the probability that the null hypothesis have falsely been rejected.

It is now recognized that while global spatial autocorrelation may provide a limited set of association results, local patterns of influence can also be used to describe the spatial independence of data (Getis and Ord, 1996). Local statistical methods can assess the spatial association of a variable within a specified distance of a single point. This class of statistics has rapidly grown in acceptance (Unwin, 1996), and is referred to by the term LISA: local indices of spatial autocorrelation (Anselin, 1995). These types of statistics differ from procedures which are applied globally, such as Moran's I, which is tested on the complete study area under examination. LISA statistics are applied locally, and are particularly useful in identifying the existence of local spatial clustering around an individual location, or 'hotspots' (Anselin, 1995; Getis and Ord, 1996).

Although all LISA statistics assess the local association amongst the data, the Getis-Ord Gi* statistic (Ord and Getis, 1995) evaluates association by measuring additive qualities, and can therefore compare local averages to global averages. This statistic provides specific measures of spatial association by defining a set of neighbors for each location as being those observations that fall within a distance (d). These measures indicate the extent to which a location is surrounded by a cluster of high or low values for the variable under consideration. Formally, the Getis-Ord Gi* statistic (Ord and Getis, 1995) is defined as:

$$G_i^* = \frac{\sum_j w_j(d) x_j}{\sum_j x_j} \tag{4}$$

Where $w_{ij(d)}$ are the elements of the contiguity matrix for distance d. This matrix assigns a spatial weight for each point pair; a binary classification dependent on whether the point is within a distance d of i. The Gi* statistic obtains in each observation point i a measure of spatial clustering that includes the observation and depends on the distance of the neighboring points. This statistic has been used to locate and identify local autocorrelations in research fields, including remote sensing (Wulder and Boots, 1998), ecology (Diniz et al., 2003), criminology (Ratcliffe and McCullagh, 1998), and sociology (Unwin, 1996; Amrhein and Reynolds, 1997). However, these techniques are normally not used in geomorphology.

4. HI ANALYSIS

4.1. Extraction of HI values

We have obtained HI values for the catchment area of the Genil river for two different DEMs of 10 and 90 m resolution, and additionally for one DEM of 90 m resolution obtained by resampling the 10 m resolution model. The 10 m resolution DEM was provided by the Junta de Andalucía regional government. This DEM was generated from 1:20,000 (B&W) Aerial Photographs (previously corrected and orientated with the aid of several Topographic Control Points) obtained in a photogrammetric flight (years 2001-2002) for the entire Andalucía region. This model is geo-referenced on to a Universal Transverse Mercator projection using European Datum 1950 (zone 30). The 90 m resolution DEM is based on Shuttle Radar Topography Mission (SRTM) 3-arc-second digital elevation data. These data were re-projected to the same system as the 10 m model for consistency. All the models were pit-filled using AcrGis 9.1 generic tools in order to fill possible voids.

Most of the present-day incised channels within the Granada basin have a hectometric scale and are rarely wider than 1 km. Therefore, we consider that a kilometric-scale analysis grid can efficiently record the topographic characteristics of the area. In order to analyze the scale influence in HI value distribution we used different-size analysis grids for both DEMs. We calculated HI values for 500 m, 1km, and 2km analysis grids with the 10 m DEM and for 1km and 2km for the 90 m DEM. For the third regridded 90 m DEM we used only an analysis grid-size of 1 km. We used ArcGis 9.1 software to perform zonal statistics for each cell of the analysis grids using the elevation data of the DEMs. The HI values in the six cases follow a normal distribution with a mean average slightly under 0.5 (Fig. 5).

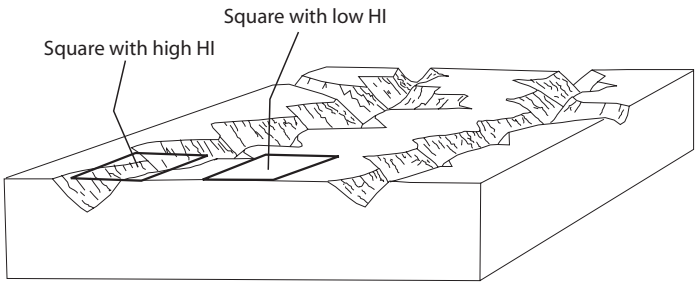

Figure 4. Schematic illustration showing how HI values estimated for regular squares can present high variation depending only on the square location (modified from Keller and Pinter, 2002).

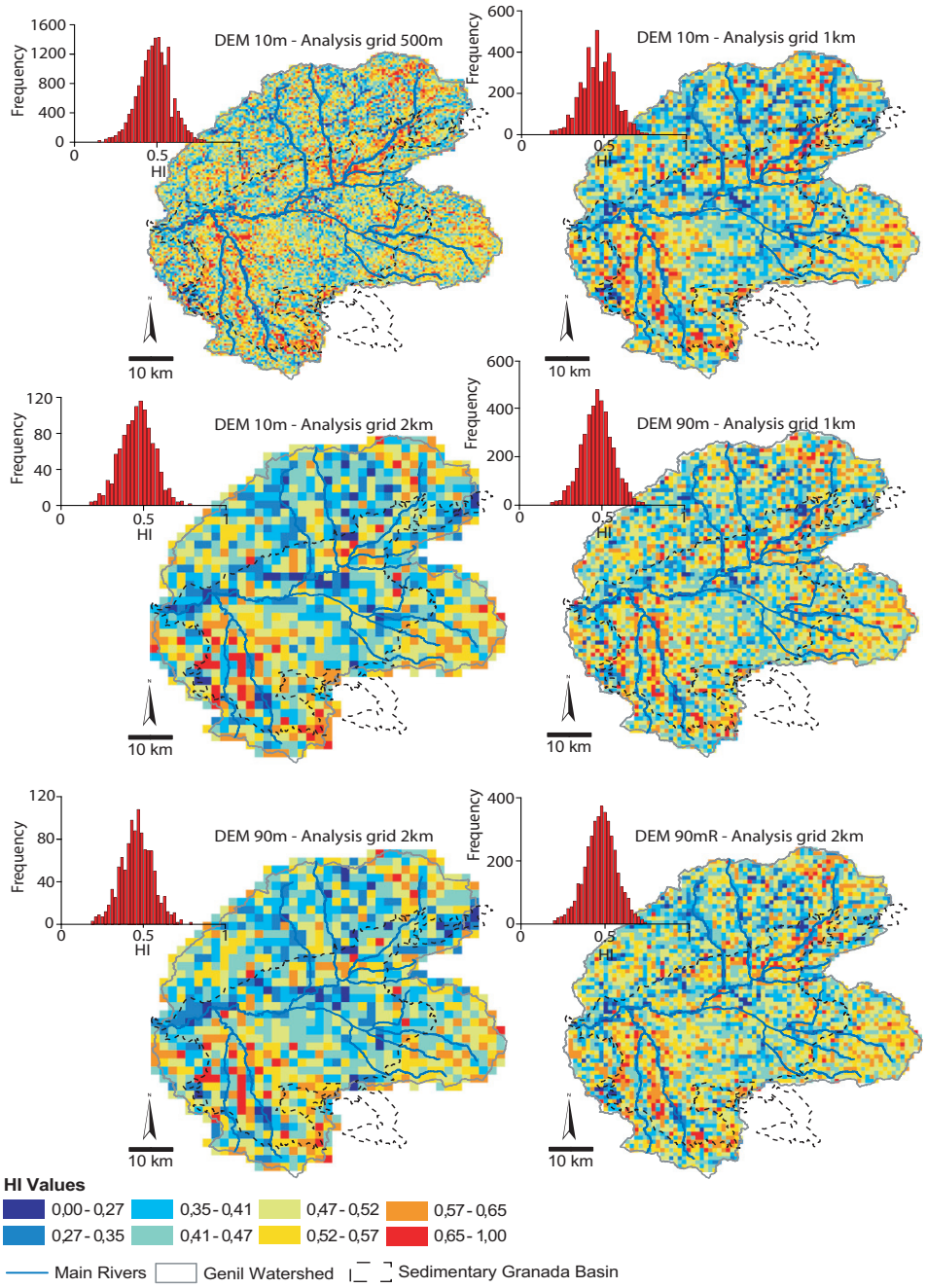

Figure 5. HI distributions using two different elevation models of 10 and 90 m and for different analysis grids sizes. There are no clear spatial patterns in the raw data, but the distributions with different DEMs using the same analysis grid size are similar.

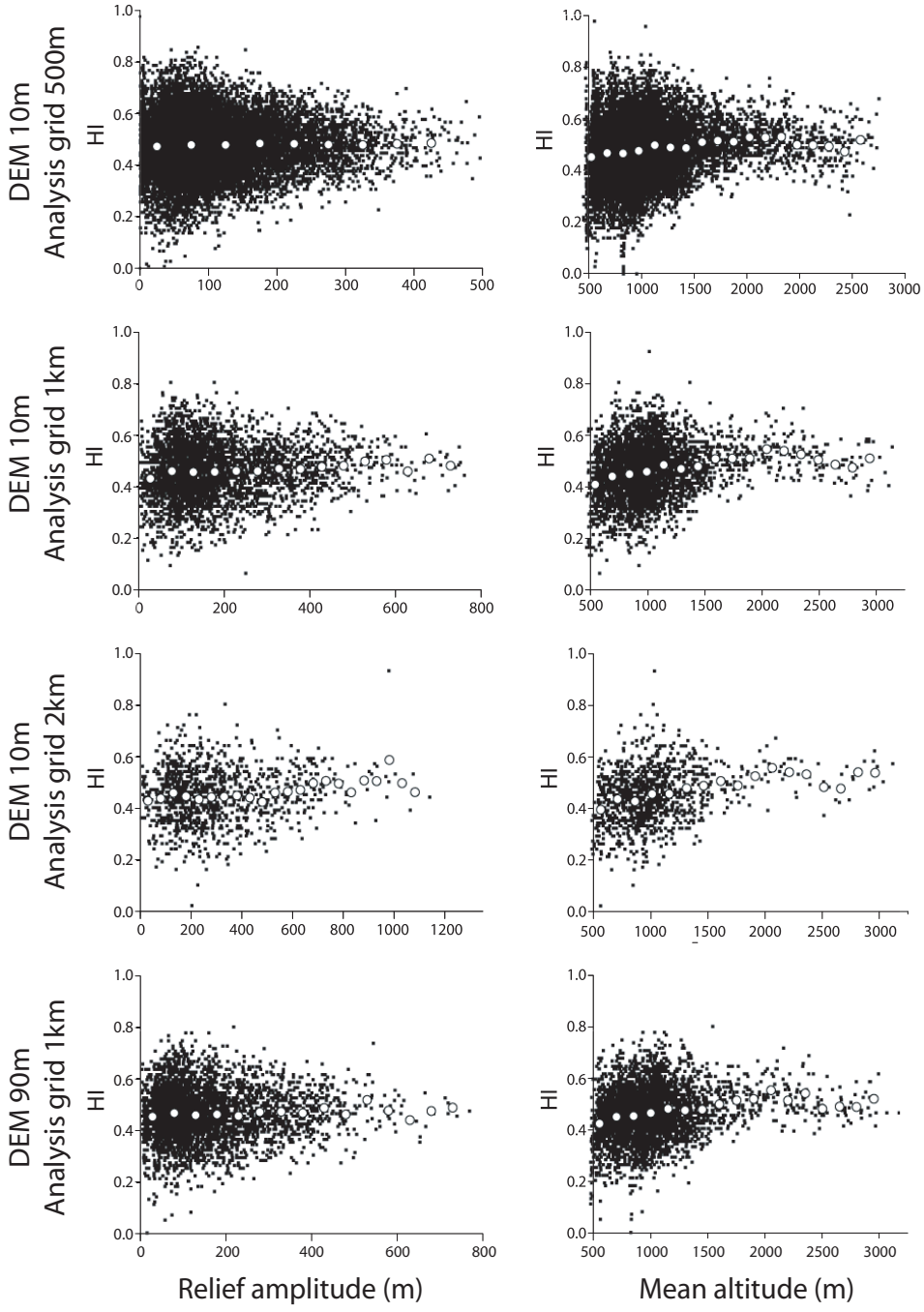

Figure 6. HI values versus relief amplitude and versus mean altitudes for the five considered cases. There are no clear relations between HI and these two parameters.

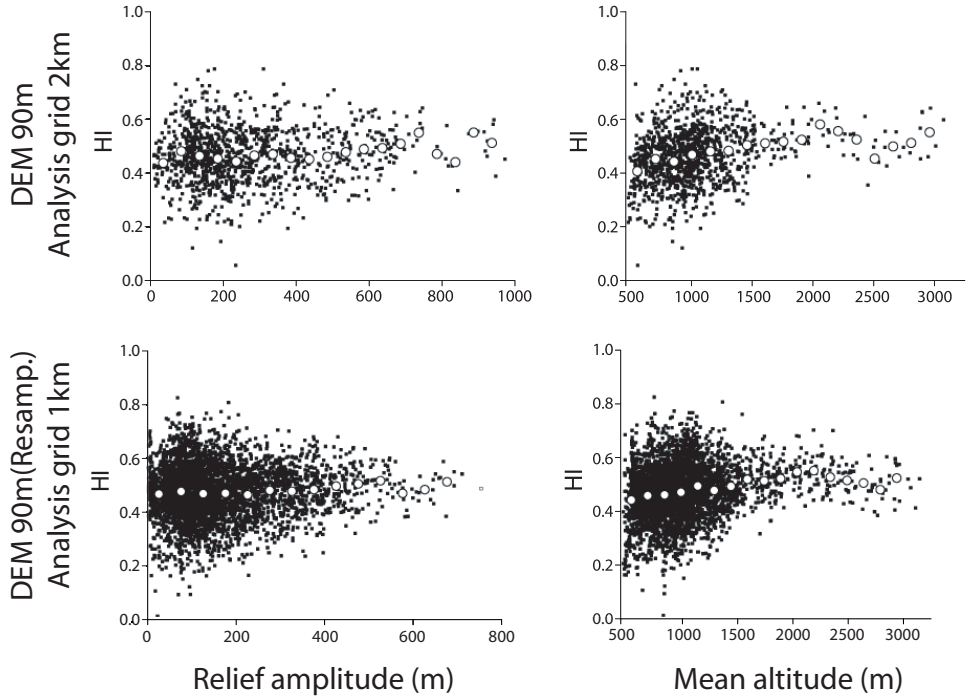

Figure 6. (Continuation).

The spatial distribution in each case does not offer a clear view of grouped values because of patial dependency of HI values

The HI values could be spatially dependent due to the relative topographic position of the squares within the basin (Chen et al., 2003). In order to test whether the HI values have such a dependency, we calculated two representative factors—the mean elevation and the relief amplitude (maximum elevation – minimum elevation) for each square. The squares located in the head of a catchment will be characterized by high mean elevation together with high relief amplitude (since in the upper parts the low order streams have steeper gradients, see Figure 8 in Chen et al., 2003).

Figure 6 shows HI versus mean elevation and HI versus relief amplitude for the five considered cases. In all the plots, the HI values are distributed around the HI mean, but there is significant scattering indicating that both factors are highly variable. Both graphics seem to be biased by the high number of low–medium values. However, when HI values are binned in fixed-intervals on the horizontal axis and averaged, a better correlation is visi-

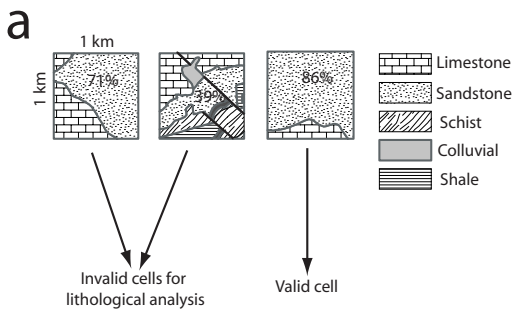

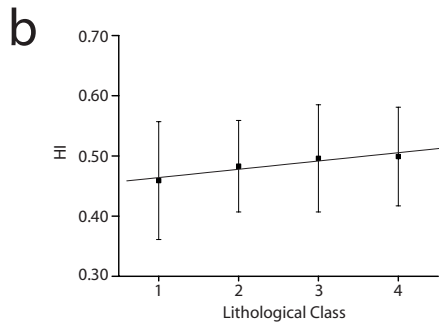

Rock Type	Class
Soft sedimentary Rocks (muds, clays, marls and loose sediments)	1
Mixed sedimentary rocks (Limestone-sandy, limestone-shaly, marlstones and limy-dolostones)	2
Hard sedimentary Rocks (Conglomerates, sandstones, limestones, and dolostones)	3
Metamorphic Rocks (Marbles, schists, gneisses, and quarzites)	4

Figure 7. a) Scheme showing the selection of valid cells for the lithological analysis. In the three cells the main lithology is sandstone, but it is only representative enough for cells where this majority represents more than 80% of the rock type. **b)** Mean HI values, obtained from the 10m DEM and the analysis grid of 1 km, for each lithologic group (lithology descriptions are found in the table below). The error bars represent the standard deviations for the HI mean values for each lithologic group.

ble. In the plots of HI versus relief amplitude we see averaged HI values in relief-amplitude intervals of 50 m. The averaged values follow almost a straight line indicating that HI values are not dependent of this factor. These findings correlate with the results obtained by Walcott and Summerfield (2008) for several basin and sub-basins of southern Africa. In the plots of HI versus mean altitude we have averaged HI values in mean altitude intervals of 150 m because the horizontal scale is nearly three times larger. The averaged values present in these plots show a more complex pattern for the larger grid sizes (1 and 2 km). Nevertheless, there are no clear correlations between the two parameters as the averaged values distribute around the mean HI values. Therefore, we can conclude that there is no clear dependency between the HI values and the position of the squares within the Genil watershed.

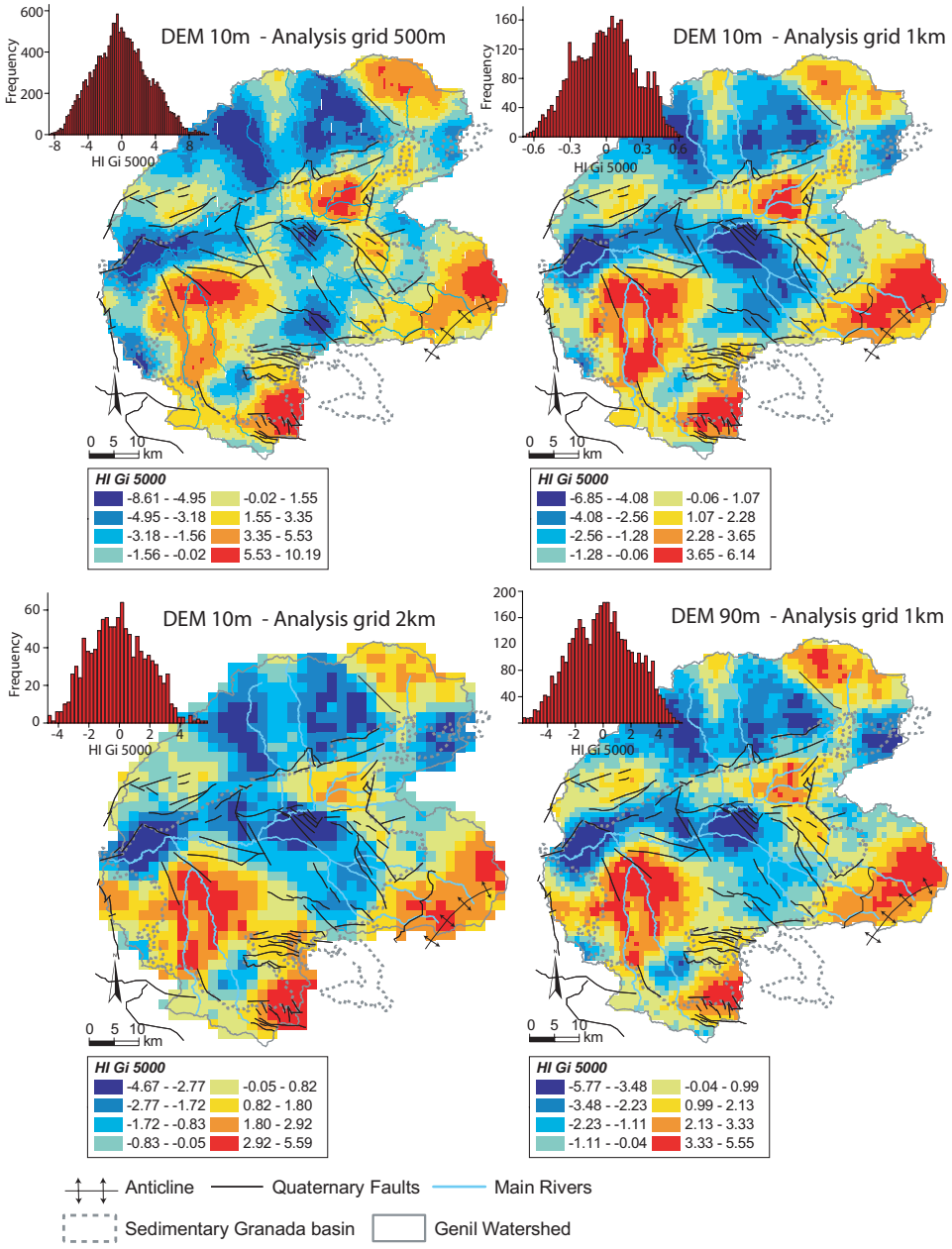

Figure 8. Getis-Ord*-statistic estimation for the HI values in the five cases. Clear clusters of high and low values are visible in all the cases but better defined when the considered analysis grid is smaller. The figure shows how the clusters of high values are related with the footwall of active normal faults. The main hot-spots are labeled in the first HI distribution. .

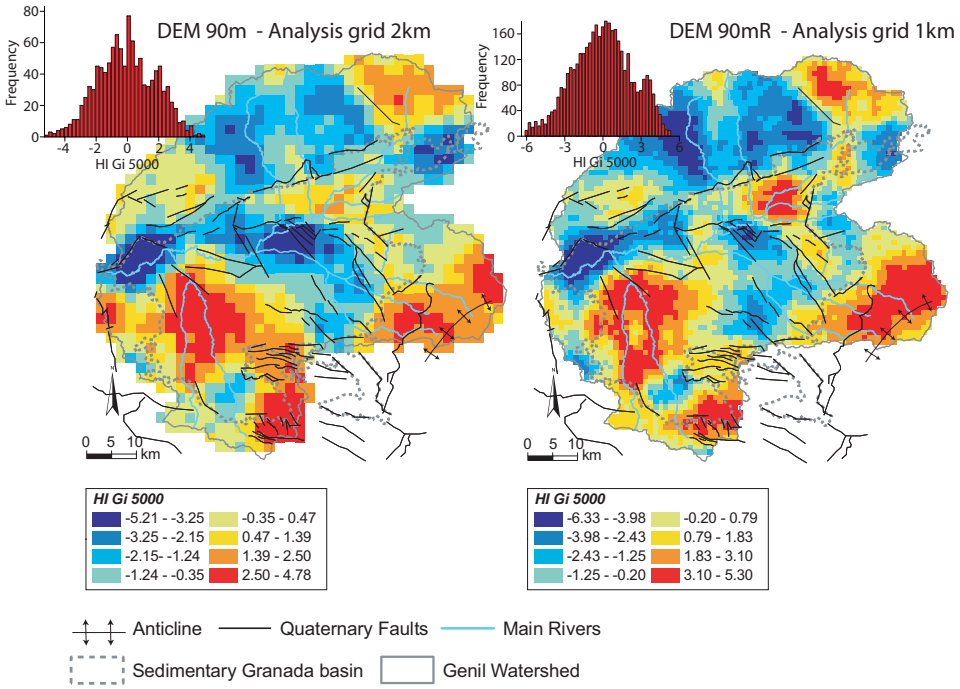

Figure 8. (Continuation)

DEM	Analysis Grid	N	I	E(I)	Z	p
10m	0.5km	16514	0.005951	-0.000061	62.965218	0.0001
10m	1km	4051	0.020737	-0.000249	41.196878	0.0001
10m	2km	1114	0.027486	-0.000898	20.704706	0.0001
90m	1km	4051	0.010346	-0.000249	27.519481	0.0001
90m	2km	1114	0.023184	-0.000898	17.566103	0.0001
90m R	1km	4051	0.018331	-0.000247	36.874131	0.0001

Table 1. Results of the global autocorrelation tests using Moran statistic for the considered cases. N, number of HI values; I, Moran index for the data set, E(I), expected Moran for a random distribution, Z, significance of Moran index, p, probability that the data distribution could be generated randomly.

4.2. Lithological influence on HI value distribution

Due to the large size of the area (nearly 4,000 km^2) and the great variability in lithology, we did not perform a detailed analysis of the erodibility, but performed a relative rock classification instead. We correlate the lithology with the HI values obtained for the 1 km analysis grid using the 10 m DEM. This lithologic analysis was carried out on the basis of 1:50,000 geologic maps, reclassifying and simplifying the different lithologies in five lithological classes in accordance with the rock type.

We computed the main lithology for each 1 km square of the Genil watershed grid—that is, the lithology that appears most often—and calculated its percentage with respect to the square. In order to avoid squares with mixed lithologies, we took into account only those squares in which the main lithology represents more than 80% of the square (Fig. 7a). Only 1,787 squares out of the 4,050 in the grid fulfill this condition. For each lithology group, the mean and the standard deviation of the HI values was obtained. Figure 7b shows the distribution of HI values in each of these lithology classes. Although slight, the mean values present a positive correlation between high HI values and hard-rock type. This fact agrees with the work of Hurtrez and Lucazeau (1999), however, the error bars (standard deviations for each HI mean value) are too high to consider a clear positive correlation within the data. Moreover, this influence is not enough to explain great variations in relative high or low HI values.

4.3. Autocorrelation analysis for the HI values

We have computed Moran's I statistic (Moran, 1950) in order to detect autocorrelation patterns in the data distributions. For each data distribution we calculated the Moran's I statistic, the expected Moran's I (under the assumption of no autocorrelation) and the Z-significance (Anselin, 1995). The results can be viewed in table 1. All the distributions show high positive Z-score values that indicate that the data are distributed in clusters. It is noteworthy that the regridded 90 m DEM shows a Z-significance which is higher than the SRTM 90 m DEM but lower than the 10 m DEM.

In order to map these clusters of high and low HI values, we have performed a hot-spot analysis by applying the Gi* statistic (Ord and Getis, 1995). We used a significance distance of 5 km to define the neighbors in the analyses. This distance has been chosen for all the distributions since the average fault length in the area is 10 km. Therefore this distance is thought to correlate neighboring cells that are affected by uplift or subsidence respectively in footwall and hanging wall fault blocks. The resulting maps (Fig. 8) show clear clusters of high and low HI values.

5. DISCUSSION

5.1. Scale and DEM dependency on LISA-HI technique

The global autocorrelation tests made through the Moran I statistic show that the data are auto-correlated presenting high positive Z-scores. The Z-score decrease in the analyses when a coarser grid is used for the same DEM, thus indicating that the correlation patterns of the data vary with the scale. The Z-scores also decrease when the 90 m DEMs

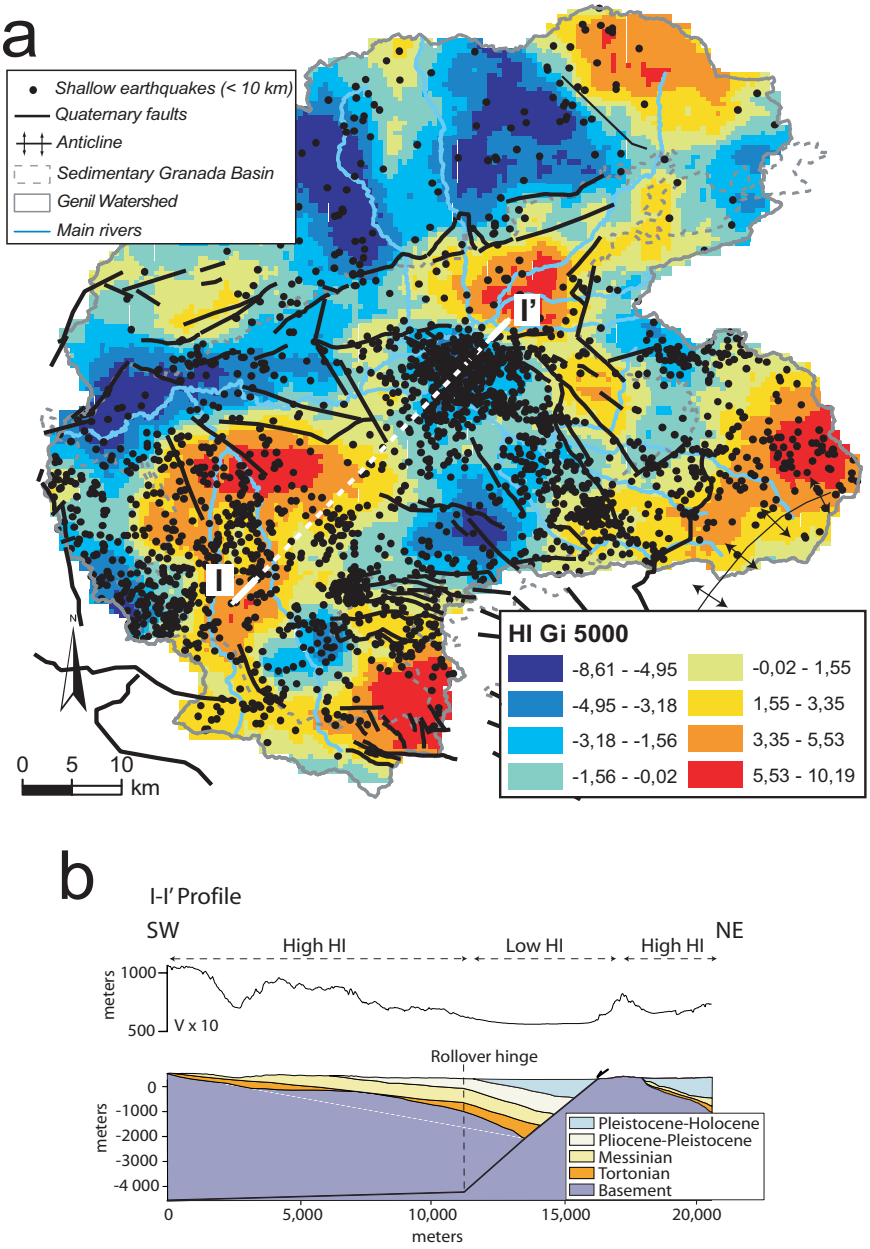

Figure 9. a) Distribution of shallow earthquakes (< 10 km) for the Genil catchment. The earthquake-epicenter distribution is very diffuse but a clear concentration can be viewed in the hanging-walls of the faults that limit hot-spot 1 in Figure8. **b)** SW-NE profile showing a schematic geology interpretation and the relation between HI values and the topography (vertical scale in the topography profile is exaggerated 10 times).

(SRTM and regridded) instead of the 10 m DEM are used. Nevertheless these variations are smaller (Table 1). The hot-spot analyses made with different DEMs on the same analysis grid are quite similar, but there is a loss in resolution for the hot-spots when the analysis grid increases, being more evident between the 1 and 2 km analysis grids (Fig. 8). Therefore we can conclude that global autocorrelation as well as LISA analyses of HI values are sensitive to scale but more robust with increasing DEM resolution. This scale-dependency agrees with the findings of Walcott and Summerfield (2008). Additionally, the similarities between the SRTM 90 m DEM and the regridded 90 m DEM, once the LISA technique was applied are noteworthy (Fig. 8). Since the regridded DEM was obtained from the more accurate 10 m dataset and yielded the same results, we can conclude that the SRTM model provide a reliable dataset for mapping and for topographic analysis. Despite the loss in resolution of the hot-spot analysis made for the analysis grids of 2 km, they present roughly the same hot-spot locations. A possible dependency on the location of the grid-cells can also be discarded: the cells of the different analysis grids cover different areas but they define the same hot-spots when the Gi* statistic is applied.

5.2. Relation between high-low HI clusters and tectonics in the Granada basin

High HI values are present in the NE, S, and SW corners of the Granada sedimentary basin (zones 1, 2 and 3 in Fig. 8, respectively), and in the northern flank of Sierra Nevada (outside of the Granada sedimentary basin limits, 4 in Fig. 8). There are also high values in the NE corner of the Genil watershed but outside of the Granada sedimentary basin limits (5 in Fig. 8). Nevertheless, there are no high values at the mouth of the Genil river, where the capture by the Guadalquivir river took place.

In the NE corner of the Granada sedimentary basin, the distribution of HI values coincides with the distribution of the main active faults in this area (1 in Fig. 8). High HI values are concentrated in the footwall of the main active NW-SE normal faults (Fig. 3), where tectonic uplift is most active. These normal faults have been active in the upper Pleistocene (Pérez-Peña et al., 2009c) and are associated with large historical earthquakes (Sanz de Galdeano et al., 2003; Azañón et al. 2004). Low-HI values occur in regions of Holocene sedimentation in the hanging wall of the main active faults. The low-HI values also coincide with the region where the shallowest earthquakes occur (Fig. 9), in the hanging wall of the main normal faults dipping SW.

The high HI values in the SW corner of the Granada basin (2 in Fig. 8) occur in the hanging wall of the main normal faults. Several processes can explain these high HI values

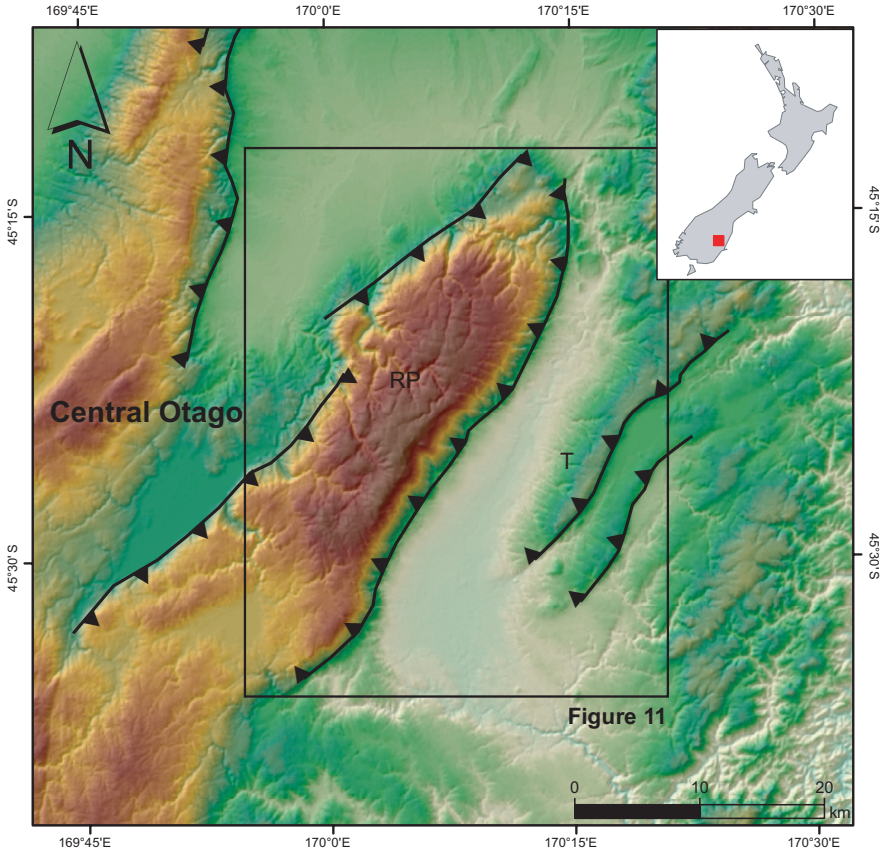

Figure 10. Location map of the Otago area in the New Zealand. The faults are taken from Jackson et al., (2002). RP, Rock and Pillar Range; T, Taieri Ridge.

away from the main fault scarps. First, the general context of epeirogenic uplift produces high HI values in areas where uplift is not counteracted by local extension; second, some additional uplift could result from the formation of a rollover fold related to the listric geometry of the normal faults that tilts the Quaternary sediments towards the NE (Fig. 9). Part of the uplift observed in the hanging wall of the faults, away from their traces, could be related with a second family of faults found south of the rollover fold hinge that marks the ramp-flat transition in the hanging wall of the fault (Fig. 9). This transition is also visible in the relief, producing higher erosion southwestwards of the rollover hinge (Figs. 8 and 9). The same reasoning can be applied to the southernmost high HI values (3 in Fig. 8). These

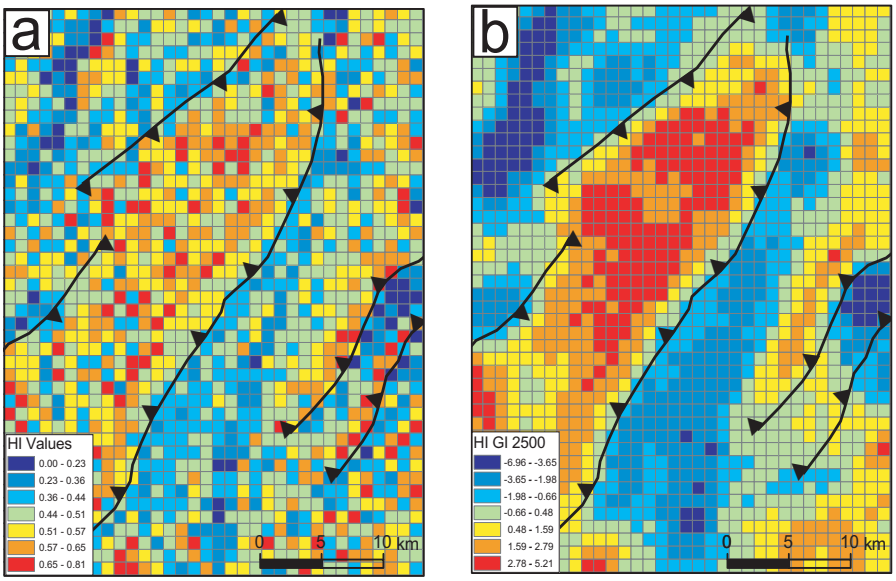

Figure 11. a) HI distributions using the SRTM 90 m DEM and an analysis grid-size of 1 km. **b)** Getis-Ord*-statistic estimation for the HI values. Clear clusters of high and low values are visible in the Rock and Pillar Range and in the Taieri Ridge. See text for further explanations.

values are disconnected from the hot-spot mentioned previously due to the influence of normal faults located southwards.

The high values in the west of the Genil watershed (4 in Fig. 8) coincide with the rolling-hinge fold of the Sierra Nevada extensional dome (Martínez-Martínez and Soto, 2002; Martínez-Martínez et al., 2004). This fold is limited in its western border by normal faults that have been active in Quaternary times yielding high slip rates (Reinhardt et al., 2008a,b).

Finally the high values in the NE corner of the Genil watershed (5 in Fig. 8), falling outside of the sedimentary Granada basin limits, coincide with the footwall of a normal fault that separates Jurassic marls and limestones from Plio-Quaternary sediments.

5.3. Applicability of the LISA-HI technique to other areas

Once the methodology proposed in this paper was adjusted for the Granada basin, we applied it to a different area of known tectonic activity in order to demonstrate its appli-

cability with other datasets and in other tectonic settings. We selected a small area located within the central Otago region in New Zealand (Fig. 10), where active folding and thrusting occurs (Jackson et al., 1996; 2002).

The region of Central Otago (Fig. 10) is located east of the Southern Alps in the South Island of New Zealand. This region presents a relatively gentle topography (500-1000 m) that consists in a peneplain, which is warped or broken into a series of parallel ridges and valleys by active folds and reverse faults trending NE-SW (Jackson et al., 1996). For the analysis, we selected a square area containing the Rock and Pillar Range and the Taieri Ridge (Fig. 10). The topographic data was obtained from the SRTM dataset, and the HI values calculated for a 1km analysis grid (Fig. 11a). We applied the Gi* statistic using 2500 m as the significance distance to define the neighbors in the analyses. This distance was selected since the amplitude of the Taieri Ridge is not larger than 5 km. The HI value distribution, although variable, shows high values in the areas uplifted by the folds and reverse faults (Fig. 11a). However, the significance of these areas is highly improved when the Gi* statistic is applied to the HI value distribution (Fig. 11b).

6. CONCLUSIONS

In the analysis performed in this work over the relief of the Genil watershed, the raw estimation of HI values does not present a clear view of grouped high or low values. However, the application of Moran's I statistic for the data shows that these data are in fact distributed in clusters. By performing a hot-spot analysis using the Gi* statistic with different DEMs and with different analysis-grid sizes, we can visualize clusters of high or low HI values. The analyses made show that HI values are robust independent of the model resolution but are affected by scale. They do not correlate clearly with lithology or relative topographic position within the Genil watershed. In the Granada sedimentary basin, the clusters of high HI values are clearly correlated with different structural domains related with the main active faults in the area. These high HI values occur in the footwall of active normal faults and in the core of rollover folds that affect the hanging wall of the faults. Low HI values occur in active and recent sedimentation areas in the footwall of the main faults, near the trace of the faults, and coincide with the main seismicity clusters in the region. When we applied the method to other region of known tectonic activity (Central Otago, in New Zealand), the clusters of high values clearly drew the uplifted areas affected by folds. The use of local indices of spatial autocorrelation (LISA) permits the extraction of clusters of high or low HI values that reflect tectonic processes occurring in a region from otherwise highly variable, uninterpretable HI values.

Acknowledgements: This study was supported by the grants CGL2004-03333/BTE and TOPO-IBERIA CONSOLIDER-INGENIO CSD2006-00041 of the Spanish Ministry of Education. We thank to Dr. Hancock, Dr. Willgoose, Dr. Brocklehurst, and to an anonimous reviewer for their concise revisions that greatly improved the contents and the quality of this paper. We are indebted to Christine Laurin for revising the English.

4

CalHypso: An ArcGIS extension to calculate hypsometric curves and their statistical moments. Application to drainage basin analysis in SE Spain.

J. V. Pérez-Peña [(1)*], J. M. Azañón [(1,2)] and A. Azor [(1)]

(1) Departamento de Geodinámica, Universidad de Granada, Granada, Spain
(2) Instituto Andaluz de Ciencias de la Tierra (UGR-CSIC)
* Correspondence to: JV Pérez-Peña, Departamento de Geodinámica, Campus Fuentenueva s/n, Universidad de Granada, 18071 Granada, Spain. E-mail: vperez@ugr.es

ABSTRACT: We present the GIS extension CalHypso to automatically extract multiple hypsometric curves from digital elevation models (DEM). This extension is programmed in Visual Basic 6 and uses the ArcObjects architecture of ArcGIS. It employs a new and easy methodology to extract the hypsometric curve by using the integer data-model properties of ArcGIS and summations algorithms. This provides an optimal integration within the program environment, allowing the representation and comparison of curves directly within the GIS main program. The CalHypso extension can also calculate the main statistics related to the hypsometric curve by applying polynomial fits. We have tested this tool in several basins of the eastern border of the Sierra Nevada dome in the Betic Cordillera (SE Spain), showing important differences in the north- and south-slope hypsometric curves. These variations are probably related to the tectonically-controlled drainage evolution of the southern border of Sierra Nevada. An eastward decrease in tectonic-driven erosion is also suggested by the hypsometric curves analysed.

Keywords: Hypsometric curve; GIS extension; Active tectonics; Sierra Nevada; Betic Cordillera

Computers & Geosicences (2009)
DOI: 10.1016/j.cageo.2008.06.006
Received 25 February 2008
Revised 30 April 2008
Accepted 4 June 2008

1. INTRODUCTION

The hypsometric curve for a drainage basin represents the relative proportion of the watershed area below (or above) a given height (Strahler, 1952; Schumm, 1956) (Fig. 1a). This surface-elevation curve is a useful tool for characterising the topographic relief within a drainage basin and, hence, establishing comparisons between different basins. The shape of the hypsometric curve is related with the stage of geomorphic development of the basin. Convex hypsometric curves are typical of a youthful stage; s-shaped curves are related to a maturity stage, and concave curves are indicative of a peneplain stage (Fig. 1b) (Strahler, 1952). The hypsometric integral is defined as the area below the hypsometric curve (Strahler, 1952; Schumm, 1956), and it has been used, as well as the hypsometric curve, to infer the stage of development of a basin. For instance, values near 1 indicate a state of youth and are typical of convex curves. Nevertheless, mature s-shaped hypsometric curves can present a great variety of shapes, but the same hypsometric integral value (Ohmori, 1993; Hurtrez et al., 1999).

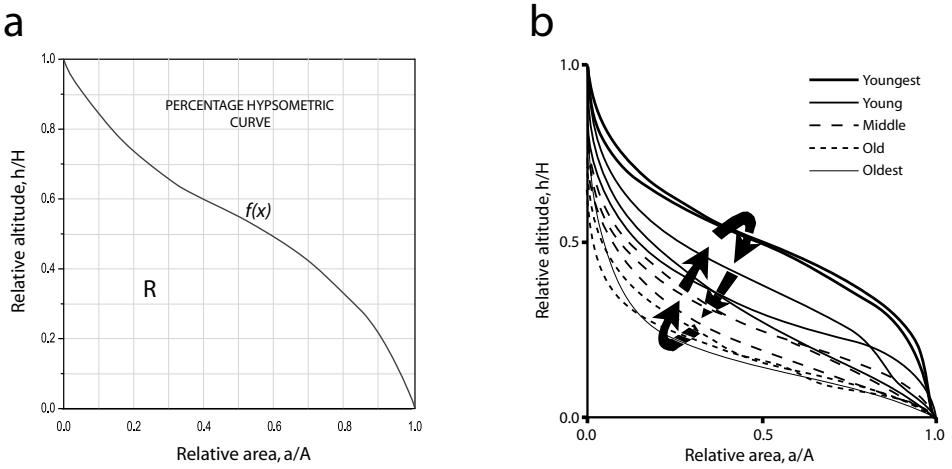

Figure 1. a) Hypsometric curve after Strahler (1952). Area of the region under the curve (R) is known as the hypsometric integral. Hypsometric curve can be represented by the function f(x). Total elevation (H) is the relief within the basin (the maximum elevation minus the minimum elevation), total area (A) is total surface area of the basin, and area (a) is surface area within the basin above a given altitude (h). **b)** Changes in hypsometric curves (Modified from Ohmori, 1993). Convex curves are typical for youthful stages of maturity and s-shaped curves and concave curves for mature and old stages. Arrows indicate a direction of change in the curves according to change in mountain altitude during a geomorphic cycle..

Hypsometric analysis has been widely used in geomorphology, hydrology, and active tectonics (Lifton and Chase, 1992; Ciccacci et al., 1992; Ohmori, 1993; Willgoose, 1994; Willgoose and Hancock, 1998; D'Alessandro et al., 1999; Chen et al., 2003). Howard (1990) studied the relations between hypsometry and hydrology, and found that hypsometric curve parameters have a pronounced relation with basin hydrology and particularly with its flood response. Masek et al. (1994) proposed a climatic effect in the hypsometry by comparing two large drainage basins in the central Andean plateau. The differences in these hypsometric curves reflected changes in erosion rates driven by climatic factors. Lifton and Chase (1992) studied the relations between tectonics and hypsometry in the San Gabriel Mountains, California. They found a positive correlation between uplift rate and the hypsometric integral. In this study they also proved a lithological influence in the hypsometry at small scales (up to 100 km^2). More recently, Chen et al. (2003) used hypsometric integral values to differentiate between different morphotectonic provinces in the foothills of Taiwan. Higher hypsometric integral values were related with hanging walls of active thrusts with considerable vertical slip. These authors also tested the spatial influence in the hypsometry by comparing hypsometric integral values in different basin types.

With the current development of Geographical Information Systems (GIS), the calculation of hypsometric curves has become easier. The spreading of digital elevation models (DEMs) offers good raw material to analyse hypsometry. It is not necessary to count on a very detailed DEM, since the hypsometric curve is robust against variations in DEM resolution (Hurtrez et al., 1999; Keller and Pinter, 2002).

Luo (1998) proposed two methods to automatically extract hypsometric curves from digital contour maps and from DEM using the GIS architecture. In DEM, this author proposed the use of zonal statistical functions integrated in GIS to obtain binned elevation frequencies from digital elevation models.

In this paper we present a method to extract relative areas and relative elevations based on the raster data model from ArcGIS. We have developed an ArcGIS extension (for ArcMap) termed CalHypso that allows the extraction of multiple hypsometric curves at once, as well as the estimation of the statistical moments for each curve. To test this program, we have carried out a hypsometric analysis in the westernmost part of the Sierra Nevada dome (Betic Cordillera, South of Spain). We have obtained the hypsometric curves and the main hypsometric statistics (Harlin, 1978; Luo, 2000) for the principal catchments in the north and south slope of the Sierra Nevada. The analysis suggests that the drainage evolution in this area is sensitive to the recent tectonics, thus reinforcing some ideas on the Neogene-Quaternary evolution of the Sierra Nevada dome.

2. STATISTICAL MOMENTS OF THE HYPSOMETRIC CURVE

Harlin (1978) developed a technique that treated the hypsometric curve as a cumulative probability distribution and used its statistic moments to describe it quantitatively. This hypsometric technique has been used to quantify hypsometric curve shapes with good results (Harlin, 1978; Luo, 2000, 2002). It consists on represent the hypsometric curve by a continuous polynomial function, (Harlin, 1978) (Fig. 1a):

$$f(x) = a_0 + a_1 x + a_2 x^2 + \ldots + a_n x^n \tag{1}$$

In this function f(x) values represent the relative-altitudes (h/H) and x values represent the relative-areas (a/A) (Fig. 1a). The relatively simple shape of the hypsometric curve, generally with few inflexions, can be fitted to a low-order polynomial function of 2nd or 3rd grade (Harlin, 1978). If we assume the hypsometric curve to be a polynomial function of 3rd grade of the form;

$$f(x) = a_0 + a_1 x + a_2 x^2 + a_3 x^3 \tag{2}$$

The function can be characterised by the coefficients a_0, a_1, a_2 and a_3, which can be obtained by regression of the hypsometric curve.

The hypsometric curve takes the values of f(x) within a unit square defined by the area and altitude axes (Fig. 1a). The hypsometric integral is defined as the area below the hypsometric curve (R in figure 1a) and, therefore, it can be calculated by exact integration of f(x) between the limits of the unit square. The result of this integration can be solved as a summation expression (Harlin, 1978):

$$A = \int_0^1 a_0 + a_1 x + a_2 x^2 + a_3 x^3 f(x)dx = \left[a_0 x + \frac{a_1 x^2}{2} + \frac{a_2 x^3}{3} + \frac{a_3 x^4}{4} \right]_0^1 = \sum_{k=0}^{3} \frac{a_k}{k+1} \tag{3}$$

We can define the first moment of f(x) about the x-axe for the unit square as a summation expression too, which represents the x-mean or centroid:

$$\mu_{01}^{'} = \frac{1}{A} \int_0^1 x f(x)dx = \frac{1}{A} \left[\frac{a_0 x^2}{2} + \frac{a_1 x^3}{3} + \frac{a_2 x^4}{4} + \frac{a_3 x^4}{4} \right]^1 = \frac{1}{A} \sum_{k=0}^{3} \frac{a_k}{k+2} \tag{4}$$

In the same way, the moments of f(x) about the x-mean can be defined as:

$$\mu_i = \frac{1}{A} \int_0^1 \left(x - \mu_{01}^{'} \right)^i f(x)dx \tag{5}$$

The second moment (μ_2) of f(x) about the x-mean is known as the variance, and can be expressed as a summation expression by following a similar development as in equations (3) and (4). The standard deviation (σ) is the square root of the variance:

$$\mu_2 = \frac{1}{A}\int_0^1 \left(x - \mu_{01}^{'}\right)^2 f(x)dx = \left[\frac{1}{A}\cdot\sum_{k=0}^{3}\frac{a_k}{k+3}\right] - \left(\mu_{01}^{'}\right)^2 \tag{6}$$

$$\sigma = \sqrt{\mu_2} \tag{7}$$

The third (μ_3) and four (μ_4) moments about the x-mean are known as the skew and kurtosis of the distribution function respectively, and they can be derived as follows (Harlin, 1978):

$$\mu_3 = \frac{1}{A}\int_0^1 \left(x - \mu_{01}^{'}\right)^3 f(x)dx = \left[\frac{1}{A}\cdot\sum_{k=0}^{3}\frac{a_k}{k+4}\right] - \left[\frac{3\mu_{01}^{'}}{A}\cdot\sum_{k=0}^{3}\frac{a_k}{k+3}\right] + 2\left(\mu_{01}^{'}\right)^2 \tag{8}$$

$$\mu_4 = \frac{1}{A}\int_0^1 \left(x - \mu_{01}^{'}\right)^4 f(x)dx = \left[\frac{1}{A}\cdot\sum_{k=0}^{3}\frac{a_k}{k+5}\right] - \left[\frac{4\mu_{01}^{'}}{A}\cdot\sum_{k=0}^{3}\frac{a_k}{k+4}\right] + \left[\frac{6}{A}\left(\mu_{01}^{'}\right)^2\cdot\sum_{k=0}^{3}\frac{a_k}{k+4}\right] - 3\left(\mu_{01}^{'}\right)^4 \tag{9}$$

The skew and the kurtosis have the same units as the x-variable and they can presents problems with unit and scale. Therefore, we will not directly use the skew and kurtosis but the coefficients of skew and kurtosis. We will refer them as hypsometric skew and hypsometric kurtosis respectively. These two coefficients are dimensionless parameters defined as:

$$HypSkew = \frac{\mu_3}{(\sigma)^3} \tag{10}$$

$$HypKurtosis = \frac{\mu_4}{(\sigma)^4} \tag{11}$$

A new function g(x) can be defined as the density function of the hypsometric curve:

$$g(x) = f^{'}(x) = a_1 + 2a_2x + 3a_3x^2 \tag{12}$$

By following the same reasoning as for f(x), we can also define the moments and coefficients of skew and kurtosis of this density function. We will denote these statistic moments of the density function of the hypsometric curve as density skew and density kurtosis (Harlin, 1978; Luo, 2000).

In statistics the coefficients of skew and kurtosis describe the shape of a distribution with respect to the normal distribution. Skew represent the asymmetry of a distribution with respect to the mean, while kurtosis is used to measure the "peakness" or "flatness" of a distribution with respect to the normal distribution. A positive value of skew indicates that the variable takes high values frequently and, therefore is skewed to the right. The skew is 0, when the variable distribution is symmetrical. Larger kurtosis (>3) indicates a "sharper" peak than normal distribution (we assumed the kurtosis of a normal distribution equal to 3); smaller kurtosis indicates "flatter" peak than normal distribution.

According to Harlin (1978) and Luo (2000) these statistics, when applied to the distribution function of the hypsometric curve, can be interpreted in terms of erosion and basin slope. The hypsometric skew represents the amount of headward erosion in the upper reach of the basin, while the density skew denotes the slope change (Harlin, 1978; Luo, 2000). The hypsometric kurtosis can be interpreted as the erosion on both upper and lower reaches of a basin, while density kurtosis depicts midbasin slope (Harlin, 1978; Luo, 2000).

These statistical moments can be used to describe and characterise the shape of the hypsometric curve and, hence, to quantify changes in the morphology of the drainage basins. In many cases, these parameters are very useful for the hypsometric analysis, especially in basins with similar hypsometric integrals but different shapes.

3. METHOD

The method that we propose in this work is based on the extraction of height and area data from DEMs by using the raster data model of ArcGIS. A DEM can be represented as a regularly raster surface or grid. A grid consists of a rectangular array of uniformly spaced cells with height values. Depending on the type of data that a cell can represent, a grid can be either integer (if the cells store integer values) or float type (if the cells store decimal values).

Integer grids in ArcGIS have an attribute table associated with them, which does not provide information of simple cells but from cell values and their distribution. An attribute table basically has two fields: "value" (which stores the cell's unique value) and "count" (which contains the number of cells with that value). If the grid represents a DEM, its attribute table will contain elevation values. Since the cells are regular squares, the number of cells is a direct measurement of the area. Therefore, the attribute table of a DEM (if it is a raster-integer type) has values of elevation ("value" field) and area ("count" field) and, through a simple algorithm, it is possible to obtain relative heights (h/H) and relative areas (a/A).

The method we propose has three main steps: i) extracting a DEM with the shape of the drainage basin; ii) transforming the DEM to an integer (if it is not integer-type) and obtaining the related attribute table; and iii) calculating relative areas and relative elevations and extracting the statistic moments of the curve (Fig. 3). To obtain a DEM with the shape of a drainage basin, we use a clip method. This method uses as input a shapefile representing the drainage basin and a DEM covering the extension of this shapefile. First it extracts a part of the DEM that coincides with the rectangular envelope of the shapefile, and subsequently it discards all the cells falling outside the shapefile boundary by assigning them a "No-Data" (null) value.

If the input DEM is not an integer raster, it is transformed to an integer-type first. The integer transformation can be made by rounding or truncation. The ArcGIS predetermined transformation is made by truncating the decimal value. This transformation gives greater errors than rounding, because it discards the decimal part. For example, the two values of 1.1 and 1.9 yield the same integer value of 1 by truncation. In order to apply a rounded-down transformation, a value of 0.5 is added to the input raster prior to truncating the decimal values.

The calculation of relative elevations and relative areas from the attribute table is made by a simple algorithm that involves only summations. Values of relative elevations can be extracted directly from the "value" field in the attribute table, whereas values of relative area can be obtained by summations of the "count" field.

Once the hypsometric curve is obtained with the area-altitude data of the basin, its statistic moments can be calculated. In order to obtain these statistics moments, the hypsometric curve is fitted to a 3rd order polynomial function by regression, using the least square fit to get the coefficients a_0, a_1, a_2, and a_3 (Equation (2)). With these coefficients it is possible to obtain the statistics moments of the hypsometric curve and the density function by using the summation expressions defined by Harlin (1978), which, in turn, permit to calculate the hypsometric integral, hypsometric skew, hypsometric kurtosis, density skew, and density kurtosis.

4. THE PROGRAM

The program CalHypso serves as an extension tool for ArcMap (ArcGIS Desktop). The extension has been developed in Visual Basic 6 programming language as a dynamic dll library. The program uses ArcObjects from ArcGIS to access spatial analyst algorithms. ArcObjects are previously designed objects based on Microsoft's Component Object Model. Using modeling language integrated in GIS provides advantages for spatial modeling

in many areas (Karssenberg, 2002; Karssenberg and de Jong, 2005; Seong and Choi, 2007). It is possible to design tools that use GIS pre-programmed functions and access the generic tools for data management and visualization (Lan et al., 2007).

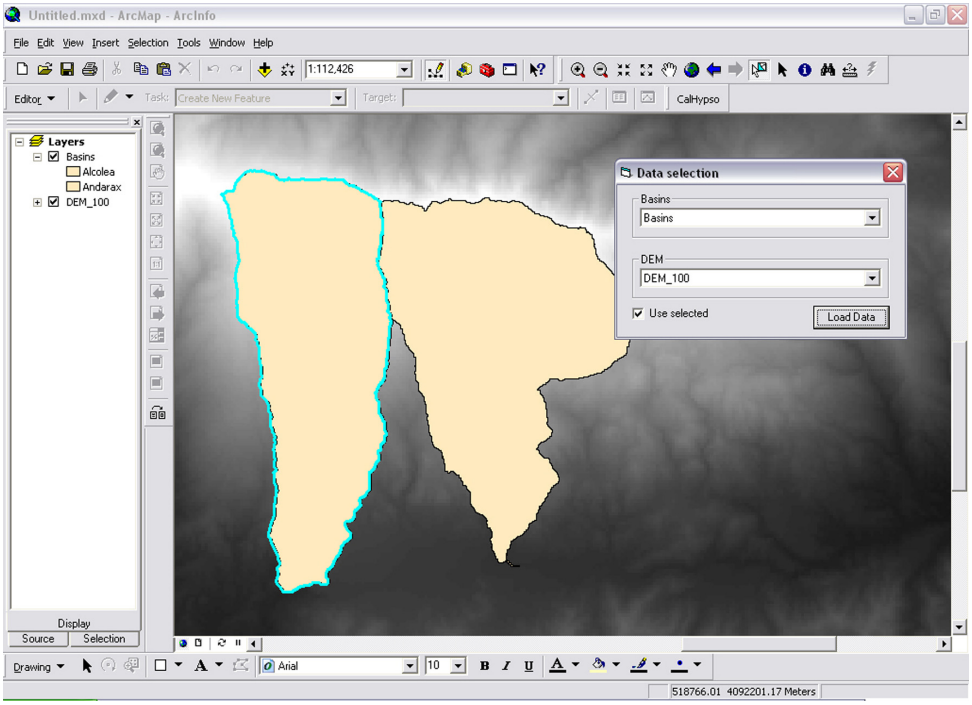

Figure 2. CalHypso extension within ArcMap environment.

The extension is in the form of a command button (ICommand) that is integrated in the ArcGIS Desktop modeling environment (Fig. 2). It is composed basically of three main windows that allow the user to select the data for the analysis, visualize the hypsometric curves for the selected data, and extract the main parameters (statistical moments) related with the curves. The extension uses as inputs a polygon shapefile with the drainage basins and a digital elevation model covering the complete extension of this basin shapefile. It allows analysis of all the basins in the shapefile or only of previously selected basins. The extension extracts the curves following the method explained above, and represents them in a graphic window within the ArcMap environment (Fig. 2). It provides a user-friendly interface with different options to visualize the style properties of the curves (Fig. 3), such as colour and size. A visual comparison between curves or curve groups becomes easy, since they can be loaded together and represented by groups, by pairs, etc., directly in a

graphic window within the ArcMap program. The extension also provides graphic and text (XY values for each curve) outputs.

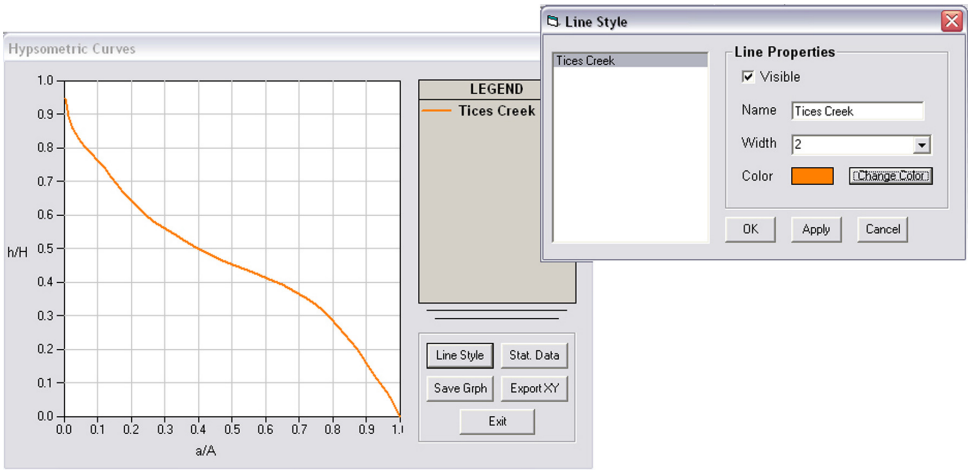

Figure 3. Main window of CalHypso program in which hypsometric curves of the selected basins are represented. The program has different options to visualize hypsometric curves and change their appearance. It also provides text and graphic outputs.

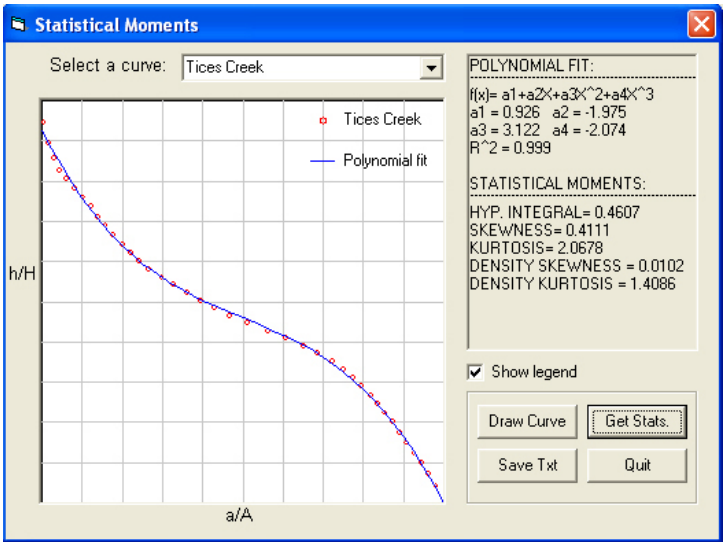

Figure 4. Statistical window of CalHypso program. This window allows the user to perform a regression analysis by using least squares fit on the curve in order to extract the main statistical moments of the selected hypsometric curve.

The third window calculates the statistical moments for each curve (Fig. 4) by performing a polynomial regression on the curve and using the methodology described by Harlin (1978).

5. CASE STUDY

In order to test the program, we performed a hypsometrical analysis in eight basins of the eastern border of the Sierra Nevada dome (Betic Cordillera, SE Spain). We selected four basins on the northern slope and four on the southern slope of the easternmost part of Sierra Nevada.

5.1. Geology, tectonic, and geomorphological setting

The Sierra Nevada dome, which includes the highest peaks on the Iberian Peninsula (e.g., Mulhacén, 3482 m), is one of the E-W folds of the Betic Cordillera generated as a consequence of the N-S convergence between Africa and Europe (Dewey et al., 1989; García-Dueñas et al., 1992; de Mets et al., 1994). In detail, the Sierra Nevada dome has been formed by the interference between two orthogonal sets of roughly N-S and E-W open folds (see arguments in Martínez-Martínez and Soto, 2002; Martínez-Martínez et al., 2004). Whilst in the western border of the Sierra-Nevada dome both sets of orthogonal folds can be found, the relief of the eastern border can be explained only by a large-scale E-W open-fold with a hinge plunging eastwards and minor sub-parallel folds (Fig. 5).

The northern and southern slopes of the eastern termination of the Sierra-Nevada dome are both geomorphologically and tectonically very different from each other. On the northern slope, the Neogene sediments of the Guadix-Baza basin lie unconformably over the basement rocks of the Sierra Nevada dome, lacking any significant faulting (Fig. 7). On the contrary, the southern slope is more structurally complex, with several fault sets striking parallel to the mountain front (Fig. 5). These faults are mainly normal and strike-slip faults, which have been interpreted as transfer faults related with the westward migration of the extension (see Martínez-Martínez et al., 2006 for details).

The drainage network of both the northern and southern slopes of the dome are bedrock channels. Seven of the eight drainage basins examined drain eastwards to the Mediterranean Sea through the Andarax river. Only the Alcolea river (the westernmost river of the southern slope) belongs to a different drainage system (Adra river drainage-basin), but it also discharges to the Mediterranean Sea (Fig. 6).

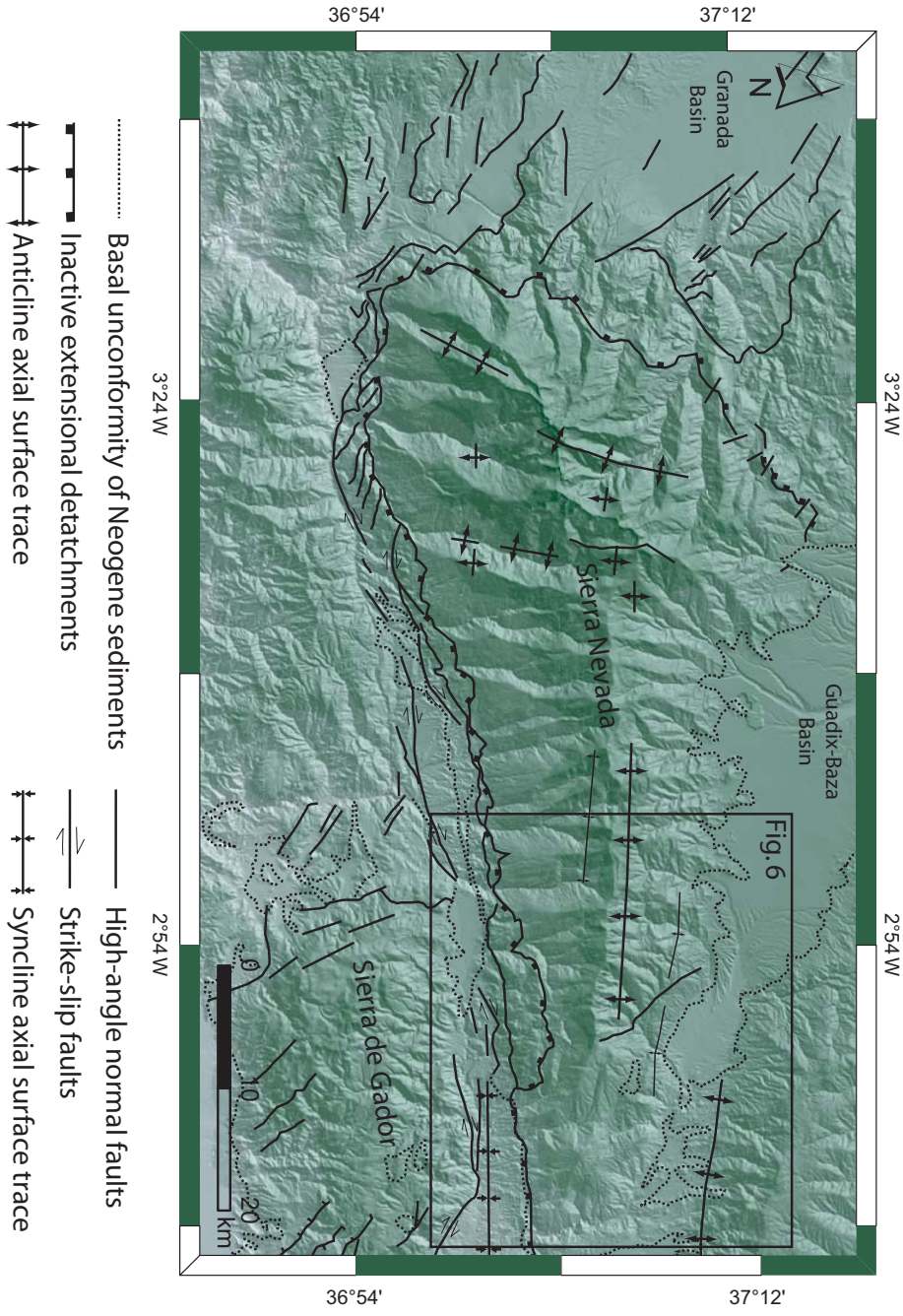

Figure 5. Neotectonic map of Sierra Nevada. Structures are taken from Martínez-Martínez et al. (2006). Map shows tectonic differences between the north and south slope, which is fault-controlled.

Rivers from the northern slope of Sierra Nevada in Pliocene times drained into an endorheic basin (Guadix-Baza basin) filled in with alluvial and lacustrine sediments (Fernández et al., 1996). At present, the drainage of this basin is external mainly towards the Atlantic Ocean via the Guadalquivir river system and towards the Mediterranean via the Nacimiento-Andarax river system (Calvache and Viseras, 1997).

5.2. Hypsometric analysis

With the aid of the CalHypso extension, we extracted the hypsometric curves for eight drainage basins of the eastern termination of the Sierra Nevada dome (Fig. 7). We have used a DEM of 100 m of pixel resolution. The model resolution is not an important issue in the hypsometric and practically do not affect to its shape (Hurtrez et al., 1999). At first sight, there are clear differences between the curves from the northern and southern slopes (Fig. 7).The curves of the southern slope have very similar slightly convex shapes

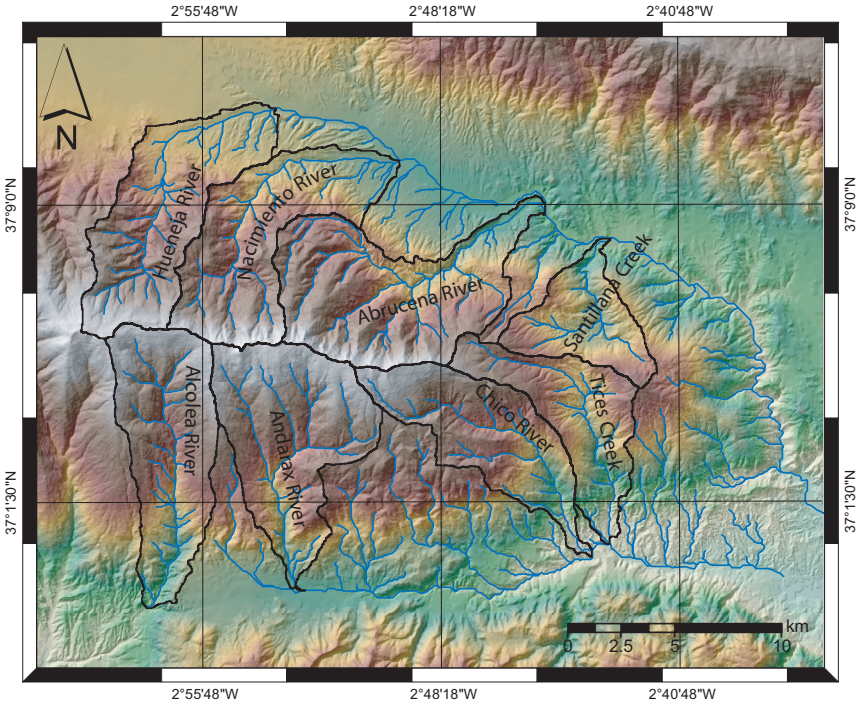

Figure 6. Selected basins of the eastern end of Sierra Nevada Dome (SE, Spain). All basins drain into the Mediterranean Sea through the same system except Alcolea river, which drains into the Mediterranean system through a different river network.

(with the single exception of the Rambla de Santillana creek) and higher hypsometric integral values than the ones on the northern slope (Fig. 7). On the other hand, the curves for the northern slope have varied shapes, although with interesting patterns. They all have the same upper part (from a/A=0 to a/A=0.1), with a high gradient in the slope curve that then changes (from a/A= 0.2 to a/A=1) ranging from concave shapes in the west (Hueneja river) to slightly convex shapes in the east (Rambla de Santillana Creek) (Fig. 7). Also noteworthy is the similar shapes of the curves for Rambla de Santillana Creek and Rambla de Tices Creek (Fig. 7), both located at the easternmost end of the Sierra Nevada dome, but in the northern and southern slopes respectively (Fig. 6).

We have also extracted the main statistical moments for the analysed hypsometric curves (Fig. 8). In the case of the southern slope, these statistics provide valuable information since the curves present very similar shapes and hypsometric integral values. The values of the hypsometric kurtosis and density kurtosis decrease slightly eastwards, whilst the values for the hypsometric skew and density skew are very similar (Fig. 8). In the curves from the north slope of the Sierra Nevada dome there is also a decrease in hypsometric kurtosis and density kurtosis values eastwards (Fig. 8). In this border, the other statistics present clear trends, with an eastward increase in hypsometric skew and density skew (Fig. 8). The values of the hypsometric integral are higher in the southern border.

5.3. Discussion

The convexity of the hypsometric curve is an indicator of the erosional stage of the basin (Strahler, 1952; Ohmori, 1993). Younger less eroded basins yield convex shapes with higher hypsometric integrals. All the curves of the eastern termination of the Sierra Nevada (north and south slope) were formed when the range started to develop, thus having roughly the same age. As climatic and lithologic factors are very similar in both slopes, the differences in the curves of the north and south slope (Fig. 7) can be attributed to tectonic factors. The southern mountain front is fault-controlled (Martínez-Martinez et al., 2006), while the northern one has no relevant faults (Fig. 5). The faults in the southern mountain front have been active during the Quaternary, having uplifted the footwalls, where the catchments are located. This relative uplift is responsible for a continuous base level lowering in the rivers, thus maintaining high vertical erosion rates. Therefore, the basins of the southern slope of Sierra Nevada have been suffering continuous rejuvenation process and preserving convex profiles over time. The area below the hypsometric curve portrays the amount of material left after erosion. Thus, when the curve gradient becomes higher in its upper part the amount of material left after erosion is smaller (Strahler, 1952; Harlin, 1978; Luo 2000). This fact can be considered a sign of maturity of the basin, since it indicates that the lateral

erosion must have been intensive in the river head (Ohmori, 1993; Keller and Pinter, 2002) (Fig. 1b).

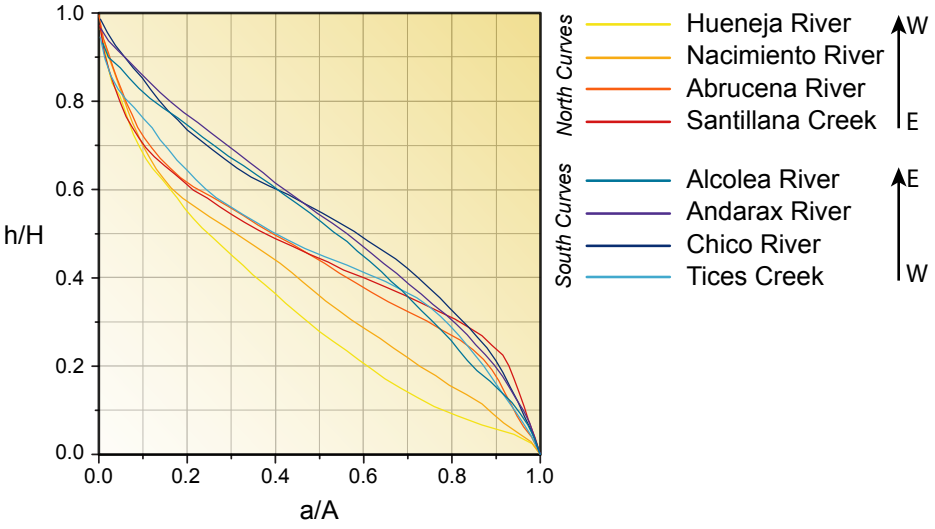

Figure 7. Hypsometric curves for 8 selected basins. Curves of the north slope have different shapes and are more concave that those of the south slope. Pattern shown by the curves from the north slope of Sierra Nevada dome indicates that the drainage basins of the east were captured previously (see text for further explanation).

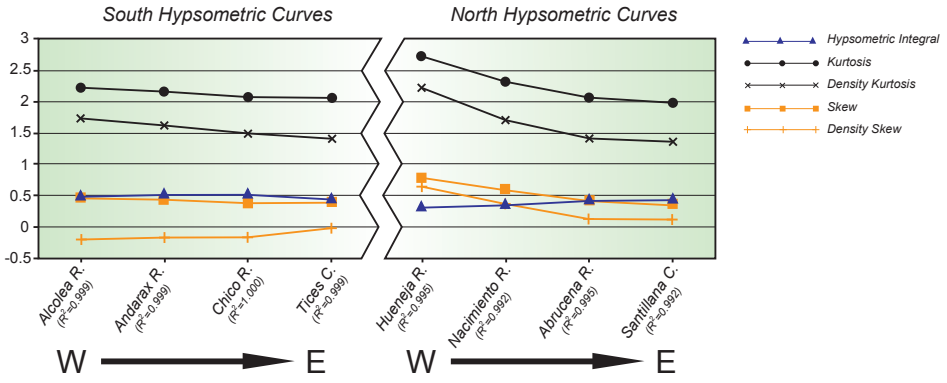

Figure 8. Values of main statistical moments of the hypsometric curves for the analysed drainage basins (see text for details). Correlation coefficients (R^2) from the regression analyses are indicates for each hypsometric curve.

The different shapes of the hypsometric curves in the northern slope of the Sierra Nevada dome (Fig. 7) are the result of a capture process of the drainage in the southernmost part of the Guadix-Baza Neogene basin. All the curves present the same upper section (from a/A=0 to a/A=0.1) with a high gradient (typical of a stage of maturity as explained before) (Fig. 7). The remaining sections of the curves progressively change from concave in the westernmost rivers (Hueneja river) to convex in the easternmost one (Santillana river) (Fig. 7). This eastward steepening in the lower sections of hypsometric curves might be related to the capture process of the catchments previously draining to the North into the Guadix-Baza basin. This capture process would generate a base level lowering and, consequently, an incision wave progressing headwards. We envisage this headward erosion as downcutting narrow canyons in the lowermost parts of the captured catchments, which in turn, would generating a convex profile. This would be reflected in the hypsometric curve as a progressive increase in concavity in the "mouth" part (Fig. 9). As this process advances over time, different curve shapes give an idea of the relative chronology of this piracy process. The differences between the curves indicate a necessary time interval between the capture in the easternmost drainage basins and the ones located westward of this position, thus revealing that the capture process advances progressively and may still be active.

The statistical moments of the hypsometric curves also provide information of the evolution of erosion around the Sierra Nevada. In this regard, an analysis of the hypsometric integral values is not sufficiently representative, since the curves of the southern slope present very similar values but slightly different shapes (Fig. 7). Nevertheless, an analysis of the other statistical moments related to the hypsometric curve can be more revealing. According to Harlin (1978) and Luo (2000, 2003), the statistics of the hypsometric curve can be interpreted in terms of erosion and basin slope. Hypsometric kurtosis and density kurtosis values decrease estwards in both the northern and southern curves, thus indicating a decrease in erosion in the lower and upper reaches of the basins (Fig. 8) (Harlin, 1978; Luo 2000). Assuming that lithology does not play an important role in making these differences, and that climate is homogeneous all over (this region).It is noteworthy that the more active structures in the Sierra Nevada dome are located towards its western border (Martínez-Martínez and Soto, 2002; Martínez-Martínez et al., 2004), and some authors have proposed a westward migration of the tectonic activity (Azañón et al., 2004; Martinez-Martinez et al., 2006). Thus, this hypsometric analysis also fits with a westward migration of tectonic activity in the Sierra Nevada.

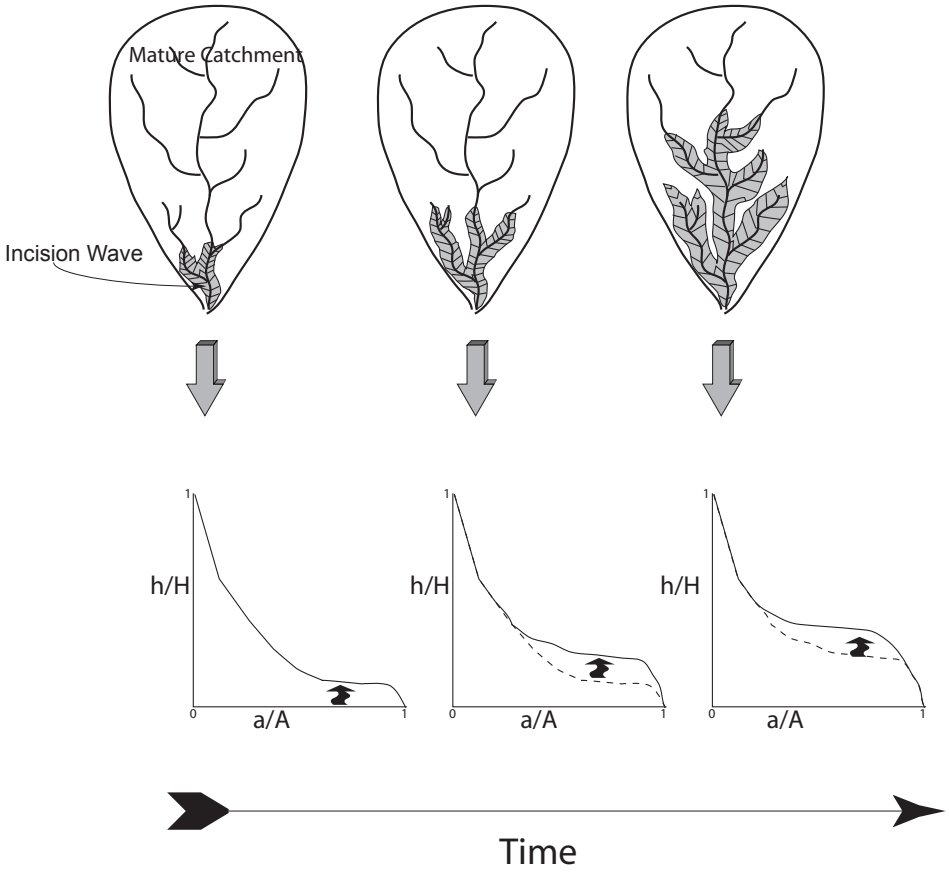

Figure 9. Schematic drawing (not to scale) showing the effect that a capture process, with a subsequent base-level lowering, will have in a mature drainage basin over time. Dashed line in the hypsometric curves represents the "previous" stage.

6. CONCLUSION

In this work we have presented CalHypso, a new ArcGIS extension to extract hypsometric curves from Digital Elevation Models. This extension applies a new methodology based on the integer data model of ArcGIS and, therefore, it operates efficiently within this GIS environment. The main advantage of this extension is that the user can extract multiple hypsometric curves directly within the ArcGIS software and calculate the main statistics related to these hypsometric curves, such as kurtosis, density kurtosis, skew, density skew, and the hypsometric integral. As an example, we have made an analysis in rivers of the eastern sector or the Sierra Nevada dome in SE Spain. The differences between the nor-

thern and southern slope hypsometric curves fit with the main tectonic setting envisaged for both mountain fronts. The southern slope curves show a younger erosional stage due to the tectonic activity along the faults bounding the mountain front. The northern slope reveals patterns in curve shapes due to basin rejuvenation induced by a capture process. The statistics related to the hypsometric curves also provide useful information regarding erosion processes. These erosion rates in the Quaternary decrease eastwards, thus suggesting a decrease in tectonic activity in the same direction.

Acknowledgements: This study was supported by the grants BTE2003-01699, CGL2004-03333/BTE, and TOPO-IBERIA CONSOLIDER-INGENIO CSD2006-00041 of the Spanish Ministry of Education. We are indebted to Christine Laurin for revising the English. We also thank the useful comments provided for two anonymous reviewers that help us to improve the scientific quality of this work.

5

Quaternary landscape evolution and erosion rates for an intramontane Neogene basin (Guadix–Baza basin, SE Spain).

J. V. Pérez-Peña[(1)*], J. M. Azañón [(1,2)], A. Azor[(1)], P. Tuccimei[(3)], M. Della Seta[(d)] and M. Soligo[(3)]

(1) Departamento de Geodinámica, Universidad de Granada, Granada, Spain
(2) Instituto Andaluz de Ciencias de la Tierra (UGR-CSIC)
(3) Universitá Roma Tre. Dipartimento di Scienze Geologiche, Roma, Italy
(4) Universitá degli Studi di Roma "La Sapienza". Dipartimento di Scienze della Terra, Roma, Italy
* Correspondence to: JV Pérez-Peña, Departamento de Geodinámica, Campus Fuentenueva s/n, Universidad de Granada, 18071 Granada, Spain. E-mail: vperez@ugr.es

ABSTRACT: The landscape evolution in Neogene intramontane basins is a result of the interaction of climatic, lithologic, and tectonic factors. When sedimentation ceases and a basin enters an erosional stage, estimating erosion rates across the entire basin can offer a good view of landscape evolution. In this work, the erosion rates in the Guadix–Baza basin have been calculated based on a volumetric estimate of sediment loss by river erosion since the Late Pleistocene. To do so, the distribution of a glacis surface at ca. 43 ka, characterised by a calcrete layer that caps the basin infilling, has been reconstructed. To support this age, new radiometric data of the glacis are presented. The volume of sediment loss by water erosion has been calculated for the entire basin by comparing the reconstructed geomorphic surface and the present-day topography. The resulting erosion rates vary between 4.28 and 6.57 $m^3\ ha^{-1}\ yr^{-1}$, and are the consequence of the interaction of climatic, lithologic, topographic, and tectonic factors. Individual erosion rates for the Guadix and Baza sub-basins (11.80 $m^3\ ha^{-1}\ yr^{-1}$ and 1.77 $m^3\ ha^{-1}\ yr^{-1}$ respectively) suggest different stages of drainage pattern evolution in the two sub-basins. We attribute the lower values obtained in the Baza sub-basin to the down-throw of this sub-basin caused by very recent activity along the Baza fault.

Keywords: Landscape evolution; Erosion rates; Guadix–Baza basin; GIS, River capture; U/Th dating

Geomorphology (2009)
DOI:10.1016/j.geomorph.2008.10.018
Received 11 July 2008
Revised 27 October 2008
Accepted 29 October 2008

1. INTRODUCTION

The study of Quaternary and present-day tectonic activity of mountain belts is mainly based on seismologic, geodetic, geomorphologic, and geologic data. In regions subject to low/moderate tectonic rates, geomorphologic and geologic data provide the best approach for the characterisation of active tectonics. Along these lines, geomorphic features and structural data have been used to qualitatively evaluate recent tectonic activity (e.g. Molin et al., 2004; Dumont et al., 2005; Necea et al., 2005). Geomorphic approaches such as analyses of drainage patterns and river incision rates have become standard tools in tectonic studies (e.g. Azor et al., 2002; van der Beek et al., 2002; Wegmann and Pazzaglia, 2002; Zhang et al., 2004). However, geomorphic processes are controlled by a number of topographic, climatic, and lithological factors that must be taken into account when deriving tectonically oriented conclusions.

River incision rates and long-term erosion rates are classic issues concerning fluvial geomorphology (e.g. Burbank et al., 1996; Dadson et al., 2003; Pratt-Sitaula et al., 2004; Whipple, 2004; Stock et al., 2005). These rates have been estimated using geomorphic markers and often related to uplift and tectonics (Small and Anderson, 1998; Small, 1999; Schildgen et al., 2007; Reinhardt et al., 2007a, b). The recent development of GIS allows calculating eroded volumes by comparing digital terrain models of present-day and relict geomorphic surfaces, thus enabling a spatial analysis of erosion rates (Brozovic et al., 1995; Schildgen et al., 2007). However, the interpretation of incision and erosion rates is complex since diverse processes can produce similar results. In fact, in addition to tectonics, a number of factors related to fluvial dynamics can be responsible for river entrenchment such as discharge variations, bedload decreases, and base-level lowering. Some of these factors may be climatically controlled, while others are mostly controlled by riverbed lithology.

In this paper, we analyse the drainage pattern evolution and river incision in an essentially flat elevated region during the Quaternary. The study focuses on the Guadix–Baza basin, a Neogene–Quaternary sedimentary basin of the Betic Cordillera in SE Spain (Fig. 1). This basin provides an excellent setting to analyse river-incision rates since it depicts a former endorheic sedimentary basin that was incorporated into an external drainage system (the Guadalquivir river) during the Late Pleistocene. The basin has been geomorphologically studied and a relict geomorphic surface has been radiometrically dated. This geomorphic surface is a residual glacis that developed at the top of the sedimentary infilling, thus recording the final deposits in the former endorheic basin, prior to the development of the present-day external drainage pattern. This glacis is formed by a laminar calcrete that has

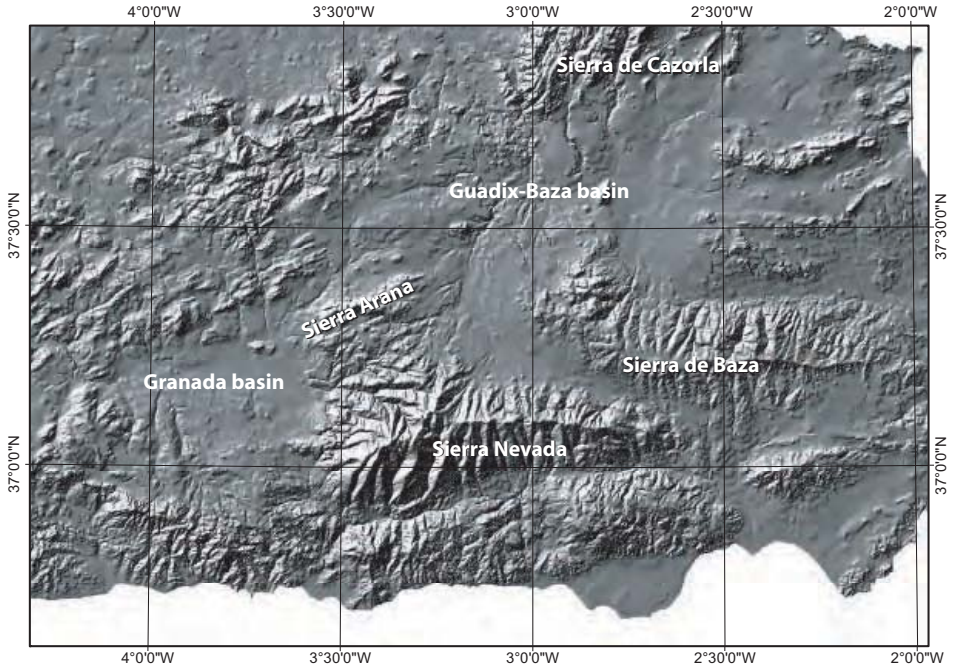

Figure 1. Digital elevation model (DEM) showing the main Neogene basins and ranges of the western part of the Betic Cordillera.

been dated with U/Th, thereby allowing an estimation of the Late Pleistocene incision rates of the drainage network.

We have analysed long-term erosion rates within the Guadix–Baza basin by reconstructing the original morphology of the relict glacis surface. This analysis provides a better knowledge of the Quaternary landscape evolution of the Guadix–Baza basin and interesting links among erosion, topography, and recent tectonic activity.

2. GEOLOGICAL AND GEOMORPHOLOGICAL SETTINGS

2.1. Geological setting

The Guadix–Baza basin is a Neogene intramontane depression of the Betic Cordillera. The basin blankets the contact between the Internal and the External Zones of the Cordillera. Its basement comprises Mesozoic carbonate rocks (External Zones) in its northern sector and Triassic metamorphic rocks (Internal Zones) in the southern sector (Fig. 2). The sediment fill is markedly continental and extends from the Late Tortonian to the Upper

Pleistocene (Vera, 1970; Viseras, 1991; Fernández et al., 1996). Palaeogeographically, this basin was an endorheic depression bounded by prominent reliefs during its continental filling. Its Pliocene–Pleistocene sedimentary record suggests a genetic model with alluvial fans on the borders that gradually connected by means of channel systems with a large central lake (Viseras, 1991; Fernández et al., 1996). On the southern and eastern borders of the Guadix sub-basin, the continental fill is formed by an alternation of poorly cemented conglomerates and sands of the Guadix Formation (Vera, 1970); towards the central part of this sub-basin, these deposits gradually change to marls and clays (Viseras, 1991; Fernández et al., 1996). The Neogene fill of the Baza sub-basin is composed of an alternation of lacustrine and palustrine deposits together with alluvial deposits in the distal parts. The upper levels of these deposits have been dated by means of amino acid racemization ratios from ostracods, yielding ages around 280 ka (Ortiz et al., 2004).

The sedimentation in the Guadix–Baza basin ends in the Upper Pleistocene with the formation of a thick calcrete (0.5–1 m) that constitutes a residual surface or glacis (Fig. 3). This glacis, where preserved, is visible across the whole Guadix–Baza basin and has been used as a reference level to characterise active tectonics in the basin (García-Tortosa et al., 2008). Nevertheless, the age of this surface, and consequently the later endorheic–exorheic transition is still in discussion. Subsequent to the development of this glacis, sedimentation in the basin is restricted to alluvial and colluvial facies, slope deposits, and fluvial terraces.

The Pliocene–Pleistocene history of the Guadix–Baza basin seems to be dominated by sedimentary processes, with a lack of significant tectonic events. The Quaternary deformation in this basin is constrained to a few important normal faults as well as some open folds (interlimb angle 70º–120º; Ramsay and Huber, 1987) that slightly deform the glacis surface (García-Tortosa et al., 2008), some related with diapirism. The most prominent tectonic structure of this basin is the Baza fault (Fig. 2).

The Baza fault is a normal fault (37 km long) that divides the Guadix–Baza basin into two sub-basins, the Guadix sub-basin to the west and the Baza sub-basin to the east. This fault is composed of three segments with different orientations (Alfaro et al., 2007): a northern segment striking NNE–SSW, a central segment orientated N–S, and a southern one striking NW–SE (Fig. 2). Its geomorphic expression is a well preserved fault scarp, which is located between poorly cemented and highly erodible Neogene sediments. This fault produces a down-throw of approximately 100 m in the glacis. García-Tortosa et al. (2008) carried out a tectono-geomorphologic study over this fault by analysing some of its geomorphologic features such as its front sinuosity, stream-length gradient index, and river

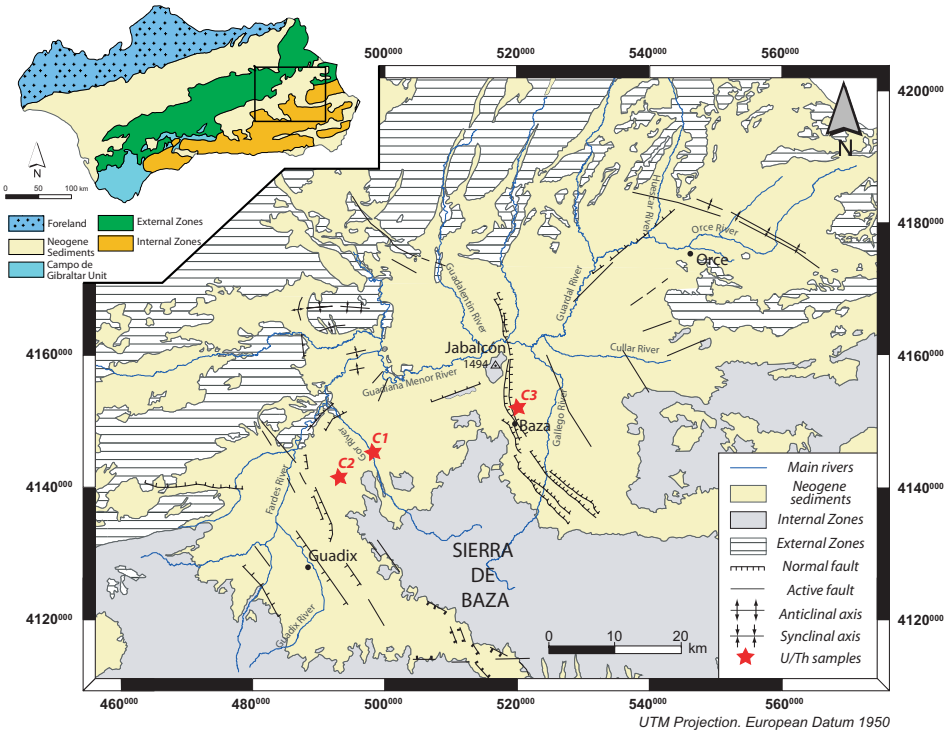

Figure 2. General geologic map of the Neogene Guadix–Baza basin indicating the main active structures (their location is taken from García Tortosa et al., 2008). The inset shows the general tectonic setting. The locations of the samples dated by U/Th are indicated. Sample C1 corresponds to the dating of Azañón et al. (2006), while C2 and C3 are the dating presented in this work.

entrenchment; results showed very recent activity. The historic activity of this normal fault is evident and its associated seismicity includes important events like the Baza earthquake of 1531 with a magnitude of 5.1 Mb, the Caniles earthquake of 1962 at 4.7 Mb, and the more recent Benamaurel earthquake of 2003 at 4.1 Mb. The focal mechanism solution for the latter earthquake corresponds with the strike and orientation of the Baza fault (Alfaro et al., 2007; García-Tortosa et al., 2008).

2.2. Geomorphological setting

The Guadix–Baza basin is surrounded by mountain ranges of the Betic Cordillera (Sierra Nevada, Sierra de Baza, and Sierra de Cazorla) (Fig. 1), with an external drainage system to the Atlantic Ocean through the Guadalquivir river. Its present morphology

consists of a high plateau with a mean elevation of 1,000 m, intensely dissected by the river network (Fig. 1). This plateau constitutes the silting level of the basin and it is well preserved in many places. The present drainage network is organised around various main rivers, which can develop wide valleys (up to 1 km in the north near the capture point by the Guadalquivir river) as well as sub-vertical canyons more than 200 m deep. The sectors between the elevated glacis and the main river valleys are dominated by erosional processes producing badland topography (Fig. 3).

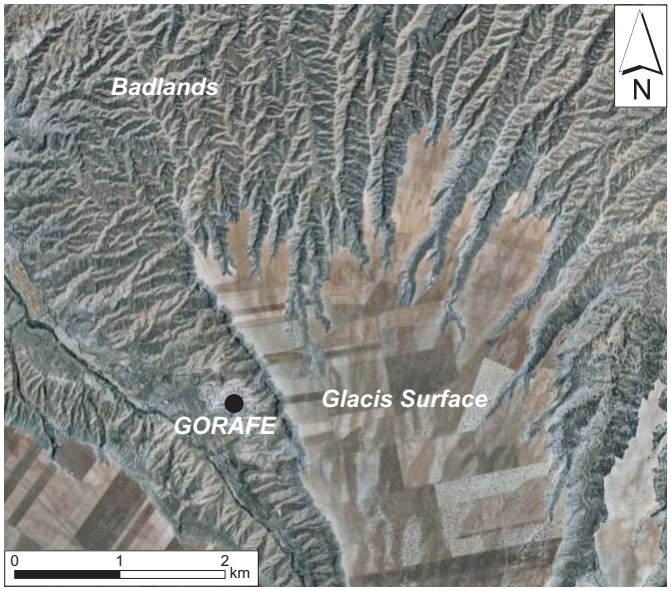

Figure 3. Colour ortho-photography where the surface of the glacis is visible, cut by the erosion of rivers forming badlands.

One of the most discussed points of the Quaternary evolution of the Guadix–Baza basin is the age of the capture of the former endorheic drainage by the Guadalquivir river system. Determination of this age is a crucial point for calculating erosion rates. The capture is associated with the end of sedimentation in the basin, when the drainage changed from endorheic to exorheic.

Some authors have proposed that the maximum age for this endorheic–exorheic transition can be constrained by the youngest Neogene sediments in the basin. Vera (1970) and Calvache and Viseras (1997) proposed in this regard that the capture took place in the middle to late Pleistocene, taking as a reference the age of the Solana del Zamborino palaeontological–archaeological site (100 ka) (Botella et al., 1985). Ortiz et al. (2004) and

Scott et al. (2007) proposed different ages for the youngest sediments in the basin: 280 ka (amino acid racemization ratios in ostracodes) and 450 ka (based on magnetostratigraphy) respectively. All these approximations give a maximum age for the capture of the drainage of the basin, since all of them are related to endorheic sedimentation. Moreover, they require a very detailed knowledge of the basin sedimentation.

A different approach can be obtained by dating deposits subsequent to the river entrenchment, giving a minimum age for the endorheic–exorheic transition in the Guadix–Baza basin. Díaz-Hernández and Juliá (2006) dated a petrocalcic layer that caps the uppermost geomorphologic unit yielding an age of 350 ka. In contrast, Azañón et al. (2006) dated the laminar calcrete that forms the glacis surface obtaining an age of 43 ± 6 ka, hence indicating that the endorheic–exorheic transition is younger than this age.

3. NEW GEOCHRONOLOGICAL DATA

In order to better constrain the age for the endorheic–exorheic transition, we have dated two samples (C2 and C3, Fig. 2) from the glacis surface by the α-counting U/Th method. The first sample is from a lower calcrete situated a few meters below the uppermost calcrete that forms the glacis surface. This sample yields an age of 68 ± 6 ka, a bit older than the one found by Azañón et al. (2006) for the uppermost calcrete (C1 in Fig. 2). This age has been obtained using a single sample from the laminar calcrete facies. The sample is slightly contaminated with a detrital fraction as can be inferred by a $^{230}Th/^{232}Th$ activity ratio ranging around 9 (Table 1), a value indicating the presence of a moderate amount of ^{232}Th accompanied by ^{230}Th not formed by radioactive decay of co-precipitated U. In order to account for the presence of inherited ^{230}Th, it was necessary to apply a correction. Since only one sample from the laminar layer of the calcrete was available, the isochron technique using total sample dissolution (Bischoff and Fitzpatrick, 1991) was not an option. Therefore, the approach for applying the correction was to consider the initial $^{230}Th/^{232}Th$ activity ratio in the laminar calcrete as equal to that of the detrital fraction and on this basis correct the $^{230}Th/^{234}U$ activity ratio of the sample (Kaufman and Broecker, 1965; Tuccimei et al., 2006). The value chosen for this correction (0.83) was deduced from the analysis of the younger calcrete, hypothesizing a similar composition for the detrital fraction in both calcretes. This value is the intercept on the Y axis of the straight line that best estimates the relationship in the younger Guadix calcrete data plotted on the $^{230}Th/^{232}Th$ – $^{234}U/^{232}Th$ space (see Fig. 11 in Azañón et al., 2006).

A second sample was collected in the hanging wall of the Baza fault (C3 in Fig. 2). Four coeval sub-samples from the laminar layer of the calcrete were selected and analysed by the U-series method, according to the total-sample dissolution (TSD) technique develo-

ped by Bischoff and Fitzpatrick (1991) for dating impure carbonates. This method has been chosen over using leachates alone (Schwarcz and Latham, 1989) because the leaching method gives reliable results only in the case of selective dissolution of the carbonate fraction, without any removal of U and Th isotopes from the detrital component, or when U and Th are leached without any fractionation. Generally, this condition is not verified because U and Th are often fractionated and Th can be re-adsorbed into the residual component. When analysing samples consisting of simple mixtures of carbonate and a detrital component, the use of the TSD method is preferred to determine the age because the sample is totally dissolved and consequently no preferential leaching or re-adsorption can occur.

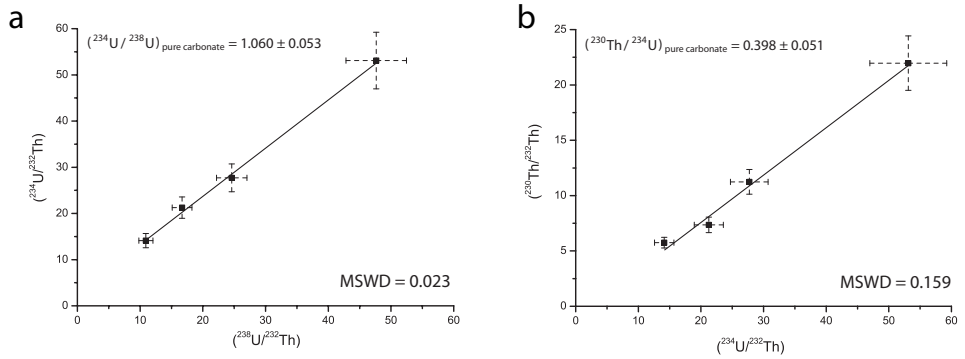

Figure 4. Isochron plots of four subsamples from the laminar horizon of the calcrete-sample. **a)** C3 $^{234}U/^{232}Th$ vs $^{238}U/^{232}Th$ plot. **b)** $^{230}Th/^{232}Th$ vs $^{234}U/^{232}Th$ plot.

Sample	*U (ppb)*	$^{234}U/^{238}U$	$^{230}Th/^{232}Th$	$^{230}Th/^{234}U$	$^{230}Th/^{234}U_{corr*}$	*Age (ka)*
C2	593 ± 18	1.535± 0.032	8.949± 0.580	0.525± 0.023	0.476± 0.029	68 ± 6

Table 1. U contents, activity ratios, and age of calcrete C2. (*) The $^{230}Th/^{234}U$ activity ratio measured for subsample C2 from the laminar horizon of the lower Guadix calcrete has been corrected using the value of 0.83 as $^{230}Th/^{232}Th$ activity ratio in the detritus at Guadix. See text for explanation.

The age of the calcrete (55 ± 9 ka) was calculated measuring the $^{230}Th/^{232}Th$, $^{234}U/^{232}Th$, and $^{238}U/^{232}Th$ activity ratios of four coeval sub-samples in order to obtain the value of the $^{230}Th/^{234}U$ and $^{234}U/^{238}U$ activity ratios in the pure carbonate fraction. These values are respectively calculated from the slopes of the regression lines in the $^{230}Th/^{232}Th$ vs $^{234}U/^{232}Th$ and $^{234}U/^{232}Th$ vs $^{238}U/^{232}Th$ isochron plots reported in Fig. 4. Calculations have been carried out using ISOPLOT, a plotting and regression program for radiogenic-isotope

data (Ludwig, 1994). Uranium and thorium concentrations, activity ratios, and ages are summarised in Table 2. Quoted uncertainties are 1 standard deviation (± 1 sigma).

S-sample	U (ppm)	$^{230}Th/^{232}Th$	$^{238}U/^{232}Th$	$^{234}U/^{232}Th$	$^{234}U/^{238}U_{carb*}$	$^{230}Th/^{234}U_{carb*}$	Age (ka)
1	0.451± .020	7.352±0.701	16.696±1.572	21.264±2.321	0.398 ± 0.051	1.060 ± 0.053	55 ± 9
2	3.069±0.196	21.968±2.461	47.650±4.828	53.115±6.129			
3	2.401 ± 0.140	11.242±1.115	24.600±2.421	27.720±3.011			
4	0.503 ± 0.029	5.756±0.481	10.917±1.124	14.133±1.539			

Table 2. U contents, activity ratios, and age of calcrete C3. (*) carb indicates the pure carbonate fraction

4. GLACIS RECONSTRUCTION AND VOLUME ESTIMATION

The methodology proposed in this work consists of reconstructing the glacis morphology prior to river entrenchment. We have used a raster Digital Elevation Model (DEM) with 20 m resolution to isolate the pixels (cells) representing the glacis and reconstruct its initial morphology. This reconstructed model can be compared with the present-day morphology of the Guadix–Baza basin and the volume of sediments eroded since the basin was captured by the Guadalquivir river system can be estimated.

The first step is to select the area to reconstruct. We have chosen only the present-day catchment area of the Guadiana Menor river (a tributary of the Guadalquivir river, Fig. 5). Only in this area where Neogene sediments are outcropping, we have the reference level of the glacis surface. Since the capture of the basin by the Guadalquivir river produced an incision wave that moved headwards, erosion rates are expected to be the greatest near the capture point and progressively decrease away from this point. Therefore, the erosion rates that we have calculated are likely underestimating the overall erosion rate of the basin.

The glacis constitutes a flat surface (with slopes less than 5°). We excluded first from the DEM those pixels with slopes greater than 5° (Fig. 6). We thereby obtained the pixels that belong to the glacis surface but also those of the valley floors. To avoid these river valley-floor pixels in our analysis, we extracted the detailed drainage network for the Guadix–Baza basin and applied a 750 m buffer to the main rivers (with the wider valleys) and a 250 m buffer for all the other rivers. From the previous slope analysis, we only considered those pixels that fell outside the area defined by the buffers.

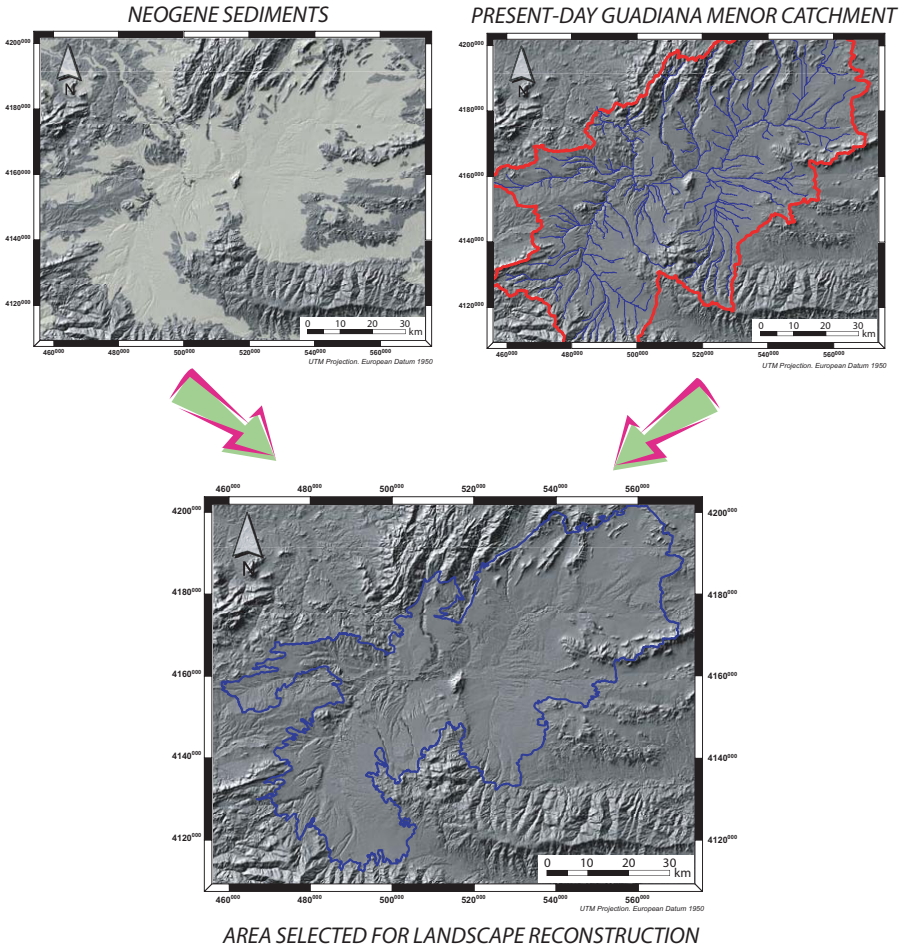

Figure 5. Area where the glacis surface has been reconstructed. This area comprises the actual drainage area of the Guadiana Menor river occupied by Neogene sediments of the Guadix–Baza basin.

With this double filter, slopes, and river distance, we isolated the pixels that represent the preserved glacis surface. However, this method is not enough near the basin capture-point (the Guadalquivir capture point) that corresponds with a second lower flat surface belonging to the Fardes river flood plain (Fig. 1). In this area, erosion has been greater than in other parts of the Guadix–Baza basin, the glacis is completely absent, and the rivers have the widest valleys. The second filter fails here since it is not enough to discard the pixels from the flood plain of the Fardes river, which has gentle slopes at lower elevations than those of the glacis surface. To avoid including pixels that do not represent the glacis, a de-

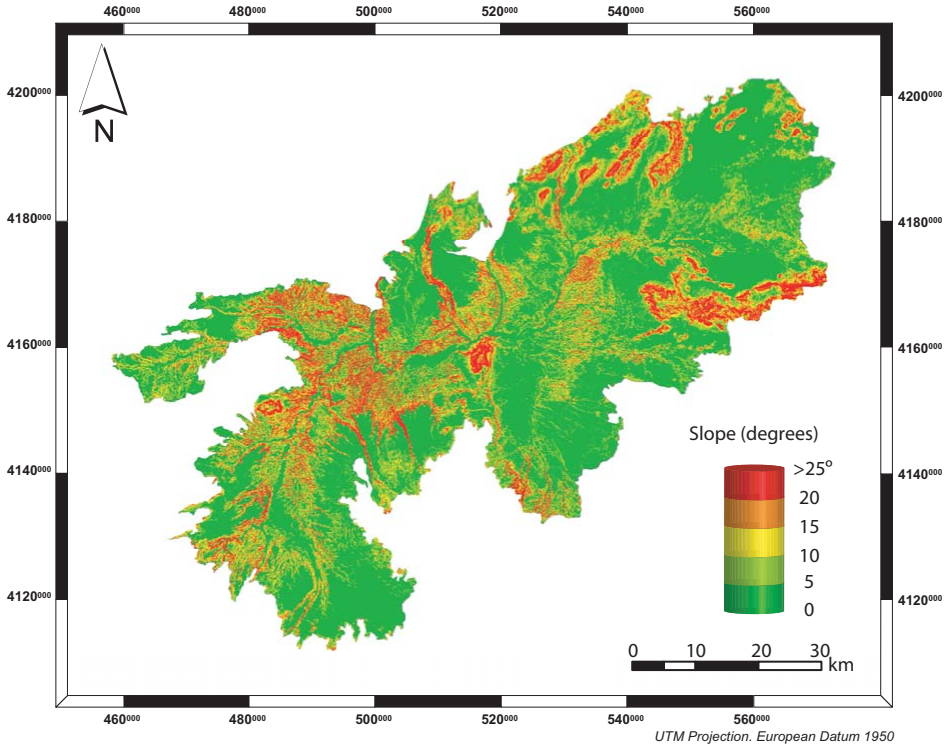

Figure 6. Slope map for the study area extracted from a 20 m DEM. Note that the gentle slopes (< 5º) correspond not only to the glacis surface but also to the valley floors.

limited area around the capture point has been discarded from the analysis. Profiles 1 and 2 in Fig. 7 show that the glacis surface is completely absent in the discarded area.

To reconstruct the glacis surface, we created a triangulated irregular network (TIN) that reproduces the morphology of the glacis surface prior to the entrenchment of the present-day drainage network (Fig. 8a). Profiles 1, 2, and 3 (Fig. 8b) (made for both the present-day and reconstructed surfaces) show that the reconstructed model adapts to the glacis morphology, even though this glacis morphology is not completely flat (Fig. 8b). Profile 3 in Fig. 8b shows that the reconstructed model adapts to the glacis morphology and, therefore, it does not overestimate elevations; this is very important to obtaining valid erosion rates for the Guadix–Baza basin.

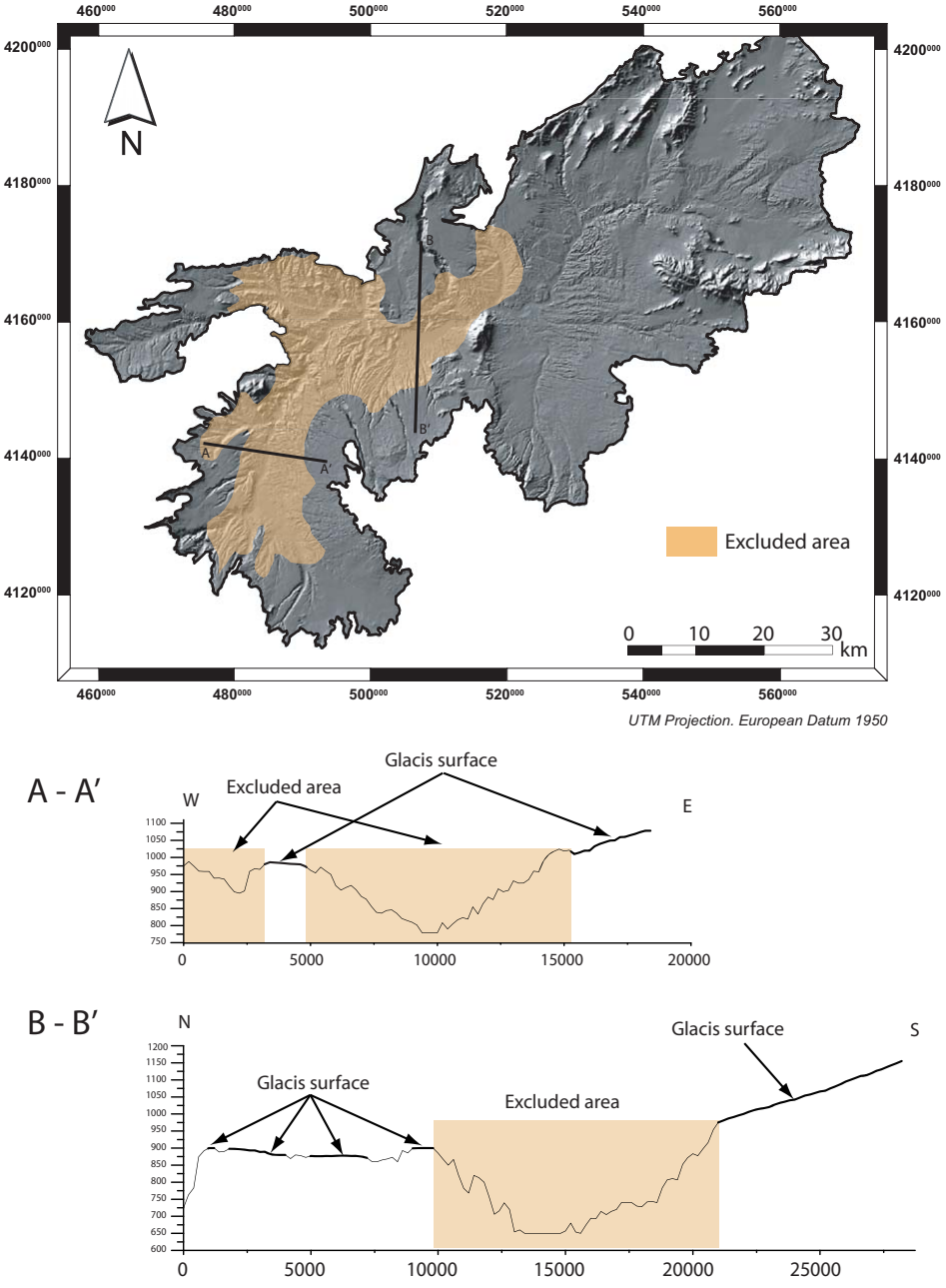

Figure 7. Excluded area around the basin capture point. The A–A' and B–B' profiles show how the glacis surface is completely absent in this excluded area. Also note that in this excluded area the valleys are wider than the considered 750 m buffer and have gentle slopes. (See text for a full explanation.).

a

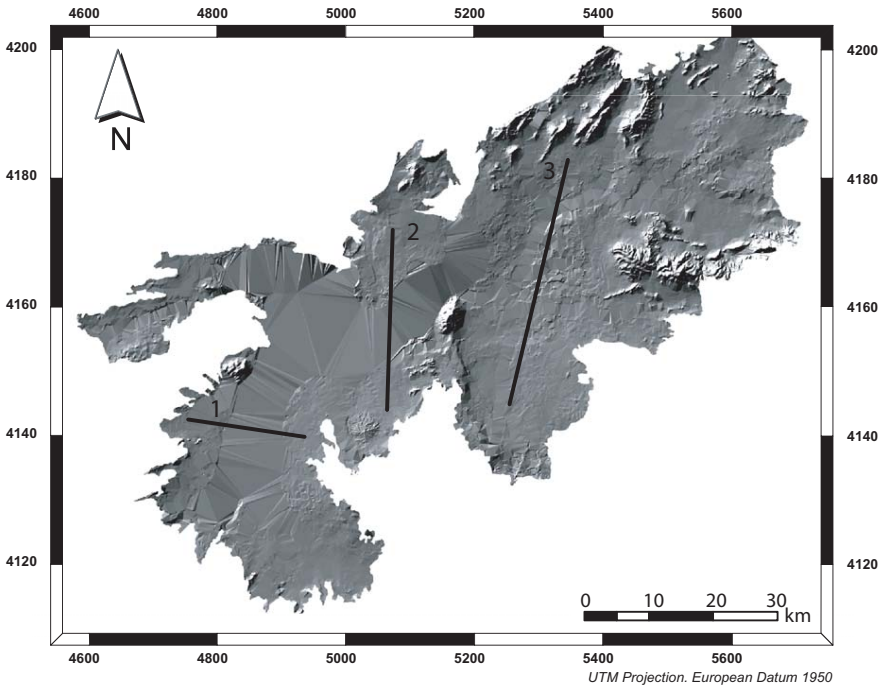
4600
4800
5000
5200
5400
5600
4200
4180
4160
4140
4120
N
1
2
3
0 10 20 30
km
UTM Projection. European Datum 1950

b

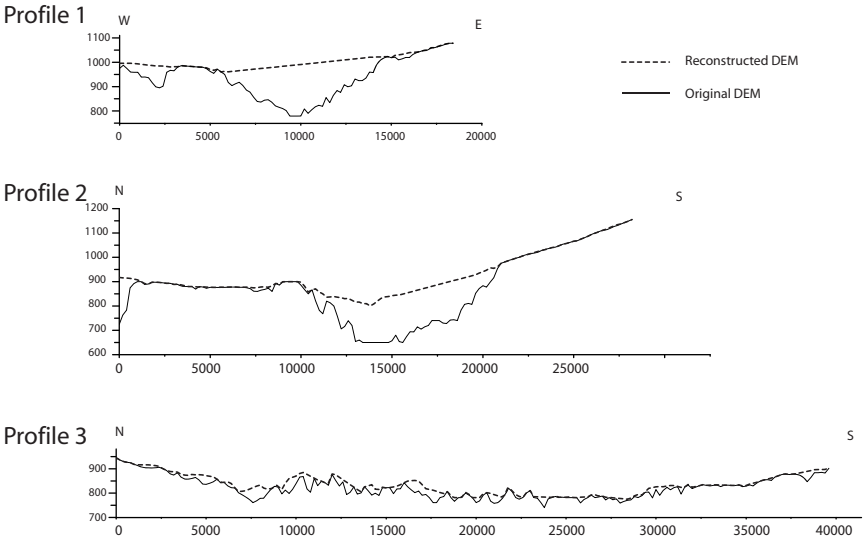
Profile 1
W
E
1100
1000
900
800
0
5000
10000
15000
20000
Reconstructed DEM
Original DEM
Profile 2
N
S
1200
1100
1000
900
800
700
600
0
5000
10000
15000
20000
25000
Profile 3
N
S
900
800
700
0
5000
10000
15000
20000
25000
30000
35000
40000

Figure 8. (Back). Reconstructed model for the Guadix–Baza basin prior to river entrenchment. **a)** Hill-shade map obtained from the reconstructed digital elevation model. **b)** Height profiles over the reconstructed and the real topography. Note that the reconstructed model never overestimates the elevation of the glacis surface, tending instead to underestimate it.

	Area (ha)		Volume (hm^3)	Rate ($m^3\ ha^{-1}\ yr^{-1}$)		Rate ($t\ ha^{-1}\ yr^{-1}$)	
	Min.	Max.		Min.	Max.	Min.	Max.
Total	429344	659382	120092	6.57	4.28	11.82	7.70
Sub-Guadix	205168	351477	103169	11.80	6.89	21.25	12.40
Sub-Baza	224176	307904	16923	1.77	1.29	3.19	2.32

Table 3. Values for surface area, volume loss by erosion, and erosion rates (taking the calcrete age of 42.6 ka as reference) for the entire Guadix–Baza basin, and for the sub-basins of Guadix and Baza separately. (See text for further explanation.)

From the present-day topography and the reconstructed model we can easily calculate the eroded volume by subtracting elevations in both models (Fig. 9). Since these models have a pixel resolution of 20 m, the elevation difference at each point is proportional to the volume. Moreover, plotting these elevation differences on a map provides an idea of how erosion is distributed within the Guadix–Baza basin (Fig. 9), hence providing an understanding of how the erosion has advanced since the basin capture.

5. EROSION RATES FOR THE GUADIX-BAZA BASIN

For the calculation of erosion rates in the Guadix–Baza basin, we used the age of 43 ± 6 ka for the glacis proposed by Azañón et al. (2006) as we considered this age more methodologically precise and found that it agrees with the new dating presented in this work. In the next Discussion chapter we will examine this choice in depth.

Since the considered area for the glacis reconstruction does not include the whole drainage area but only that occupied by the Neogene sediments, we present two erosion rates: a maximum erosion rate calculated with the volume and only the area where the glacis has been reconstructed, and a minimum erosion rate calculated by considering all the present-day drainage area (Fig. 5). Table 3 shows the results obtained as erosion rates in $m^3\ ha^{-1}\ yr^{-1}$ and $t\ ha^{-1}\ yr^{-1}$ considering a bulk sediment density of 1800 kg m^{-3}.

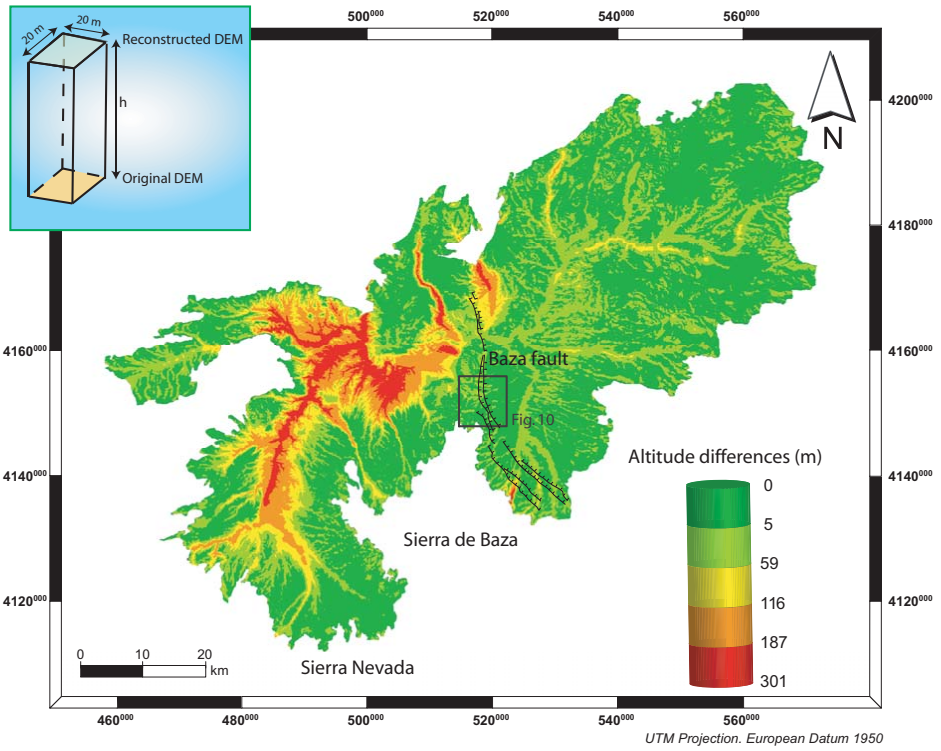

Figure 9. Elevation differences between the reconstructed and the real topography. At each point of the model, the eroded volume can be estimated by multiplying the height difference between the two models by the pixel area. Note how the erosion wave has advanced from the capture point towards the south, but is stopped to the east by the Baza Fault.

6. DISCUSSION

6.1. Considerations on the age of capture of the Guadix–Baza basin

The glacis surface is an excellent marker for selecting a reference level to calculate erosion rates. This glacis is a geomorphologic surface present at many points of the Guadix–Baza basin (Azañón et al., 2006; García-Tortosa et al., 2008) and it developed prior to the present-day drainage network entrenchment. Therefore, it provides the best approach for estimating the age of the endorheic–exorheic transition. Nevertheless, there are two ages proposed for this surface, one set forth by Azañón et al. (2006) and the other by Díaz-Hernández and Juliá (2006).

Díaz-Hernández and Juliá (2006) published a study on the geochronological position of badlands and the geomorphologic patterns in the Guadix–Baza basin. In order to establish the geochronological evolutionary framework of the main erosional stages in this depression, these authors dated three partially overlapping travertine platforms and a petrocalcic horizon capping the uppermost geomorphologic unit (named S1 in their work) using the U-series disequilibrium method. Two samples from the pisolitic horizon and a further two from the laminated layer have been dated and used to infer an age using an isochron approach to correct for the occurrence of a detrital phase. The authors report that equilibrium conditions result from the isochron approach applied to the four subsamples, indicating that the caliche formed not before 350 ka. As far as the choice of the pisolitic facies to infer the age of the caliche is concerned, it is noteworthy that this horizon, like others in the calcrete profile, is affected by the presence of older floating detrital grains that invalidate the age results by providing false older dates. A better approach would be to restrict selection of the caliche horizons to the massive laminated facies with the highest calcium carbonate contents (Azañón et al., 2006).

With regard to travertine data, only samples with high $^{230}Th/^{232}Th$ activity ratios have been considered significant and discussed by Díaz-Hernández and Juliá (2006). This approach is correct, but the ages obtained for the samples labeled "Upper travertine platform-1, -2, -3, -4" (characterised by a $^{230}Th/^{232}Th$ activity ratio equal to infinite) are not in suitable stratigraphical order (see Fig. 4 in Díaz-Hernández and Juliá, 2006). According to these authors, the upper platform is structured in three compact strata with massive stratified facies. Sub-samples 1, 2, and 3 come from the lower stratum and have been given ages covering a very large period from 205 ± 15 ka to 132 ± 6 ka; sub-sample 4 collected from the intermediate stratum of the upper platform was given an age of 174 ± 9 ka, more than 40 ka older than the youngest sample from the underlying stratum. This raises the suspicion that these chronological data are not reliable. Finally, three other data are considered significant by the authors because they are not affected by detrital contamination: one sample from the middle travertine platform (dated at 32 ± 0.7 ka) and two from the lower (36 ± 0.9 and 46 ± 2 ka). These data are grouped in a very short time interval, indicating a younger age of deposition for these travertine bodies.

The data proposed by Azañón et al. (2006) for the upper calcrete, together with the age of the lower calcrete dated in this work, agree with the age of 100 ka (Botella et al., 1985) proposed for the palaeontological site of Solana del Zamborino. This palaeontological site is one of the richest and best preserved of the Guadix–Baza basin (Botella et al., 1985; Ruiz-Bustos, 2002) and it is stratigraphically located a few meters below the glacis

surface. Therefore, we have considered the age of 43 ka as the most precise age for the capture of the Guadix–Baza basin by the Guadalquivir river system.

6.2. Erosion rates of the Guadix–Baza basin

In semi-arid environments with low but intense annual precipitation, erosion processes are mainly responsible for landscape configuration. These erosion processes are more significant when the dominant lithologies are poorly consolidated sediments and, therefore, easily erodible. In the Guadix–Baza basin, these conditions are present: a climate with low annual average precipitation occurring as scarce heavy rains and poorly consolidated Neogene sediments. It is clear that under these conditions erosion processes would be outstanding. Vandekerckhove et al. (2001) calculated short-term bank gully retreat rates in this basin, yielding very high values ranging between 4 and 6 m^3 yr^{-1}. Although these present-day values are very local, highly dependent on the area, and not comparable to the long-term erosion rates presented in this work, they do give an idea of the relevance of the erosion processes in semi-arid environments with highly erodible lithologies.

Another interesting comparison can be made with areas with similar morphological and lithologic configurations (i.e. areas with badlands and intensive erosion processes). Della Seta et al. (2006) presented erosion rates in areas with badlands in Central Italy by means of the Tu index (Ciccacci et al., 1981, 1986), deriving values in the range of 2 and 25 t ha^{-1} yr^{-1}. Although application of the Tu index can present variations depending on the basin area, it can be considered a proxy for long-term erosion rates.

Due to the difficulty of reconstructing the landscape prior to erosion, for long time intervals it is more common to present localized river incision rates. If we assume 200 m as the average maximum incision in the Guadix basin, where the basin capture occurred, we will obtain incision rates on the order of 4.7 mm yr^{-1}. In areas with very high convergence rates, incision rates can easily exceed 5 mm yr-1 (Burbank et al., 1996; Dadson et al., 2003). Present-day convergence rates in the Betic Cordillera are low (4-5 mm yr^{-1}, de Mets et al., 1994), thus discarding tectonics as the main reason for the high incision rates calculated here. Burbank et al. (1996) calculated river incision rates for the Indus river in the northwestern Himalayas obtaining values of 2–12 mm yr^{-1}, which were interpreted as related to tectonic rock uplift. This author proposed that in this case the erosion rates and the uplift rates were in equilibrium. Dadson et al. (2003) calculated erosion rates within the Taiwan orogen and founded that the highest erosion rates correspond to active structures developed on poorly consolidated sediments. Therefore, the lithology of river-bed basement can play a very important role when analyzing river incision rates, being responsible for important differences that can even occur under the same tectonic conditions.

River incision rates have been used in many studies to infer rock uplift rates (Burbank et al., 1996; Small and Anderson, 1998; Reinhardt et al., 2007a, b; Schlildgen et al., 2007). In the Betic Cordillera, there are values of long-term regional uplift rates calculated on the basis of present-day altitudes of preserved marine deposits. These uplift rates vary between 0.02 and 0.3 mm yr^{-1} (Braga et al., 2003; Sanz de Galdeano and Alfaro, 2004), i.e. they are one order of magnitude lower than the incision rates calculated in this work. There is a clear decoupling between river incision rates in the Guadix–Baza basin and long-term regional uplift rates. This decoupling seems to occur in other parts of the Betic Cordillera, such as the western border of the Sierra Nevada. In this area, Reinhardt et al. (2007b) have calculated river incision rates in the Torrente catchment, obtaining maximum rates of 5 mm yr^{-1} for the last 12 ka and 8 mm yr^{-1} for the last 1 ka. These authors envisage a rapid local base level fall as the cause behind these high incision rates.

In this regard the topographic position of the basin (1,000 m above sea level) with respect to its base level (at sea level) played a crucial role in its Quaternary evolution. When the capture of the Guadix–Baza basin occurred, the base level for erosion underwent a great fall, with an immediate lowering of ca. 1,000 m. The drainage network of the basin adjusted to these new conditions by eroding the poorly consolidated Neogene sediments of the basin. The river's response to such rapid changes is exponential, with a rapid adjustment just after the capture event, then decreasing in intensity over time. The dominant poorly consolidated lithologies in the basin would have increased this river erosion response. Since the capture of the basin is relatively recent, what we observe in the Guadix–Baza basin may be the effect of this first "rapid" adjustment to the capture. Once the Guadix-Baza basin was captured by the Guadalquivir river, the incision wave propagated headward very rapidly and the river-valley hillslopes adjusted to river downcutting by means of landsliding (Azañón et al., 2005). Mass transfer through landsliding is the most efficient process for hillslope adjustment to rapid river incision (e.g., Burbank et al., 1996). This is visible in many river canyons of the Guadix–Baza basin as is in the Arroyo the Gor, where large rotational landslides are very frequent (Azañón et al., 2005). Nevertheless, the high average elevation of this basin is probably related to large-scale long-term isostatic uplift after the pre-Miocene crustal thickening in the Betic Cordillera. Interestingly, the only sectors of the Betic Cordillera with a present-day crustal thickness exceeding 35 km are the Guadix–Baza basin and the Sierra Nevada (Banda et al., 1993). Therefore, we believe that sustained isostatic uplift may be taken to be responsible for maintaining the high average elevation of the Guadix–Baza basin.

6.3. Differential erosion rates for the Guadix and Baza sub-basins

One of the most interesting aspects of this work is the large differences (ca. one order of magnitude) between the erosion rates in the Guadix and Baza sub-basins (Table 1). First of all, we must take into account that the location of the capture point plays a crucial role in these differences. The Guadix sub-basin is located near this capture point and, as a consequence, most of the Pleistocene erosion is concentrated in this sub-basin. Also noteworthy is that the lower area of the Guadix sub-basin contributes to increasing the differences in the erosion rates with respect to the Baza sub-basin. Nevertheless, in addition to estimating the erosion rates, this work also examines how this erosion has evolved since the capture event. In Fig. 9, it is important to note how erosion advanced from the capture point southwards, reaching the foothills of the Sierra Nevada and Sierra de los Filabres. However, the erosion propagation-wave eastwards stops when it reaches the Baza fault (Fig. 9). This active normal fault uplifts the footwall where the Guadix basin is located (Alfaro et al., 2007, García-Tortosa et al., 2008) and, hence, provides an additional explanation for the differences in the erosion rates between the two sub-basins. This differential erosion is also visible on a smaller scale in ephemeral streams crossing the fault, whose erosion is restricted only to the footwall (Fig. 10). This fact reinforces the notion of the activity of this fault in the Quaternary, since it has affected the relief evolution of the Guadix–Baza basin.

Alfaro et al. (2007) have estimated the slip-rate of this fault at 0.25 mm yr^{-1}. They assume a constant rate since the late Tortonian for the fault and calculate its throw, between -1000 and -2000 m below sea level, with gravity and seismic profiles. The slip-rates proposed by these authors are valid as long-term rates for the Baza fault, but they are not accurate enough, and cannot be considered appropriate for the Quaternary activity of the Baza fault.

With the radiometric ages of the calcrete that forms the glacis surface, we can obtain an accurate late-Pleistocene slip-rate for the Baza fault. The glacis surface has an average offset of 100 m (Fig. 10.) and an age in the range of 43–60 ka; considering an average dip of 60º for the fault provides a Quaternary slip rate of 1.92 to 2.68 mm yr^{-1}. These rates are about one order of magnitude greater than those estimated by Alfaro et al. (2007), but they can be considered to be more valid for the Quaternary activity of this fault. Recent studies in other sectors of the Betic Cordillera have also obtained very high slip rates for some of the active normal faults. Reinhardt et al. (2007b) proposed a slip rate of 2 mm yr^{-1} (50 m of level fall in the last 21 ka) for the normal faults of the western mountain front of the Sierra Nevada. Giménez et al. (2000) made a study of vertical present-day uplift rates by comparing accurate leveling profile-data from the National Geographic Institute of Spain

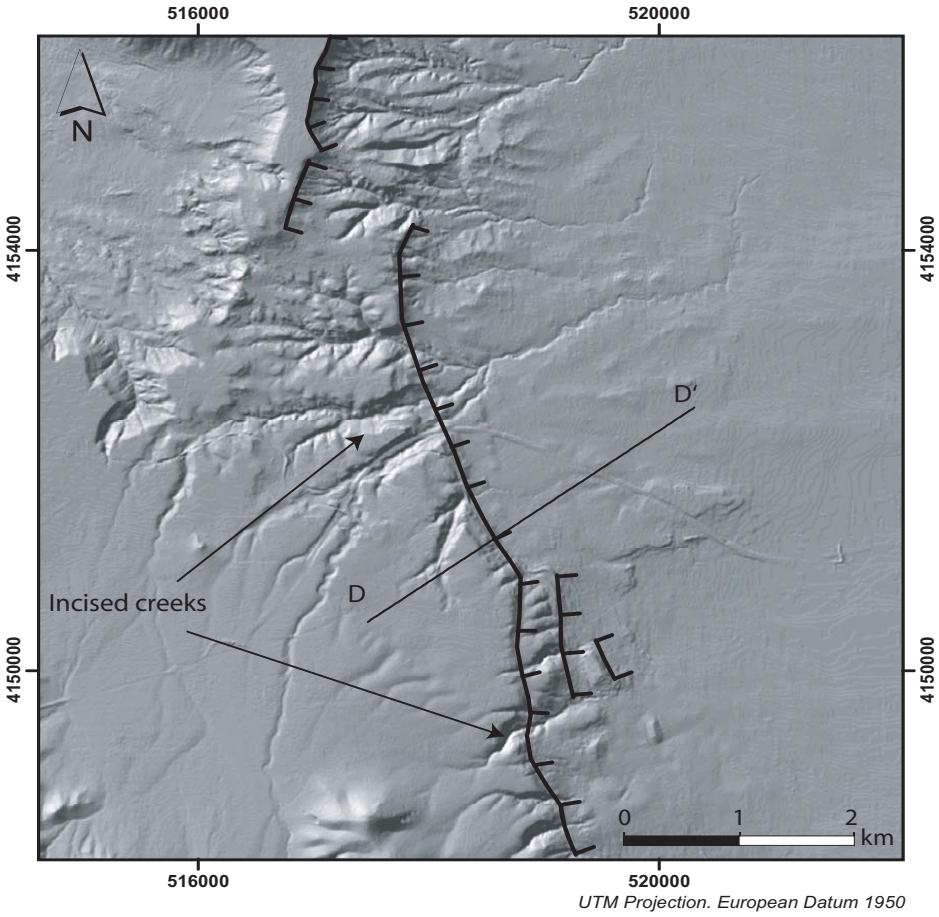

Figure 10. Detailed DEM of the Baza Fault (see location in Fig. 9). The differential erosion on both sides of the fault is noteworthy. The D–D' profile shows a very well-preserved scarp in soft materials, pointing to very recent activity for this normal fault.

(Instituto Geográfico Nacional). They obtained rates of 1 mm yr^{-1} approximately 30 km west of the Baza fault but still in its footwall (see Fig. 12 in Giménez et al., 2000). All the above-mentioned rates have a similar order of magnitude to the slip rates given in this work for the Quaternary activity of the Baza fault.

Another geomorphic feature indicating recent activity of the Baza fault is the good preservation of its fault scarp (Fig. 10) despite its location in poorly consolidated sediments. This scarp is not the topographic expression of a single tectonic event but of a cumulative throw and, therefore, its age cannot be estimated by its degradation stage. Nevertheless, based on the rates proposed by Alfaro et al. (2007), the Baza fault scarp should be 400,000 years old (García-Tortosa et al., 2008). However, the present-day conservation of the scarp, taking into account the intense erosional processes in the basin for the Quaternary and the poorly consolidated sediments, does not fit with such an older age, but with an age on the order of that presented in this work. Moreover, in order to maintain this well-preserved morphology, the Baza fault must have a moderate slip-rate in the Quaternary.

7. CONCLUSIONS

In this work we have presented and developed a methodology for the estimation of long-term erosion rates in the Guadix–Baza Neogene basin. This methodology is based on the reconstruction of the relief prior to river entrenchment by using a flat elevated surface (glacis) as a reference level. We have obtained all the cells in the DEM that correspond with this reference surface in order to interpolate the original morphology of the basin before the endorheic–exorheic transition. We have used the age proposed by Azañón et al. (2006) for a laminar calcrete that forms the glacis as the age for the basin capture. In order to corroborate this age, we have also dated the glacis surface at two locations, obtaining ages in the range of the values proposed by these authors. With this method, we have obtained not only the erosion rates for the Guadix–Baza basin, but also a view of how the erosion has been distributed in the basin since its capture by the Guadalquivir river.

The high erosion rates in the Guadix–Baza basin are one order of magnitude higher than the regional uplift rates. This decoupling between the erosion and uplift rates can be deemed as the result of basically two factors; i) the drastic base level fall due to the capture of the basin by the Guadalquivir river, and ii) the poorly consolidated nature of the sediments in the basin. The elevated topography of the Guadix–Baza basin (around 1,000 m above sea level) with respect to the Guadalquivir base level (sea level) produces high rates of erosion and river incision. The high elevation of the Guadix–Baza basin is probably related to long-term isostatic uplift in the Betic Cordillera.

The differential erosion rates between the Guadix and Baza sub-basins are the consequence of three factors: the position of the capture point near the Guadix sub-basin, the greater area of the Baza sub-basin, and the Quaternary activity of the Baza fault, which affected the normal propagation of the erosion wave eastwards.

With the radiometric data presented in this work, we have estimated the Quaternary slip rate for the Baza fault at 1.92-2.67 mm yr^{-1}. These slip rates fit better with the topographic expression of the Baza fault scarp and the glacis age.

Acknowledgements: This study was supported by the grants CGL2004-03333/BTE and TOPO-IBERIA CONSOLIDER-INGENIO CSD2006-00041 of the Spanish Ministry of Education. We are indebted to Christine Laurin for revising the English.

6

Active tectonics in the Sierra Nevada (Betic Cordillera, SE Spain): Insights from geomorphic indexes and drainage pattern analysis

J. V. Pérez-Peña [(1)*], A. Azor [(1)] and J. M. Azañón [(1,2)]

(1) Departamento de Geodinámica, Universidad de Granada, Granada, Spain
(2) Instituto Andaluz de Ciencias de la Tierra (UGR-CSIC)
* Correspondence to: JV Pérez-Peña, Departamento de Geodinámica, Campus Fuentenueva s/n, Universidad de Granada, 18071 Granada, Spain. E-mail: vperez@ugr.es

ABSTRACT: The Sierra Nevada mountain range, located in the central part of the Betic Cordillera, includes the highest peaks on the Iberian Peninsula (e.g., Mulhacén, 3482 m). It developed since the late Miocene by the interference between two orthogonal sets of NNE-SSW and E-W open folds. We carried out a geomorphologic study with the aid of evaluating the recent tectonic activity in this mountain range. On this purpose, we have calculated several geomorphic indexes in the Sierra Nevada. Mountain front sinuosity (S_{mf}) varies from the southern and western mountain fronts (1.17-1.34) to the northern mountain front (2.10). Ratio of width of valley floor to valley height (V_f) shows the same variation pattern as the Smf, presenting the higher values in the northern mountain front. Hypsometric curves describe younger and more active basins along the southern border of the Sierra Nevada. These data suggest that active faulting is more important in the south and south-western borders of Sierra Nevada, as it is also evidenced by other geological features. The drainage network in the Sierra is tectonically controlled by booth NNE-SSW and W-E folds as is evidenced by basin asymmetries and river flow-directions. Nevertheless, river profiles indicate that maximum linear erosion is concentrated in the western border of the sierra, thus pointing to maximum uplift related with the NNE-SSW isostatic folds. All these indexes indicate that the recent tectonic activity in the Sierra is mainly controlled by the extensional tectonics in the west and contractional tectonic in the east, where the extensional system became inactive.

Keywords: Tectonic Geomorphology; Mountain fronts; Drainage pattern; Geomorphic indexes; Active folding and faulting; DEM

Article submitted to Geomorphology

1. INTRODUCTION

Active tectonics is one of the most fast-growing disciplines in Earth Sciences due to the recent development of new geochronological and geodetic tools, which permit to obtain accurate rates (uplift rates, incision rates, erosion rates, slip rates on faults, etc.) at variable (10-10^6 years) time-scales (e.g., Schumm et al., 2000; Burbank and Anderson, 2001; Keller and Pinter, 2002). Furthermore, this discipline is becoming quite popular since the results of regional studies on active tectonics are of capital importance for evaluating natural hazards, as well as for planning land use and management in populated areas (e.g., Cloetingh and Cornu, 2005). Apart from its social and economic interest, studies on active tectonics must follow a multi-disciplinary approach, integrating data from structural geology, geomorphology, stratigraphy, geochronology, seismology, and geodesy.

In mountain ranges, recent and active tectonics can be viewed as the main factor contributing to rock uplift, being their present-day topography the result of the competition between tectonic and erosional processes (e.g., England and Molnar, 1990; Bishop, 2007). In the same way, topography, drainage pattern analysis, and geomorphic features can be used to evaluate recent and present-day tectonic activity (e.g., Keller et al., 2000; Azor et al., 2002; Molin et al., 2004; Harkins et al., 2005).

The drainage pattern in tectonically active regions is very sensitive to active processes such as folding and faulting. These processes can be responsible for accelerated river incision, asymmetries of the catchments, and river diversions, among other effects (e.g., Cox, 1994; Jackson and Leeder, 1994; Jackson et al., 1996, 1998; Clark et al., 2004; Salvany, 2004; Schoenbohm et al., 2004). River incision in such regions can be related to tectonic uplift, although other processes such as stream piracy, base level lowering, and climatic episodes can also be responsible for differential and accelerated river incision (e.g., Starkel, 2003; Hancock and Anderson, 2002; Azañón et al., 2005; Pérez-Peña et al., 2009b). Numerical dating of geomorphic surfaces and/or recent deposits is always necessary in order to obtain rates for the tectonic (folding, faulting, etc.) and geomorphic (river incision, etc.) processes (e.g., Hetzel et al., 2002; Watchman and Twidale, 2002).

This paper aims to evaluate the Quaternary tectonic activity in the Sierra Nevada mountain range (SE Spain) drawing on geomorphic indexes and drainage pattern analysis. The area of study is located in the central part of the Betic Cordillera, which represents, together with the Rif in Northern Morocco, the westernmost fragment of the Alpine circum-Mediterranean orogenic belt. According to the absolute and stratigraphic ages available, long-term Neogene-Quaternary tectonic activity seems to have occurred at low to moderate

rates (e.g., Johnson, 1997; Braga et al., 2003; Sanz de Galdeano and Alfaro, 2004) in this region dominated by normal faulting. The geomorphic data obtained suggest that activity in this mountain range is concentrated along the western mountain front, where normal fault scarps are well developed, although transverse active folding is also deduced and compatible with some of the tectonic models proposed recently.

2. GEOLOGICAL AND TECTONIC SETTINGS

The Betic-Rif arc-shaped mountain belt (Fig. 1) constitutes the western termination of the peri-Mediterranean Alpine orogen, being related at a broad scale to the collision between Africa and Iberia (de Mets et al., 1994; Morales et al., 1999; Galindo-Zaldívar et al., 1999; 2003). Despite the general N-S compressional setting, the kinematic picture of this orogenic belt is rather complicated because of the presence of a micro-plate (Alborán Domain), which seems to have displaced westward, colliding in Early Miocene times with the margins of southern Iberia and northern Africa (Balanyá and García-Dueñas, 1988). Thus, the Betic-Rif cordillera is made up of two external zones (the South Iberian margin in Spain and the Maghrebian margin in northern Morocco) with one internal zone in-between (the Alborán domain). The early compressional tectono-metamorphic evolution of the Alborán Domain is obscured by pervasive extensional tectonics occurred since Early-Middle Miocene times (e.g. Galindo-Zaldívar et al., 1989; Platt and Vissers, 1989; García-Dueñas et al., 1992; Lonergan and Platt, 1995; Martínez-Martínez et al., 1997; Orozco et al., 2004). This extensional tectonics is responsible for ductile shear zones, low- and high-angle normal faults, as well as for the initial development of Neogene-Quaternary sedimentary basins. The largest of these sedimentary basins is the Alborán Sea (Watts et al., 1993; Comas et al., 1999), which was formed over the metamorphic rocks of the internal zone, separating the Rif in Northern Morocco from the Betics in Southern Spain (Fig. 1). The extensional tectonics seems to have occurred coevally with N-S oriented compressional structures active since the Late Miocene too and responsible for large-scale E-W oriented folds (Martínez-Martínez and Soto, 2002). These folds depict the most outstanding topographic features in the internal zone of the Betic Cordillera: the antiforms coincide with the main ranges, which thus can be said to be antiformal ridges; the synforms coincide with Neogene-Quaternary sedimentary basins (Fig. 1).

The Sierra Nevada mountain range (Fig. 2) has been considered as an orogenic dome or core-complex structure, having been exhumed since the Late Miocene in an extensional tectonic regime involving in a first stage both low-angle normal faulting and vertical ductile thinning (Martínez-Martínez et al., 2004). The Pliocene-Quaternary tectonic evolution is responsible for the formation of a large-scale open antiformal ridge coincident with the whole extent of the Sierra Nevada and coeval normal faulting (Fig. 2). Galindo-

Zaldívar et al. (2003) considered the antiformal ridge related to a blind-thrust buried under the northern E-W oriented mountain front of the Sierra Nevada, while the normal faults would be coeval and related to extension sub-perpendicular to the NNW-SSE axis of maximum shortening (Africa-Iberia present-day vector of convergence). Martínez-Martínez et al. (2004) proposed that the present-day topography of the Sierra Nevada is due to the interference of two orthogonal sets of Miocene-Pliocene, large-scale open folds trending roughly E-W and NNE-SSW. They suggested that NNE-SSW folds were generated by a rolling-hinge mechanism, whilst E-W folds are due to shortening perpendicular to the direction of extension.

The western border of the Sierra Nevada is bounded by NW-SE striking normal, which limit the sediments of the Neogene Granada and Padul basins. These faults present clear activity in Quaternary-Holocene times as can be deducted from seismicity and deformed Holocene alluvial fans (e.g. Alfaro et al., 2001). Some authors have proposed slip rates of 0.6 - 0.8 mm/yr for these faults in the Quaternary (Sanz de Galdeano, 1996; Keller et al., 1996). El Hamdouni et al. (2007) studied some geomorphic indexes in this part of the Sierra Nevada, proposing a moderate-high tectonic activity for these faults in the Quaternary. Reinhardt et al. (2008b) studied the response to a rapid base-level fall in the Torrente river, which is limited in its mouth by these faults. These authors dated Quaternary sediments using radiometric methods and proposed that 50 m of base-level fall should be occurred in the last 21 ka.

The northern and southern borders of the Sierra Nevada present very different characteristics. The southern border is bounded by a WSW–ENE sub-vertical dextral strike-slip fault zone, which has been active Miocene (Sanz de Galdeano et al., 1985; Martínez-Martínez et al., 2006). On the contrary the northern border of the Sierra Nevada is not fault-bounded and the Neogene-Quaternary sediments of the Guadix-Baza basin unconformably overlaying the metamorphic rocks of the Sierra Nevada (Fig. 2).

The present-day seismicity in the Sierra Nevada and surrounding areas fits well with the tectonic structures described before; the earthquake epicentres are concentrated along the western and southern borders, the core of the range being aseismic (Martínez-Martínez et al., 2006). The Neogene-Quaternary Granada basin located to the west (Figs. 1, 2) presents the highest seismic activity in all of the Iberian Peninsula, with a great number of earthquakes of low to moderate magnitude ($mb \leq 5.5$) (Morales et al., 1997). Focal mechanisms indicate a present-day stress-state dominated by radial extension or by a NE-SW oriented extensional axis (Galindo-Zaldívar et al., 1999; Muñoz et al., 2002).

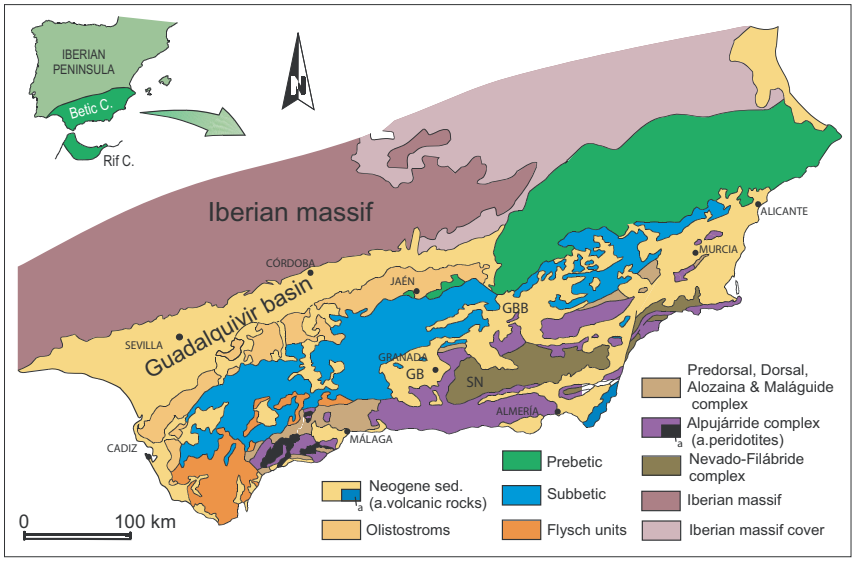

Figure 1. Geological sketch of the Betic Cordillera (modified from Ruano et al., 2003). GB, Granada Basin; GBB, Guadix-Baza Basin; SN, Sierra Nevada.

3. DRAINAGE PATTERN ANALYSIS

Uplift of the Sierra Nevada started in Early Tortonian times (Johnson, 1997; Braga et al., 2003), but its present-day drainage pattern started to develop in the Pleistocene, i.e. streams draining the Sierra Nevada incise into Pleistocene deposits of the Neogene basins surrounding the range. Nevertheless, some palaeorivers coincide with nowadays rivers, as deduced from the distribution of Pliocene to lower Pleistocene fan deposits in the Granada basin (Alhambra Formation and Zubia Formation) and the Alpujarra Corridor (Quaternary deposits in the Ugíjar basin).

The drainage network has been extracted from a Digital Elevation Model (DEM) of 10 m of pixel resolution following the methodology described by Tarboton (1997). This methodology takes into account the accumulation of upwards curved grid cells (Peuker and Douglas, 1975; Band, 1986), being adaptive to spatial variability in drainage density. This drainage network was cleaned and validated in order to avoid DEM-associated errors, and channels were ordered following Strahler (1952).

We have divided the Sierra Nevada in three sectors (Fig. 4) (west, middle, and east), attending to the main drainage systems. The western sector comprises the Genil and Gua-

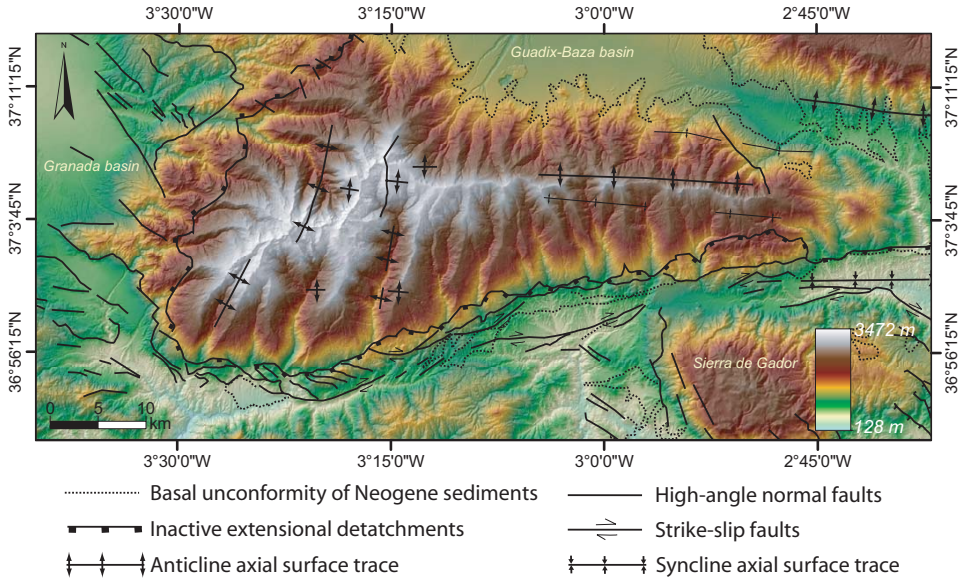

Figure 2. Digital elevation model (DEM) with the Sierra Nevada mountain range and the main tectonic structures (tectonic structures are taken from Martínez-Martínez et al., 2006).

dalfeo main rivers with their corresponding tributaries. The Guadalfeo drains to the Mediterranean Sea, whereas the Genil river is a tributary of the Guadalquivir river, which, in turns, drains to the Atlantic Ocean. The middle sector contains the Adra drainage system in the southern slope of the Sierra Nevada, which drains towards the Mediterranean Sea, and some tributaries of the Guadiana Menor river in the northern slope, which drains to the Atlantic Ocean. The eastern sector includes the Andarax drainage system, which drains towards the Mediterranean Sea.

The main divide in the Sierra Nevada is mostly straight or gently curved (Fig. 3) and lacks along-strike important steps, with the highest elevations located in its western part (Fig. 3). Some bends of the crest-line are clearly related to head-ward erosion of the streams draining the southern limb of the Sierra Nevada, which thus tend to capture the highest sectors of the catchments draining the northern limb (Fig. 3). The streams draining the northern limb are generally longer than the ones draining the southern limb, due to the higher local-base level in the northern limb. The orientations of the main streams are generally perpendicular to the crest-line in the middle sector of the range and present a radial pattern in the western termination. The drainage pattern in the easternmost sector of the Sierra Nevada presents some peculiar anomalies. There are some channels that flows almost parallel to the river divide coinciding with the traces of W-E minor folds.

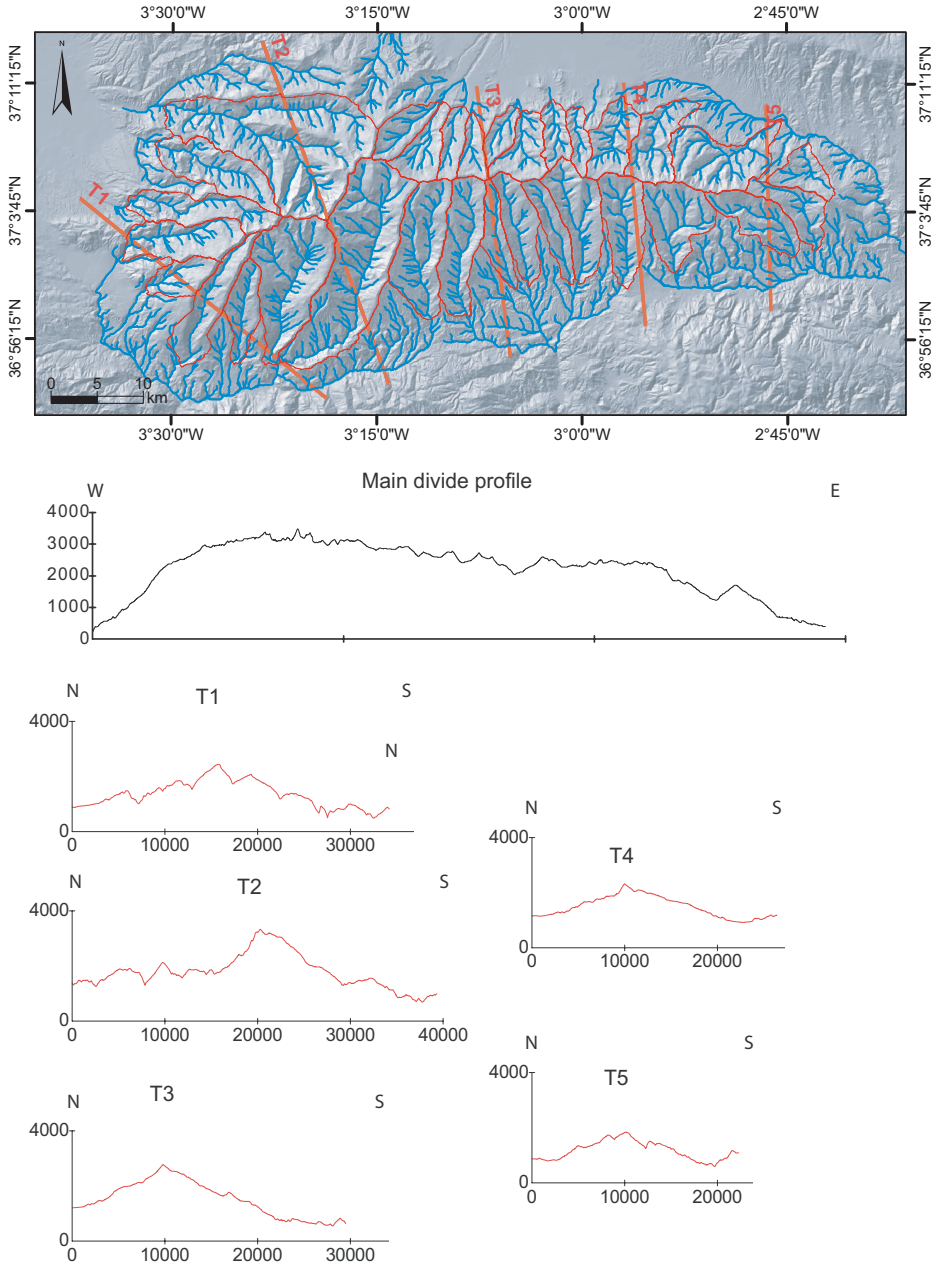

Figure 3. Shaded relief map with the drainage network extracted for the Sierra Nevada. Five transversal profiles and one longitudinal profile (following the main divide between the north and south slopes) are presented. The profiles were made using a DEM of 10 m resolution provided from the Junta de Andalucía regional government.

4. GEOMORPHIC INDEXES

We have analyzed several geomorphic indexes [mountain-front sinuosity (S_{mf}), valley floor width-to-height ratio (V_f), and asymmetry factor (AF)], together with topographic river profiles and hypsometric curves for the main catchments of the Sierra Nevada.

4.1. Mountain front sinuosity (S_{mf})

Mountain-front sinuosity was defined by Bull (1977) as:

$$S_{mf} = L_{mf} / L_s$$

Where S_{mf} is the mountain front sinuosity; L_{mf} is the length of the mountain front along the foot of the mountain, i.e. the topographic break in the slope, and L_s is the length of the mountain front measured along a straight line. This index has been used to evaluate the relative tectonic activity along mountain fronts (Bull and McFadden, 1977; Keller and Pinter, 2002; Silva el al., 2003). In active mountain fronts, uplift will prevail over erosional processes, yielding straight fronts with low values of S_{mf}. On the contrary, in less active fronts the erosional processes will generate irregular or sinuous fronts, with high values of S_{mf}. Some studies have proposed that values of the S_{mf} index lower than 1.4 are indicative of tectonically active fronts, while values higher than 3 are related to inactive fronts (Keller, 1986; Silva et al., 2003).

This index has been applied to some of the fault-bounded mountain fronts of the western Sierra Nevada (El Hamdouni et al., 2006; Martín-Rojas et al., 2003). In this work we have differentiated three main mountain fronts: northern, southern, and western fronts (Fig. 4), which correspond to different tectonic situations as previously explained.

The S_{mf} index is low in the western (S_{mf} = 1.17) and southern (S_{mf} = 1.34) mountain fronts (Fig. 4), suggesting that these two fronts are tectonically active. On the contrary, the value obtained for the northern mountain front (S_{mf} = 2.10) is much higher, pointing out to an inactive front.

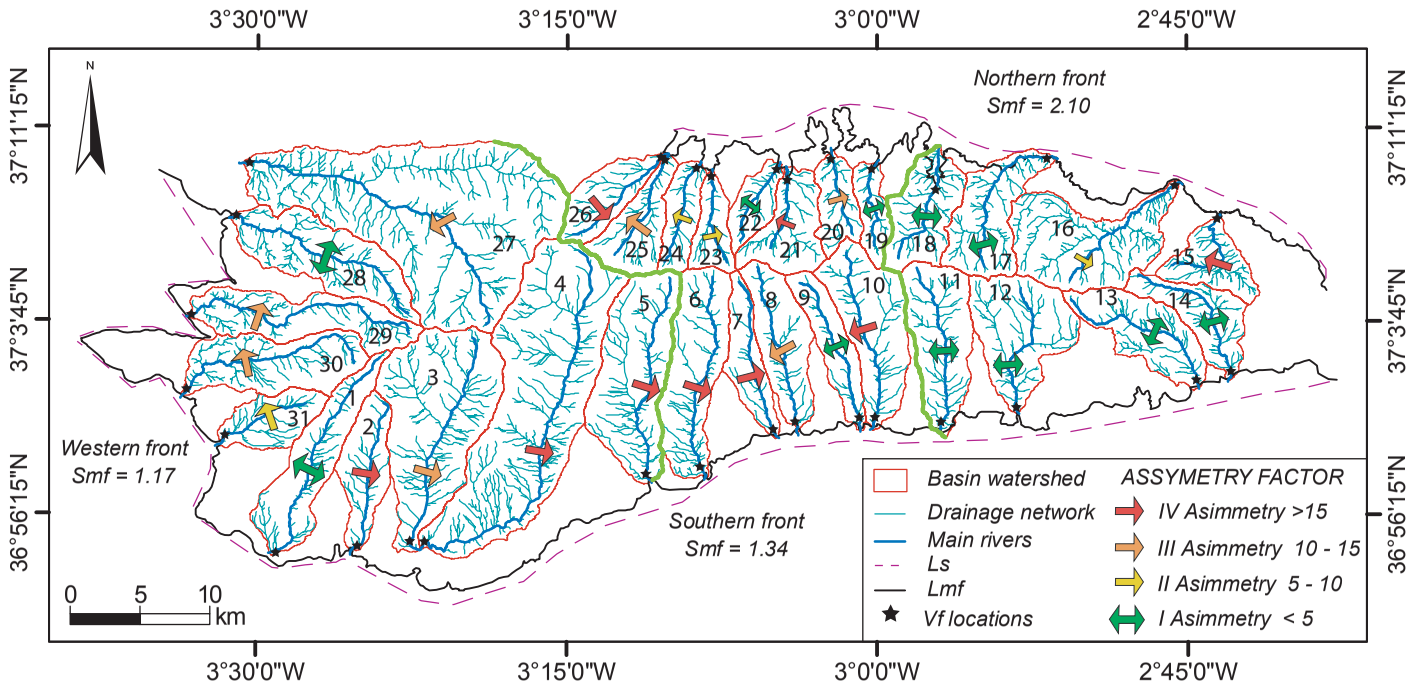

Figure 4. Schematic map showing the main geomorphic indexes calculated in this work. AF values are represented with an arrow indicating the asymmetry sense, and a colour indicating the class (see text for further explanation). Black starts show the locations of the V_f measurements (300 metres from the mountain front). Bolder light-green lines differentiate the Sierra Nevada sectors defined in the work (west, central, and east). Values of S_{mf} for each mountain front are indicated. Basins are labeled with a number (see table 1 for river names).

ID River	*Name*	V_{fw}	E_{ld}	E_{rd}	E_{sc}	V_f	*AF*
1	Lanjarón R.	44	1157	710	539	0.112	3.872
2	Chico R. (W)	71	800	653	553	0.409	16.665
3	Poqueira R.	19	937	864	604	0.064	13.701
4	Trevelez R.	15	1195	807	633	0.041	22.110
5	Cadiar R.	78	1284	1261	1012	0.299	23.851
6	Mecina R.	18	1271	1053	862	0.060	20.716
7	Valor R.	55	877	865	780	0.604	21.697
8	Nechite R.	40	1028	980	803	0.199	11.566
9	Laroles R.	74	1006	828	731	0.398	2.850
10	Picena R.	66	884	935	706	0.324	15.189
11	Alcolea R.	98	1114	1052	797	0.343	3.350
12	Andarax R.	54	1316	1333	959	0.148	3.777
13	Chico R. (E)	30	894	945	660	0.116	4.927
14	Rmb. de Tices	73	834	822	635	0.378	2.083
15	Rmb. de Santillana	78	948	996	778	0.402	18.100
16	Abrucena R.	175	919	1054	834	1.148	8.854
17	Nacimiento R.	92	1101	1217	1008	0.609	0.408
18	Hueneja R.	144	1366	1405	1194	0.752	2.982
19	Rmb. De los Castaños	61	1540	1486	1313	0.305	1.140
20	Chico creek	108	1392	1360	1273	1.049	14.399
21	Rmb. de Benejar	45	1464	1364	1279	0.333	21.957
22	Bco. del Gallego	91	1378	1395	1272	0.795	0.847
23	Bco. del Barrio	52	1447	1485	1373	0.559	9.828
24	Bco. del Pueblo	37	1522	1500	1344	0.222	6.449
25	Bco. de Alcazar	33	1546	1381	1294	0.195	10.975
26	Bco. de Alhorí	20	1395	1417	1330	0.263	24.541
27	Genil R.	185	970	933	766	0.997	10.040
28	Monachil R.	23	1098	1206	948	0.113	3.599
29	Dilar R.	26	1223	1237	957	0.095	11.816
30	Durcal R.	28	1132	1103	809	0.091	11.049
31	Torrente R.	19	1373	1277	974	0.054	8.327

Table 1. Values of V_f (and related parameters) and AF for the main rivers of the Sierra Nevada.

4.2. Valley floor width-to-height ratio (V_f)

Valley floor width-to-height ratio (V_f) (Bull and McFadden, 1977) is a geomorphic index conceived to discriminate between V-shaped and U-shaped flat-floored valleys. This index is defined as:

$$V_f = (2V_{fw}) / [(E_{ld}-E_{sc}) + (E_{rd}-E_{sc})] \quad (2)$$

Where V_f is the valley floor width-to-height ratio, V_{fw} is the width of the valley floor, E_{ld} and E_{rd} are elevations of the left and right valley divides, and Esc is the elevation of the valley floor.

Deep V-shaped valleys (V_f<1) are associated with linear active downcutting streams distinctive of areas subjected to active uplift, while flat-floored valleys (V_f > 1) are characteristic of sectors with major lateral erosion in response to relatively tectonic quiescence (e.g. Keller and Pinter, 2002). This index has been applied to several mountain fronts located in the eastern and central Betic Cordillera (Silva et al., 2003; Pedrera et al., 2009).

The V_f index was calculated for all the main channels, 300 m upstream from the mountain front (Fig. 4). For narrow river-valleys (valley-width < 50 m) the used DEM is insufficient to accurately measure valley widths. For this reason, this parameter was obtained by measuring widths directly from aerial photographs. The obtained V_f values are higher in the northern mountain front, and lower in the western mountain front (Fig. 5).

4.3. Asymmetry factor (AF)

The asymmetry factor (AF) of catchments was used to detect possible tectonic tilting at the scale of the whole range. The AF is defined as (Hare and Gardner, 1985; Keller and Pinter, 2002):

$$AF = 100(A_r / A_t) \quad (3)$$

Where A_r is the area of the basin to the right (facing downstream) of the trunk stream, and A_t is the total area of the drainage basin. Values of AF above or below 50 indicate that the basin is asymmetric.

In order to avoid possible confusions between the catchments located in the northern and southern slopes of the Sierra Nevada, we expressed AF as the absolute value minus 50 and added an arrow indicating the asymmetry direction. We have divided AF absolute va-

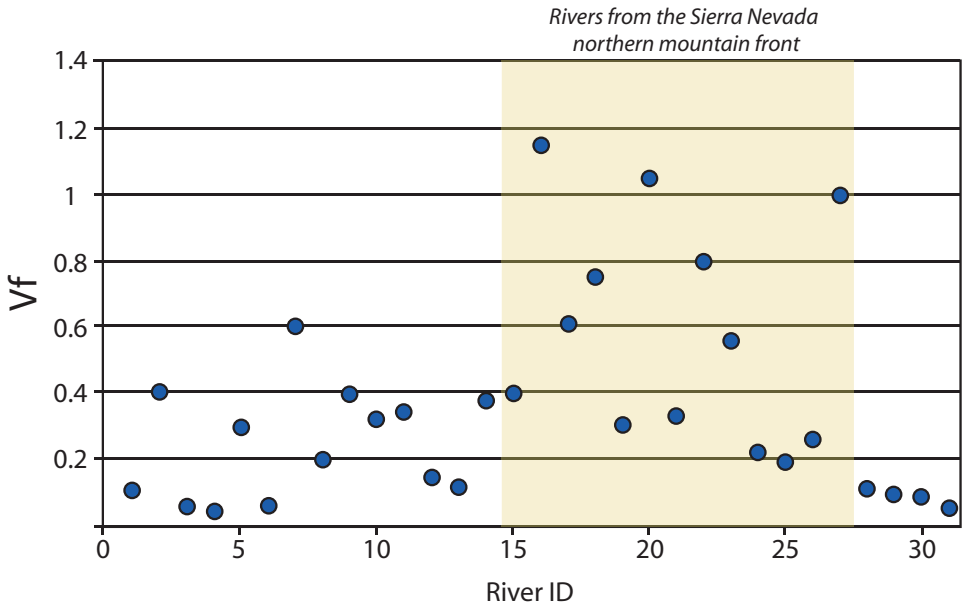

Figure 5. Plot of V_f values for the main rivers of the Sierra Nevada. Rivers are labeled with a number (see table 1 for river names). Rivers from the northern mountain front of the Sierra Nevada are highlighted.

lues in four classes; AF < 5 (symmetric basins), AF = 5-10 (gently asymmetric basins), AF = 10-15 (moderate asymmetric basins), and AF > 15 (strong asymmetric basins). AF values in the western part of the Sierra Nevada present a pattern with contrary asymmetries at both sides of the Lanjaron river, thus coinciding with the fold hinge of one of the NNE-SSW oriented antiforms (Table 1, Figs. 2, 4). In the eastern part of the Sierra there is not a defined pattern in AF values, and the majority of the basins are symmetric (AF < 5).

4.4. Hypsometric curves

The hypsometric curve of a catchment represents the distribution of area and altitudes within a basin (Strahler, 1952). This curve is created by plotting the proportion of total basin height (relative height) against the proportion of total basin area (relative area) (Strahler, 1952; Keller and Pinter, 2002). A useful attribute of these curves is that drainage basins of different sizes can be compared with each other since area and elevation are plotted as functions of total area and total elevations and therefore, the curves are independent of differences in basin size and relief (Keller and Pinter, 2002; Walcott and Summerfield, 2008; Pérez-Peña et al., 2009a). The shape of this curve is related to the degree of dissection of the basin, i.e. its erosional stage. Convex hypsometric curves characterize "young"

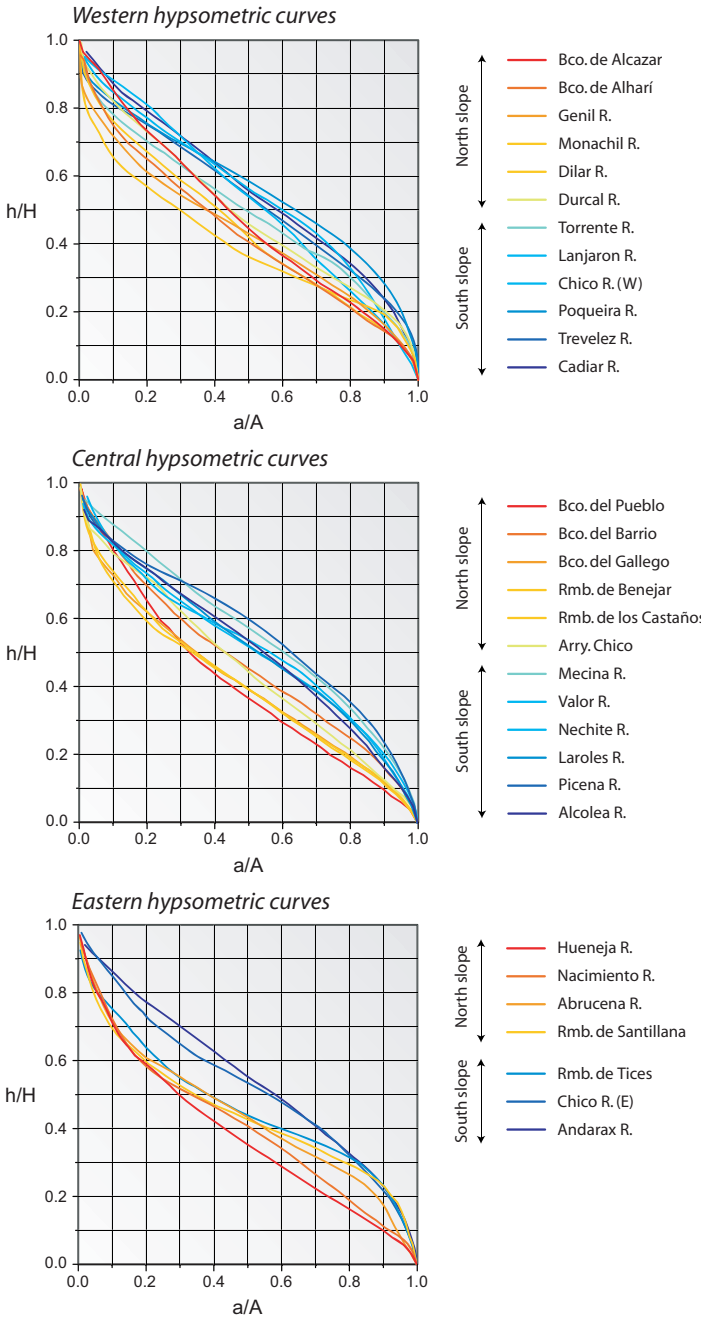

Figure 6. Hypsometric curves from the different sectors of the Sierra Nevada. Curves have been calculated using a DEM of 10 m resolution and CalHypso ArcGIS module (Pérez-Peña et al., 2009a). Curves from the northern slope of the Sierra Nevada are drawn with blue colours, while curves from the southern slope are in red colours.

weakly eroded regions; S-shaped curves characterize moderately eroded regions; concave curves characterize old highly eroded regions. The area below the hypsometric curve is known as the Hypsometric Integral (HI), varying from 0 to 1, with values close to 0 in highly eroded regions and values close to 1 in weakly eroded regions. The shape of the hypsometric curves –and the HI values- also provide valuable information on the tectonic, climatic and lithological factors controlling catchment landscape (e.g. Moglen and Bras, 1995; Willgoose and Hancock, 1998; Huang and Niemann, 2006).

We have calculated the hypsometric curves for all of the basins draining the Sierra Nevada with the aid of an ArcGIS extension (Pérez-Peña et al., 2009a). The hypsometric curves show differences between the curves of the north and south slopes of the Sierra. The curves from the north slope (northwards to the Lanjarón river) show profiles more concave than the ones from the south slope (Fig. 6). There is not a clear variation in the shape of the curves from east to west neither in the north nor the south slopes of the Sierra Nevada.

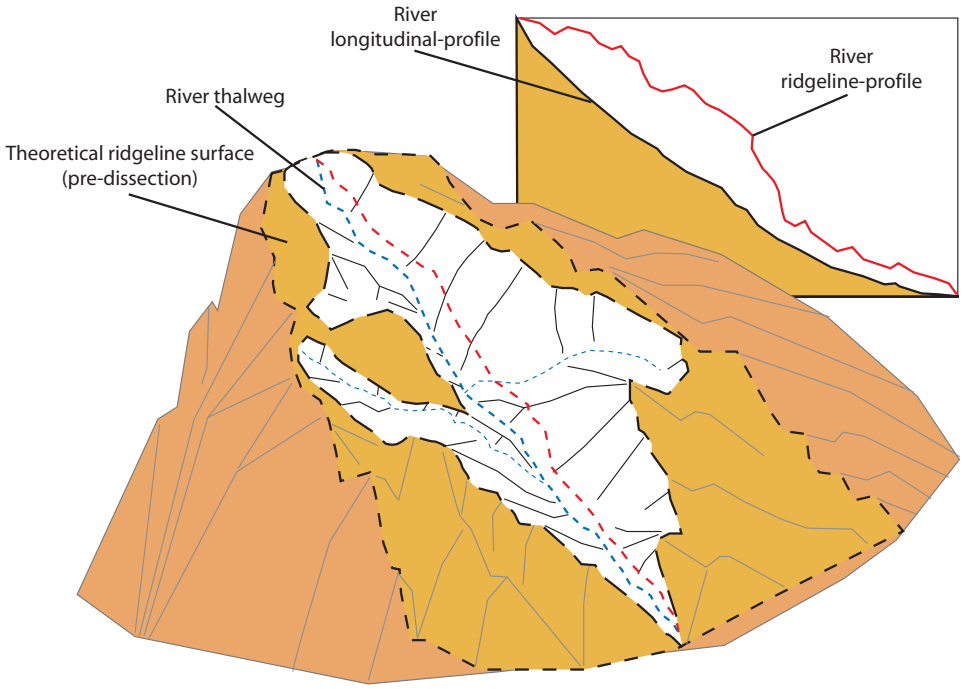

Figure 7. Schematic cartoon showing the methodology used to obtain the projected ridge-line profiles. (Modified from Menéndez et al., 2008)

4.5. Longitudinal river profiles

Longitudinal river profiles can be interpreted as resulting from the balance between erosion and uplift rates (Hovius, 2000; Menendez et al., 2007). Hovius (2000) defined three types of profile morphologies according to uplift rates and monthly rainfall (as a proxy of denudation rate). Concave profiles represent long-term equilibrium between uplift and erosion rates. Concave-convex profiles with erosion steps in the middle reaches indicate long-term predominance of erosional processes. Convex profiles are characteristic of areas where uplift is dominant.

Valuable information can also be obtained from "ridge-line profiles" (Menendez et al, 2008). These profiles are drawn by projecting river thalwegs onto a theoretical pre-incision layer constructed from present-day lateral divides of the basins (Menendez et al, 2008; Fig. 7). One advantage of these ridge-line profiles is that they provide equivalent lengths as for the longitudinal river. Despite of this type of pre-incision layer cannot be considered exactly the pre-incision surface (Brocklehurst and Whipple, 2002) it can generate a view of the structure of the relief for each basin, allowing relative comparisons of bulk erosion between the different basins.

Longitudinal and ridge-line river profiles have been extracted for the main river draining the Sierra Nevada (Fig. 8). The rivers of the northern slope of the Sierra present mainly concave profiles, while the rivers of the south slope depict linear and convex profiles (Fig. 8). In the western sector some river profiles show erosion steps as the Poqueira, Trevelez, and Cadiar river, and other present clear convex profiles (Lanjaron river) or slightly concave profiles (Durcal, Monachil, and Dilar rivers) (Fig. 8). Ridgeline profiles show the greatest height differences in the western sector of the Sierra (Fig. 8). On the contrary, the smallest height differences are found in rivers of the northern slope of the Sierra (Fig. 8).

5. DISCUSSION AND CONCLUSIONS

The geomorphic indexes calculated in this work suggest that the Sierra Nevada is tectonically active, with the more recent uplift concentrated along its western mountain front, where S_{mf} and V_f present the lowest values (Figs. 4, 5). This conclusion is corroborated by surface geology, since the western mountain front coincides with prominent normal fault scarps and has associated Quaternary alluvial fans. Furthermore, these faults affect the alluvial fans and present high Quaternary slip-rates (Sanz de Galdeano 1976; Calvache and Viseras, 1997; Sanz de Galdeano 1996; Keller et al., 1996). The distribution of present-day seismicity also points to active faulting along the western mountain front of the Sierra Nevada (Morales et al., 1997; Muñoz et al., 2002; Martínez-Martínez et al., 2006).

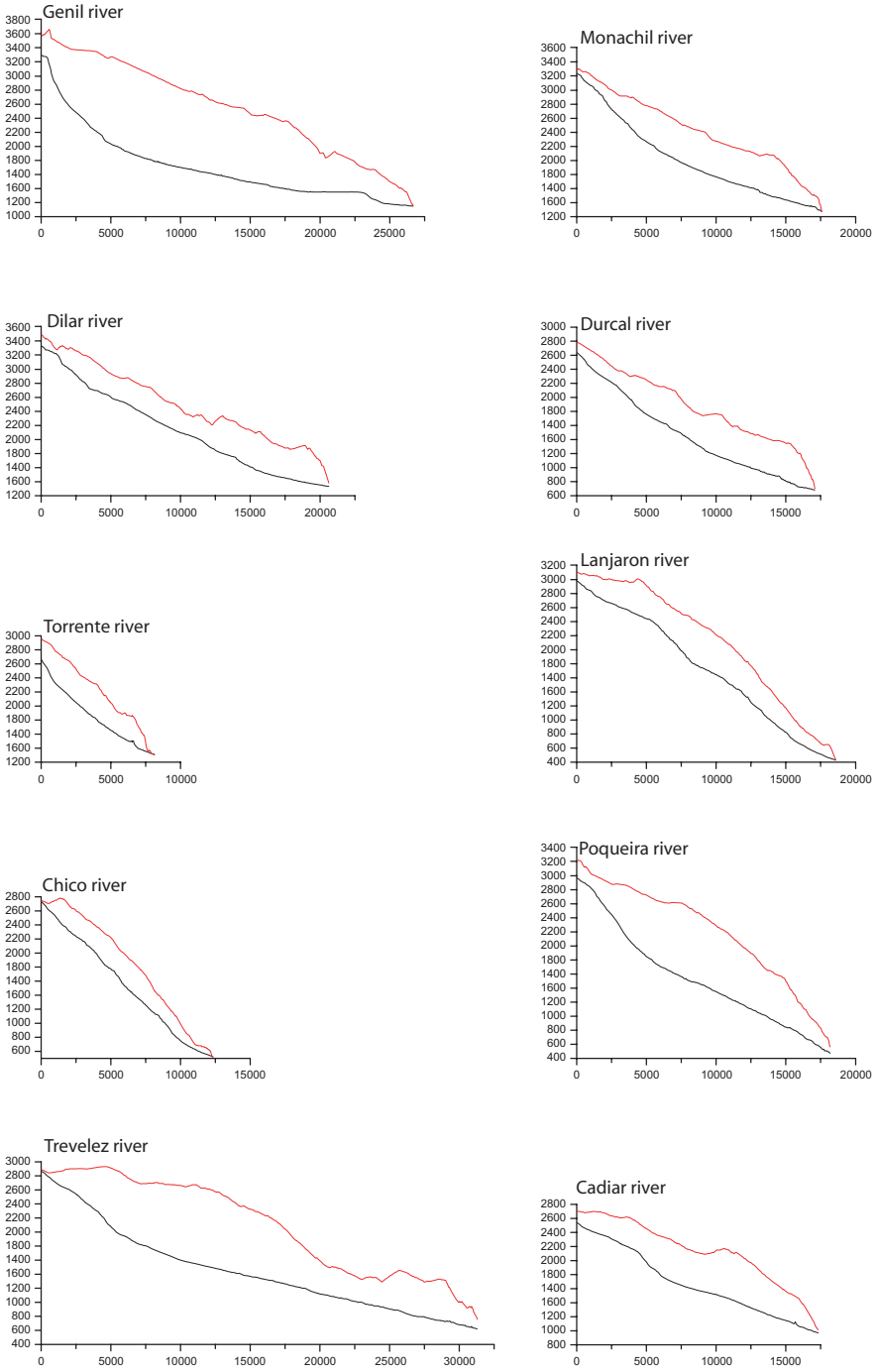

Figure 8. River longitudinal and ridge-line profiles for the main rivers of the Sierra Nevada.

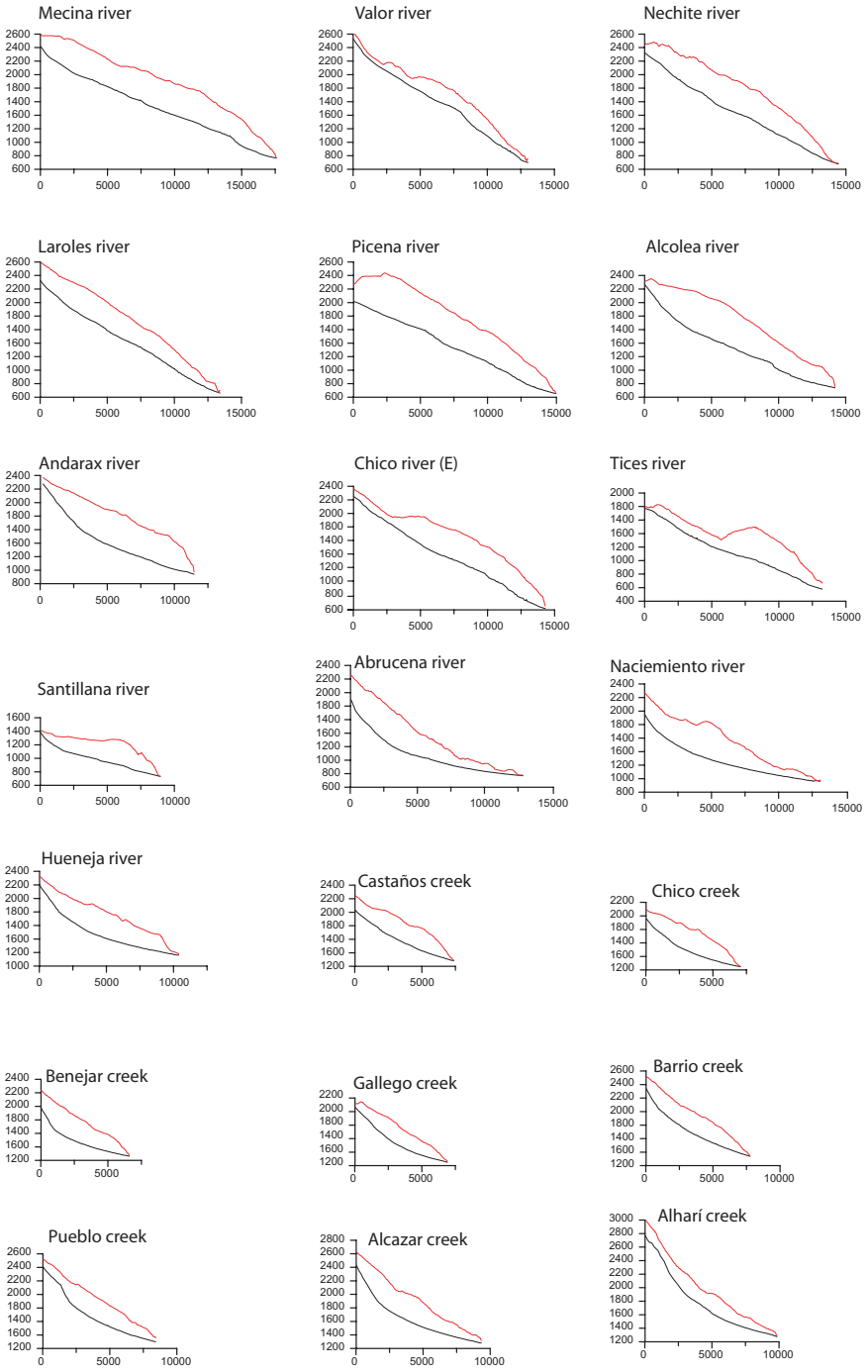

Figure 8. (Continuation)

The southern mountain front of the Sierra Nevada is characterized by low values of S_{mf} and V_f (Figs. 4, 5), though the interpretation in terms of tectonic activity is not so straightforward as in the case of the western mountain front. Actually, the southern mountain front runs parallel to one of the main rivers in the region, namely the Guadalfeo river, whose Quaternary incision and retreat might be responsible, at least partially, for the low values of S_{mf} and V_f. Moreover, fault scarps are not as prominent as in the western mountain front. However, the presence along some segments of this mountain front of subvertical strike-slip faults (Sanz de Galdeano and Rodríguez-Fernández, 1985) is indicative of recent tectonic activity. In this respect, Martínez-Martínez et al. (2006) proposed that the southern Sierra Nevada border is an active transfer fault made up of strike-slip fault segments, which join two normal fault-bounded mountain fronts (western Sierra de Gádor front and Sierra Nevada mountain fronts). Therefore, the southern Sierra Nevada mountain front can be considered to have Quaternary tectonic activity, though its geomorphic expression is a bit ambiguous due to the recent incision of the Guadalfeo river and the interference of relay-ramp and fault-bounded sectors along the mountain front.

The northern mountain front of the Sierra Nevada presents the hightest S_{mf} and V_f values, thus suggesting low rates of Quaternary tectonic activity. Accordingly, this mountain front corresponds to an unconformity between the Neogene-Quaternary sedimentary infill of the Guadix-Baza basin and the metamorphic rocks of the Sierra Nevada. Furthermore, no appreciable present-day seismicity is observed along this mountain front, which also reinforces the idea that it is tectonically inactive.

Other geomorphic indicators sensible to active tectonics, such as hypsometric curves, longitudinal/ridgeline river profiles, and drainage patterns, show subtle E-W and N-S variations, which are best understood in terms of river dynamics rather than in terms of differential tectonic uplift. N-S variations are mainly due to the fact that local base-level is ≈1100 m in the northern mountain front of the Sierra Nevada and ≈600 m in the southern one, i.e. southern slope streams have more erosional power than northern ones. Therefore, southern slope streams are longer and more entrenched than northern ones (Figs. 3, 4). No systematic E-W variation in the hypsometric curves/ if found in the Sierra Nevada (Fig. 6). On the contrary, river entrenchment as deduced from the comparison of longitudinal and ridgeline river profiles increases westward (Fig. 8). This fact might be related to the recent uplift of the western Sierra Nevada as compared to the eastern.

The main rivers of the western and central sectors of the Sierra Nevada show a radial pattern around the highest peaks (Figs. 3, 4). This simple pattern changed in the easternmost sector, where some streams are not perpendicular to the main E-W divide, but

rather oblique or even parallel to it (Rivers 13, 14, and 15; Figs. 3, 4). The main cause for the existence of these streams with "anomalous directions" is probably related to complex piracy processes occurred during the Pliocene and Quaternary evolution of the Andarax catchment. However, E-W oriented active folding might have also contributed to this complicated drainage pattern (Fig. 2).

The asymmetry factor of the main catchments draining the Sierra Nevada has also been calculated in order to detect active large-scale surface tilting. Most catchments show no asymmetry, except in the southwestern sector of the range where opposite and systematic asymmetries have been found at both sides of the Lanjarón river (Fig. 4). The absence in this sector of important faults striking NNE-SSW (parallel to the Lanjarón river) discards the interpretation of this asymmetry pattern as related to active faulting. Therefore, catchment asymmetry in the southwestern sector of the Sierra Nevada is probably due to active folding. In this view, an antiform striking parallel to the Lanjarón river (NNE-SSW) accords well with the basin asymmetry data obtained (Fig. 2).

Quaternary uplift rates in the Sierra Nevada are very scarce, lacking data enough as to propose systematic transverse (N-S) and along-strike (E-W) variations. In the eastern sector, García et al. (2003) obtained river incision rates between 0.3 and 0.8 mm/yr for the last 303-245 ka, which can be reasonably assumed to correspond to tectonic uplift. Actually, these uplift rates (0.3-0.8 mm/yr) are only slightly higher than long-term uplift rates calculated for the whole period (8-10 Ma) of relief formation in the Sierra Nevada (0.3-0.4 mm/yr; Sanz de Galdeano and López Garrido, 1999; Braga et al., 2003; Sanz de Galdeano and Alfaro, 2004). Therefore, the eastern sector of the Sierra Nevada seems to have not undergone any accelerated tectonic uplift in Quaternary times, as also deduced from the geomorphic approach followed in our work. In the western Sierra Nevada. Reinhardt et al. (2008b) have reported incision rates of 5 mm/yr, which they relate to a base-level fall of 50 m in the last 12 ka. The cause of such base-level fall cannot be but active faulting along the western mountain front of the Sierra Nevada, since sea-level falls are discarded for this period of time. Assuming these very high erosion rates to be due to tectonic uplift in the hanging wall of the normal faults bounding the western Sierra Nevada, the low values of S_{mf} and V_f obtained here are easily explained in terms of very high and recent faulting along this mountain front.

Looking for a tectonic model for the Quaternary tectonic evolution of the Sierra Nevada is not an easy task, since extension and compression seem to have acted coevally. Most authors propose a Quaternary stress field characterized by NW-SE compression with a concomitant extension axis oriented NE-SW (de Mets et al., 1994; Galindo-Záldivar et

al., 1999; 2003). Thus extensional and compressional structures with different orientations would have formed at the same time. In the case of the Sierra Nevada, the E-W oriented large-scale antiform coincident with the whole range is thought to be a result of the NNW-SSE compression occurred since the Pliocene, while the NW-SE oriented normal faults bounding the western mountain front are associated to SW-directed extensional tectonics (e.g. Galindo-Zaldívar et al., 2003; Martínez-Martínez et al., 2006). This scenario is roughly coherent with the main conclusions derived from our study, i.e. the highest tectonic activity in the Sierra Nevada is concentrated along its western mountain front and consists in normal faulting with donwthrowing of the SW block (Granada and Padul sedimentary basins) and uplift of the range. Nevertheless, the presence of NNE-SSW oriented active folding in the western termination of the Sierra Nevada as deduced from the study of catchment asymmetries, introduces some complexity to the tectonic scenario invoked. In this respect, the tectonic model proposed by Galindo-Zaldívar et al. (2003) considered the E-W oriented large-scale antiformal ridge to be active and related to a blind thrust buried under the northern mountain front of the Sierra Nevada. This model envisaged the northern mountain front as tectonically active, which is not the case according to geomorphic indexes calculated. At the same time, Galindo-Zaldívar et al. (2003) proposed that SW-directed extension is coeval with the NNW-SSE oriented compression, but their model does not explains the existence of NNE-SSW oriented active folding. These active folds might be completely different in origin to the E-W oriented ones as proposed by Martínez-Martínez et al. (2006). These authors considered the existence of a generation of NNE-SSW oriented folds with an isostatic origin related to the unroofing produced by the normal faults of the western Sierra Nevada mountain front.

To sum up, our geomorphic study points to Quaternary tectonic activity concentrated along the western border of the Sierra Nevada with active normal faulting and isostatic-driven folding occurring coevally. Compressional E-W oriented folding seems to have lesser activity in Quaternary times than the NNE-SSW folds, since they do not generate a linear front in the northern Sierra Nevada. Strike-slip faulting might be active along the southern mountain front, joining the normal fault-bounded western Sierra Nevada mountain front to the normal fault-bounded western Sierra de Gador mountain front. This model explains the distribution of geomorphic indexes and the topography of the Sierra Nevada and the surrounding Neogene-Quaternary sedimentary basins. Especially interesting is the very different topography and landscape of the Granada and Guadix-Baza basins. The Granada basin located to the west of the Sierra Nevada has a mean altitude of 600 m, being scarcely incised by the fluvial network, except in the margins of the basin near to the fault-bounded mountain front (Pérez-Peña et al., 2009c). On the contrary, the Guadix-Baza basin located to the north of the Sierra Nevada has a mean altitude of 1000 m, with the fluvial network

deeply incised (down to 200 m; Pérez-Peña et al., 2009b) into the Neogene-Quaternary infill. These topographic and geomorphic differences are probably due to the different tectonic location of the two basins: The Granada basin is located in the hanging wall of the SW-directed extensional system bounding to the west the Sierra Nevada, being thus subjected in a great extent to Quaternary subsidence. On the contrary, the Guadix-Baza basin is located in the footwall of the above-mentioned extensional system, being part together with the whole Sierra Nevada of a single block suffering tectonic uplift during the Quaternary.

Acknowledgements: This study was supported by the grants CGL2004-03333/BTE and TOPO-IBERIA CONSOLIDER-INGENIO CSD2006-00041 of the Spanish Ministry of Education. We are indebted to Christine Laurin for revising the English.

7

CONCLUSIONS / CONCLUSIONES

ARCGIS-BASED ATOMATED AND RE-FORMULATED GEOMORPHIC INDEXES

This thesis provides some ArcGIS-based methods for relief analysis and evaluation of recent tectonics. The primary data for these calculations mainly come from drainage networks, especially from parameters such as stream gradient and catchment hypsometry. Thus, we have improved previously defined geomorphic indexes in two aspects: (i) we have automatized their calculation by developing specific ArcGIS-based software, and (ii) we have applied geostatistic techniques to them in order to perform better spatial analyses.

The SL index is one of the most broadly used geomorphic indexes to characterize active tectonics. However, this index is strongly dependent on stream length, thus failing when applied to areas with different drainage density and/or stream lengths. To avoid these problems, we have normalized this index and renamed it as SLk index. Thus, the use of the SLk index allows using rivers of different lengths and generating SLk anomaly maps. We have refined SLk anomaly map calculation by using geostatistic techniques. A comparison of SLk anomaly maps with classic SL maps in the NE border of the Granada basin shows how the re-formulated index gives way to better defined anomalies, i.e. anomalies adapt better to active structures and/or lithological contacts with contrasting strengths.

Hypsometry is also a valuable tool in active tectonic studies, though manual calculation of hypsometry-derived geomorphic indexes is very tedious. For this reason, we have presented a new ArcGIS extension to automatically extract hypsometric curves from Digital Elevations Models (DEM). This extension has been programmed in Visual Basic using ArcOjects architecture. It applies a method based on the integer data model of ArcGIS, operating very efficiently within its environment. This new tool can be used to analyze and visualize multiple hypsometric curves altogether and directly within the ArcMap main windows. It also allows extracting some curve-related statistic parameters, such as kurtosis, density kurtosis, skew, density skew and hypsometric integral. As an example of use of this new tool, we have studied some rivers of the eastern termination of Sierra Nevada. The differences between the northern and southern slope hypsometric curves fit with the main tectonic setting envisaged for both mountain fronts. The southern slope curves show a younger erosional stage due to the recent tectonic activity along the faults bounding the mountain front. The northern slope presents some curve-shapes characteristic of basin rejuvenation, probably induced by capture processes. The statistics related to the hypsometric curves also provide useful information regarding the erosion stage of the catchments. In the

case studied, the erosion rates deduced for the Quaternary seem to decrease eastwards, thus suggesting a decrease in tectonic activity in the same direction.

To improve hypsometry-based geomorphic indexes, we have applied Local Indicators of Spatial Autocorrelation (LISA) to hypsometric integral (HI) value distributions. To do so, we have used the Moran's I and the Getis-Ord* statistics. We have calculated HI values for regular squares in the Genil watershed, which includes most of the Granada Neogene-Quaternary sedimentary basin. This analysis shows that the raw estimation of HI values does not define a clear view of grouped high or low values. However, the application of Moran's I statistics to the HI data reveals that actually they are distributed in clusters, which, in turn, can be correlated with recently uplifted and subsided areas of the Granada basin. By applying a hot-spot analysis Getis-Ord (Gi*) statistics, we can better visualize clusters of high or low HI values. We have tested scale-dependence of this analysis by using different grid-sizes and DEM showing that HI value distributions are independent from DEM resolution and dependent on the scale. This method has also been tested in an region of well-known recent tectonic activity, the Central Otago region in New Zealand, where the clusters of high HI values clearly define the uplifted areas affected by active folds. Therefore, the use of LISA permits the extraction of clusters of high and low HI values that can reflect active tectonic processes.

QUATERNARY LANDSCAPE EVOLUTION OF THE SIERRA NEVADA AND SURROUNDING NEOGENE BASINS

The ArcGIS-based automated and re-formulated geomorphic indexes developed in this thesis have been applied to the Sierra Nevada and surrounding sedimentary basins with the idea of gaining knowledge on their Quaternary tectonic activity. The indexes obtained suggest that the more recent uplift is concentrated along the western mountain front of the Sierra Nevada, where Smf and Vf present the lowest values. On the contrary, the northern mountain front presents the lowest values of Smf and Vf, thus pointing to low recent tectonic activity. As for the southern mountain front, the Smf and Vf indexes are low, but their interpretation is not obvious in terms of tectonic activity because the Guadalfeo river runs parallel to this mountain front and the values might be conditioned by the river-valley morphology. Hypsometric curves of the main catchments of the Sierra Nevada present subtle E-W and N-S variations. N-S variations are mainly due to the fact that local base-level is ≈1100 m in the northern mountain front and ≈600 m in the southern one, i.e. southern slope streams have more erosional power than northern ones. River entrenchment in the southern slope of Sierra Nevada increases westward, thus pointing to higher recent uplift and tectonic activity concentrated along the western mountain front. Finally, the catchment asymmetry factors calculated show systematic asymmetries at both sides of the Lanjarón

river. These asymmetries are probably due to NNE-SSW oriented active folding related to the unroofting produced by the normal faults bounding the western Sierra Nevada mountain front. Our conclusions are corroborated by the scarce Quaternary uplift rates available, which increase westward, as well as by surface geology and distribution of present-day seismicity. Geological mapping shows that the southern and western mountain fronts of the Sierra Nevada are fault-bounded, while the northern one corresponds to an unconformity between the Neogene-Quaternary sedimentary infill of the Guadix-Baza basin and the metamorphic rocks of the Sierra Nevada. Moreover, the southern mountain front has been interpreted as a transfer fault linking two areas of active extension and intense present-. day seismicity (the Western Sierra Nevada mountain front and the western Sierra de Gádor mountain front).

The Quaternary landscape evolution of the Guadix-Baza basin is mostly dominated by erosional processes following its capture by the Guadalquivir river. In order to better understand its evolution, we have developed a methodology to estimate Quaternary erosion rates. This methodology is based on the reconstruction of the relief prior to river entrenchment by using as a reference level a flat elevated surface (glacis) that marks the end of sedimentation in this basin. To do so, we have used all the cells in the DEM that correspond to this reference surface, in order to obtain the original morphology of the basin before the endorheic–exorheic transition. Erosion rates are based on a numerical age available for a laminar calcrete that appears on top of the sedimentary sequence and marks the glacis surface. By comparing the present-day topography and the restored glacis surface, we have obtained not only the erosion rates for the whole Guadix–Baza basin, but also a snapshot of how erosion is distributed. The high (6.47 – 4.28 m ha^{-1} yr^{-1}) erosion rates obtained are one order of magnitude higher than the regional uplift rates. This decoupling between erosion and uplift rates seems to be basically controlled by two factors; i) the drastic base level fall occurred in Late Pleistocene times when the former endorheric Guadix-Baza basin was captured by the Guadalquivir River, and ii) the poorly consolidated nature of the sediments in the basin. The higher erosion rates obtained in the Guadix sub-basin with respect to the Baza sub-basin are controlled by three different factors: the position of the capture point closer to the Guadix sub-basin, the greater area of the Baza sub-basin and the Quaternary activity of the Baza normal fault, which has downthrown the Baza sub-basin block (hanging wall) with respect to the Guadix sub-basin one (footwall).

The Quaternary landscape evolution of the Granada basin is dominated by active normal faulting, mostly concentrated along its NE border. This basin, located to the west of the Sierra Nevada, has a mean altitude of 600 m, being scarcely incised by the fluvial network, except in the NE margin near to the fault-bounded mountain fronts of western Sierra

Nevada and southern Sierra Arana-Alfaguara. The Guadix-Baza basin, located to the north of the Sierra Nevada, has a mean altitude of 1000 m, with the fluvial network deeply incised (down to 200 m) into the Neogene-Quaternary infill. Thus, average altitude and river entrenchment in the Granada basin are lower than in the neighboring Guadix-Baza basin. These fundamental landscape differences seem to be strongly controlled by the tectonic location of these two basins: The Granada basin is located in the hanging wall of the SW-directed extensional system bounding the western Sierra Nevada, being thus subjected in a great extent to Quaternary subsidence. On the contrary, the Guadix-Baza basin is located in the footwall of the above-mentioned extensional system, being part together with the whole Sierra Nevada of a single block suffering tectonic uplift during the Quaternary.

ÍNDICES GEOMORFOLÓGICOS BASADOS EN SIG AUTOMATIZADOS Y REFORMULADOS

En esta tesis se han presentando nuevas herramientas y metodologías para el análisis del relieve y la evaluación de la actividad tectónica reciente basadas en SIG. Estas metodologías usan principalmente como dato de partida las redes de drenaje y diversos índices geomorfológicos asociados a ellas. Se ha automatizado y mejorado el cálculo de índices geomorfológicos previos básicamente en dos aspectos: i) se ha automatizado su cálculo por medio de nuevos métodos diseñados específicamente para GIS, y ii) se han aplicado técnicas geoestadísticas con el fin de realizar análisis espaciales más significativos

El índice SL es uno de los índices geomorfológicos más usados para caracterizar actividad tectónica. Sin embargo la formulación original de este índice hace que este muy influenciado por la longitud del río analizado, y por tanto, que su aplicación en redes de drenaje con ríos de diferentes longitudes. Para evitar este problema, en esta tesis se ha propuesto el uso de un re-definido y normalizado índice SLk. Este nuevo índice permite la comparación de ríos de longitudes diferentes y la generación de mapas de anomalías de SLk. Se ha propuesto un nuevo método para el cálculo de mapas de anomalías de SLk por medio de técnicas geoestadísticas. La comparación del mapa de anomalías de SLk generado para el borde NE de la cuenca de Granada se adapta mejor a las estructuras tectónicamente activas y/o litología que un mapa clásico de índice SL sin normalizar.

La hipsometría es una herramienta muy útil para la evaluación de la tectónica reciente, sin embargo el cálculo tradicional de la misma resulta muy tedioso. En esta tesis se ha presentado una nueva extensión para ArcGIS para la extracción automática de curvas hipsométricas a partir de Modelos Digitales del Terreno (MDT). Esta extensión ha sido programada en Visual Basic usando la arquitectura de objetos ArcObjects. Para el cálculo de curvas hipsométricas se aplica un método que se basa en las características de los modelos

raster enteros de ArcGIS, y por lo tanto se adapta muy eficientemente a este entorno. Esta nueva herramienta se puede usar para analizar y visualizar múltiples curvas hipsométricas directamente dentro del entorno de ArcMap. Permite asimismo la extracción de los momentos estadísticos relacionados con la curva hipsométrica. Como ejemplo de uso de esta extensión, se ha realizado un análisis en la terminación este de Sierra Nevada. Las diferencias entre las curvas hipsométricas de las vertientes norte y sur definen fehacientemente las características tectónicas de ambos bordes. El borde sur muestra un estadio erosional más reciente debido a la actividad tectónica de las fallas que lo limitan. Las curvas del norte presentan características de rejuvenecimiento debido a un proceso de captura fluvial de las cuencas por la red de drenaje del río Andaráx. Los estadísticos analizados sugieren un decremento de las tasas de erosión Cuaternarias hacía el este, probablemente relacionado con una menor actividad tectónica en la misma dirección.

Se ha introducido la aplicación de índices locales de autocorrelación espacial a las distribuciones de valores de integral hipsométrica (HI). Los valores de HI se han extraído para cuadrados regulares en la cuenca hidrográfica del río Genil (la cual engloba a la cuenca sedimentaria de Granada). El análisis realizado en este trabajo muestra que la estimación "cruda" de los valores de HI es difusa, siendo imposible discernir patrones de distribución de estos valores. Sin embargo cuando se aplican índices de autocorrelación espacial, se muestran clusters claros de agrupación de altos y bajos valores de HI. Se han analizado las relaciones y posibles influencias del modelo utilizado (fuente del mismo y resolución) sobre los análisis de HI, así como las posibles relaciones con la litología y la posición relativa dentro de la cuenca hidrográfica. Los valores de HI no tienen una relación directa ni con la litología ni con la posición relativa dentro de la cuenca. La distribución de los clusters de HI, es robusta independientemente del DEM utilizado, pero está influenciada por la escala. Una vez este método ha sido puesto a punto en la cuenca de Granada, se ha verificado exitosamente la aplicabilidad del mismo en un area de conocía actividad tectónica como es la región central de Otago en la isla sur de Nueva Zelanda.

EVOLUCION CUATERNARIA DEL RELIEVE EN SIERRA NEVADA Y CUENCAS NEOGENAS DE GUADIX-BAZA Y GRANADA

Finalmente, las herramientas presentadas anteriormente, junto con otros índices geomorfológicos, se han aplicado en Sierra Nevada para evaluar su actividad tectónica. Los índices geomorfológicos calculados sugieren que el levantamiento más reciente de la misma está concentrado en su frente oeste, donde se encuentran los valores más bajos de Smf y Vf. Por el contrario el frente norte presenta los valores más altos de Smf y Vf, sugiriendo por tanto una actividad tectónica menor en el cuaternario. El frente sur de Sierra Nevada también presenta valores bajos de Vf y Smf, aunque su interpretación no es tan obvia en

términos de tectónica activa, puesto que el río Guadalfeo discurre paralelo a este frente y podría condicionar su morfología. Las curvas hipsométricas calculadas para Sierra Nevada muestran diferencias entre las vertientes norte y sur. Estas variaciones pueden ser debidas al hecho de que el nivel de base en la vertiente norte está situado a 1100 metros y en la sur a 600 metros, por lo que los ríos de la vertiente sur tendrían un poder erosivo mayor. La incisión fluvial se incrementa en la parte oeste de Sierra Nevada, sugiriendo a un levantamiento más reciente del frente oeste. Por último, las asimetrías calculadas muestran variaciones sistemáticas a ambos lados del río Lanjarón. Estas asimetrías están debidas con pliegues de dirección NNE-SSW relacionados con la actividad tectónica de las fallas que limitan el frente oeste de Sierra Nevada. Estas conclusiones avalan las tasas de levantamiento existentes (las cuales se incrementan en el oeste) y la distribución de la sismicidad actual.

La evolución cuaternaria del relieve en la cuenca de Guadix-Baza esta principalmente dominada por procesos erosivos desencadenados desde la captura de la misma por el río Guadalquivir. Para comprender mejor esta evolución, se ha desarrollado una metodología para la reconstrucción de la morfológica de la cuenca previa al encajamiento de la red de drenaje. Esta superficie se corresponde con un glacis compuesto por una calcreta laminar que marca el final de la sedimentación en la cuenca. Para ello se han seleccionado todas las celdas del MDE que se corresponden con esta superficie. Las tasas de erosión se han calculado tomando como referencia la edad de esta superficie. Mediante la comparación de la superficie actual de la cuenca y del modelo reconstruido, no solo se han obtenido las tasas de erosión, sino también su distribución espacial. Las altas tasas de erosión calculadas (6.47 – 4.28 m ha-1 año-1) son un orden de magnitud mayor que las tasas de elevación. Este desajuste parece debido a la combinación de dos factores; i) el drástico descenso de nivel de base que supone la captura de la cuenca endorreica de Guadix-Baza por el río Guadalquivir; ii) Los sedimentos pobremente consolidados de la cuenca. Las tasas de erosión mayores en la sub-cuenca de Guadix respecto a la sub-cuenca de Baza están debidas a tres factores diferentes; i) la posición del punto de captura dentro de la sub-cuenca de Guadix, ii) la mayor área de la sub-cuenca de Baza, y iii) la actividad Cuaternaria de la falla de Baza, que actúa hundiendo el bloque donde se sitúa la sub-cuenca de Baza y por tanto supone una barrera para el avance de la erosión.

La evolución Cuaternaria del relieve en la cuenca de Granada está dominada por la actividad de fallas normales. Esta cuenca está situada al oeste de Sierra Nevada tiene una altitud media de 600 metros, y esta levemente encajada por la red de drenaje a lo largo del rio Genil (drenaje axial de la misma hacia el río Guadalquivir). Sin embargo su margen NE presenta un notable encajamiento situado en el bloque de muro de un sistema de fallas normales que conecta con el sistema que limita el oeste de Sierra Nevada. La cuenca de

Guadix-Baza, situada al norte de Sierra Nevada está muy encajada por la red de drenaje (hasta 200 metros en algunos puntos). Estas diferencias entre ambas cuencas parecen estar controladas por su localización: La cuenca de Granada se sitúa en el bloque de techo del sistema extensional de dirección SO que limita el oeste de Sierra Nevada, y está por lo tanto sujeta a extensión en el Cuaternario. Por el contrario la cuenca de Guadix-Baza está localizada en el bloque de techo de dicho sistema, siendo elevada conjuntamente con Sierra Nevada durante el Cuaternario.

8

REFERENCES

Alfaro, P., Delgado, J., Sanz de Galdeano, C., Galindo-Zaldívar, J., García-Tortosa, F.J., López-Garrido, A.C., López-Casado, C., Marín-Lechado, C., Gil, A., Borque, M.J., 2007. The Baza Fault: a major active extensional fault in the central Betic Cordillera (south Spain). *International Journal of Earth Science (Geologische Rundschau),* **97:** 1353-1365.

Alfaro, P., Galindo-Zaldívar, J., Jabaloy, A., López-Garrido, A.C., Sanz de Galdeano, C., 2001. Evidence for the activity and paleoseismicity of the Padul fault (Betic Cordillera, SE Spain). *Acta Geológica Hispánica*, **36**: 283-295.

Amrhein, C., Reynolds, H., 1997, Using the Getis statistic to explore aggregation effects in Metropolitan Toronto Census data. *Canadian Geographer-Geographe Canadien*, **41**: 137-149.

Anselin, L., 1995. Local Indicators of Spatial Association–LISA. *Geographical Analysis*, **27:** 93-115.

Argus, D.F., Gordon, R.G., de Mets, C., Stein, S., 1989. Closure of the Africa-Eurasia-North America Plate Motion Circuit and Tectonics of the Gloria Fault. *Journal of Geophysical Research*, **94**: 5585-5602.

Azañón, J.M., Azor, A., Booth-Rea, G., Torcal, F., 2004. Small-scale faulting, topographic steps and seismic ruptures in the Alhambra (Granada, southeast Spain). *Journal of Quaternary Science*, **19**: 219-227.

Azañón, J.M., Azor, A., Pérez-Peña, J.V., Carrillo, J.M., 2005. Late Quaternary large-scale rotational slides induced by river incision: The Arroyo de Gor area (Guadix basin, SE Spain). *Geomorphology*, **69**: 152-168.

Azañón, J.M., Crespo-Blanc, A., 2000. Exhumation during a continental collision inferred from the tectonometamorphic evolution of the Alpujarride Complex in the central Betics (Alboran Domain, SE Spain). *Tectonics*, **19**: 549-565.

Azañón, J.M., García-Dueñas, V., Martínez-Martínez, J.M., Crespo-Blanc, A., 1994. Alpujarride tectonic sheets in the central Betics and similar eastern allochthonous units (SE Spain). *C.R. Acad. Sci. II A* **318**: 667-674.

Azañón, J.M., Tuccimei, P., Azor, A., Sánchez-Almazo, I.M., Alonso-Zarza, A.M., Soligo, M., Pérez-Peña, J.V., 2006. Calcrete features and age estimates from U/Th dating: Implications for the analysis of Quaternary erosion rates in the northern limb of the Sierra Nevada range (Betic Cordillera, southeast Spain). In: A.M. Alonso-Zarza, L.H. Tanner (Eds.), *Paleoenvironmental Record and Applications of Calcretes and Palustrine Carbonates*. Geological Society of America Special Paper, pp. 223-239.

Azor, A., Keller, E.A., Yeats, R.S., 2002. Geomorphic indicators of active fold growth: South Mountain-Oak Ridge anticline, Ventura basin, southern California. *Geological Society of America Bulletin*, **114**(6): 745-753.

Balanyá, J.C., García-Dueñas, V., 1988. El Cabalgamiento cortical de Gibraltar y la tectónica de Béticas y Rif. II Congreso Geológico de España. Simposium sobre Cinturones Orogénicos, Granada.

Band, L.E., 1986. Topographic partition of watersheds with digital elevation models. *Water Resources Research*, **22**: 15-24.

Banda, E., Gallart, J., García-Dueñas, V., Danobeitia, J.J., Makris, J., 1993. Lateral variation of the crust in the Iberian Peninsula - New evidence from the Betic Cordillera. *Tectonophysics*, **221**(1): 53-66.

Bischoff, J.L., Fitzpatrick, J.A., 1991. U-series dating of impure carbonates: An isochron technique using total sample dissolution. *Geochimica et Cosmochimica Acta*, **55**: 543-554.

Bishop, P., 2007. Long-term landscape evolution: linking tectonics and surface processes. *Earth Surface Processes and Landforms*, **32**(3): 329-365.

Blumenthal, M., 1927. Versucheiner tektonischen gliederung der Betischen-Cordilleren von central and süd-west Andalusien. *Eclogae Geologicae Helvetica*, **10**: 487-532.

Booth-Rea, G., Azañón, J.M., Azor, A., García-Dueñas, V., 2004. Influence of strike-slip fault segmentation on drainage evolution and topography. A case study: The Palomares Fault Zone (southeastern Betics, Spain). *Journal of Structural Geology*, **26**(9): 1615-1632.

Botella, M., Martínez, C., Cárdenas, F.J., 1985. Las industrias paleolíticas de la Cueva Horá (Darro, Granada). *Antropología y Paleoecología Humana*, **1**: 59-74.

Braga, J.C., Martín, J.M., Quesada, C., 2003. Patterns and average rates of late Neogene-Recent uplift of the Betic Cordillera, SE Spain. *Geomorphology*, **50**(1-3): 3-26.

Brocklehurst, S.H., Whipple, K.X., 2002. Glacial erosion and relief production in the Eastern Sierra Nevada, California. *Geomorphology*, **42**(1-2): 1-24.

Brookfield, M.E., 1998. The evolution of the great river systems of southern Asia during the Cenozoic India-Asia collision: rivers draining southwards. *Geomorphology*, **22**(3-4): 285-312.

Brozovic, N., Burbank, D.W., Fielding, E., Meigs, A.J., 1995. The spatial and temporal topographic evolution of Wheeler Ridge California: new insights from digital elevation data. *Geological Society of America Abstracts with Programs*, **27**: 395.

Buforn, E., Bezzeghoud, M., Udias, A., Pro, C., 2004. Seismic sources on the Iberia-African plate boundary and their tectonic implications. *Pure and Applied Geophysics*, **161**(3): 623-646.

Bull, W.B., 1977. Tectonic geomorphology of the Mojave Desert. *U.S. GEological Survey Contract Report 14-08-001-G-394*

Bull, W.B., 1991. Geomorphic response to climatic change. Oxford University Press, Oxford, 326 pp.

Bull, W.B., McFadden, L.D., 1977. Tectonic geomorphology north and south of the Garlock fault, California. In: D.O. Doehering (Ed.), *Geomorphology in arid regions. Proccedings at the Eighth Annual Geomorphology Simposium*. State University of New York, Binghamton, NY, pp. 115-138.

Burbank, D.W., Anderson, R.S., 2001. Tectonic Geomorphology. Blackwell Science, Oxford, 247 pp.

Burbank, D.W., Leland, J., Fielding, E., Anderson, R.S., Brozovic, N., Reid, M.R., Duncan, C., 1996. Bedrock incision, rock uplift and threshold hillslopes in the northwestern Himalayas. *Nature*, **379**: 505-510.

Calvache, M.L., Viseras, C., 1997. Long-term control mechanisms of stream piracy processes in Southeast Spain. *Earth Surface Processes and Landforms*, **22**: 93-105.

Carrara, A., Cardinali, M., Detti, R., Guzzetti, F., Pasqui, V., Reichenbach, P., 1991. GIS techniques and statistical-models in evaluating landslide hazard. *Earth Surface Processes and Landforms*, **16**(5): 427-445.

Carrara, A., Cardinali, M., Guzzetti, F., Reichenbach, P., 1993. GIS technology in mapping landslide hazard. In: A. Carrara , F. Guzzetti (Eds.), International Workshop on Geographical Information Systems in Assessing Natural Hazards, Perugia, Italy, pp. 135-175.

Carvajal, R., Sanz de Galdeano, C., 2001. La red de drenaje de la red nororiental de la Cuenca de Granada. Del río Bermejo al Darro. Aplicación de índices geomorfológicos. In: C. Sanz de Galdeano, J. Pelaez Montilla , A.C. López Garrido (Eds.), *La cuenca de Granada. Estructura, tectónica activa, sismicidad, geomorfología y dataciones existentes.* Universidad de Granada, Granada, pp. 67-77.

Chen, Y.C., Sung, Q.C., Cheng, K.Y., 2003. Along-strike variations of morphotectonic features in the Western Foothills of Taiwan: tectonic implications based on stream-gradient and hypsometric analysis. *Geomorphology*, **56**(1-2): 109-137.

Ciccacci, S., D'Alessandro, L., Fredi, P., Lupia-Palmeri, E., 1992. Relations between morphometric characteristics and denudational processes in some drainage basins of Italy. *Zeitschfirt für Geomorphology*, **36**(1): 53-67.

Ciccacci, S., Fredi, P., Lupia Palmieri, E., Pugliese, F., 1981. Contributo dell'analisi geomorfica quantitativa alla valutazione dell'entità dell'erosione nei bacini fluviali. *Bollettino della Società Geologica Italiana*, **99**: 455-516.

Ciccacci, S., Fredi, P., Lupia Palmieri, E., Pugliese, F., 1986. Indirect evaluation of erosion entity in drainage basins through geomorphic, climatic and hydrological parameters. *International Geomorphology*, **2**: 33-48.

Clark, M.K., Schoenbohm, L.M., Royden, L.H., Whipple, K.X., Burchfiel, B.C., Zhang, X., Tang, W., Wang, E., Chen, L., 2004. Surface uplift, tectonics, and erosion of eastern Tibet from large-scale drainage patterns. *Tectonics*, **23**(1), DOI: 0.1029/2002TC001402

Cloetingh, S., Cornu, T., 2005. Surveys on environmental tectonics. *Quaternary Science Reviews*, **24**(3-4): 235-240.

Comas, M.C., García-Dueñas, V., Jurado, M.J., 1992. Neogene tectonic evolution of the Alboran Sea from MCS data. *Geo-Marine Letters*, **12**(2-3): 157-164.

Comas, M.C., Platt, J.P., Soto, J.I., Watts, A.B., 1999. The origin and tectonic history of the Alboran Basin: Insights from Leg 161 results. In: R. Zahn, M.C. Comas, A. Klaus (Eds.), *Proc. ODP, Sci Results*. Ocean Drilling Program, College Station, TX, pp. 555-579.

Cox, R.T., 1994. Analysis of drainage-basin symmetry as a rapid technique to identify areas of possible Quaternary tilt-block tectonics: An example from the Mississippi embayment. *Geological Society of America Bulletin*, **106**(5): 571-581.

D'Alessandro, L., Del Monte, M., Fredi, P., Lupia-Palmeri, E., Peppoloni, S., 1999. Hypsometric analysis in the study of italian drainage basin morphoevolution. *Transactions, Japanese Geomorphological Union*, **20**(3): 187-202.

Dadson, S.J., Hovius, N., Chen, H.G., Dade, W.B., Hsieh, M.L., Willett, S.D., Hu, J.C., Horng, M.J., Chen, M.C., Stark, C.P., Lin, J.C., 2003. Links between erosion, runoff variability and seismicity in the Taiwan orogen. *Nature*, **426**: 648-651.

Dai, F.C., Lee, C.F., 2002. Landslide characteristics and, slope instability modeling using GIS, Lantau Island, Hong Kong. *Geomorphology*, **42**(3-4): 213-228.

Davis, J.C., 1986. Statistic and data analysis in geology. John Wiley and Sons, New York, 564 pp.

de Mets, C., Gordon, R.G., Argus, D.F., Stein, S., 1994. Effect of recent revisions to the geomagnetic reversal time-scale on estimates of current plate motions. *Geophysical Research Letters*, **21**: 2191-2194.

Della Seta, M., Del Monte, M., Fredi, P., Palmieri, E.L., 2007. Direct and indirect evaluation of denudation rates in Central Italy. *Catena*, **71**(1): 21-30.

Deutsch, C.V., Journel, A.G., 1992. GSLIB Geostatistical Software Library and User's Guide. Oxford University Press, New York, 384 pp.

Dewey, J.F., Helman, M.L., Turco, E., Hutton, D.H.W., Knott, S.D., 1989. Kinematics of the western Mediterranean. In: M.P. Coward, D. Dietrich , R.G. Park (Eds.), *Alpine Tectonics*. Geological Society of London Special Publication, London, pp. 265-283.

Didon, W.P., Durand Delga, M., Kornprobst, J., 1973. Homologies géologiques entre les deux rives du détroit de Gigraltar. *Bulletin de la Societe Geologique de France*, **7**(15): 77-105.

Diniz, J. A.F., L.M. Bini, Hawkins B.A., 2003. Spatial autocorrelation and red herrings in geographical ecology, *Global Ecolology and Biogeography*, **12**: 53-64.

Duggen, S., Hoernle K., van den Bogaard, P., Rupke, D., Morgan, J.P., 2003. Deep roots of the Messinian salinity crisis, *Nature*, **422**: 602-606.

Dumont, J.F., Santana, E., Vilema, W., 2005. Morphologic evidence of active motion of the Zambapala Fault, Gulf of Guayaquil (Ecuador). *Geomorphology*, **65**(3-4): 223-239.

Dunne, T., Leopold, L.B., 1978. Water in Environmental Planning. Freeman and Company, New York, 818 pp.

Durand-Delga, M., Rossi, P., Olivier, P., Puglisi, D., 2000. Structural setting and ophiolitic nature of Jurassic basic rocks associated with the Maghrebian flyschs in the Rif (Morocco) and Sicily (Italy). *C.R. Acad. Sci. II A* **331**(1): 29-38.

Egeler, C.G., 1963. On the tectonics of the eastern Betic Cordilleras (SE Spain). *Geologische Rundschau*, **53**: 260-269.

El Hamdouni, R., Irigaray, C., Fernández, T., Chacon, J., Keller, E.A., 2008. Assessment of relative active tectonics, southwest border of the Sierra Nevada (southern Spain). *Geomorphology*, **96**(1-2): 150-173.

England, P., Molnar, P., 1990. Surface uplift, uplift of rock, and exhumation of rocks. *Geology*, **18**(12): 1173-1177.

Fallot, P., 1948. Les Cordillères Bétiques. *Estudios geologicos*, **4**(7-8): 259-279.

Fernández, J., Viseras, C., Soria, J., 1996. Stratigraphic architecture of the Neogene basins in the central sector of the Betic Cordillera (Spain): tectonic control and base-level changes. In: P.F. Friend , C. Dabrio (Eds.), *Tertiary Basins of Spain: The Stratigraphic Record of Crustal Kinematics*. Cambridge Univ. Press, Cambridge, pp. 353-365.

Finlayson, D.P., Montgomery, D.R., 2003. Modeling large-scale fluvial erosion in geographic information systems. *Geomorphology*, **53**(1-2): 147-164.

Flinch, J.F., 1996. Accretion and extensional collapse of the external Western Rif (Northern Morocco). In: P.A. Ziegler , F. Norvath (Eds.), *Peri-Tethys Memoir II: Structure and Prospects of Alpine Basins and Forelands*. PeriTethys Memoir. Mémoires du Muséum national d'Histoire naturelle, Paris, pp. 61-85.

Fredi, P., Peppoloni, S., 2002. Recent uplift and plano-altimetric configuration in some italian drainage basins. In: F. Dramis, P. Farabollini, P. Molin (Eds.), Large-scale vertical movements and related gravitational processes. Studi Geologici Camerti, Camerino-Rome, pp. 95-101.

Galindo-Zaldívar, J., Gil, A.J., Borque, M.J., González-Lodeiro, F., Jabaloy, A., Marín-Lechado, C., Ruano, P., Sanz de Galdeano, C., 2003. Active faulting in the internal zones of the central Betic Cordilleras (SE, Spain). *Journal of Geodinamics*, **36**: 239-250.

Galindo-Zaldívar, J., Jabaloy, A., Serrano, I., Morales, J., González-Lodeiro, F., Torcal, F., 1999. Recent and present-day stresses in the Granada Basin (Betic Cordilleras): Example of a late Miocene-present-day extensional basin in a convergent plate boundary. *Tectonics*, **18**(4): 686-702.

Galindo Zaldívar, J., González Lodeiro, F., Jabaloy, A., 1989. Progressive extensional shear structures in a detachment contact in the Western Sierra Nevada (Betic Cordilleras, Spain). *Geodinamica Acta*, **3**: 73-85.

García, A.F., Zhu, Z., Ku, T.L., Sanz de Galdeano, C., Chadwick, O.A., Montero, J.C., 2003. Tectonically driven landscape development within the eastern Alpujarran Corridor, Betic Cordillera, SE Spain (Almeria). *Geomorphology*, **50**(1-3): 83-110.

García-Castellanos, D., Fernandez, M., Torne, M., 2002. Modeling the evolution of the Guadalquivir foreland basin (southern Spain). *Tectonics*, **21**(3).

García-Dueñas, V., Balanyá, J.C., Martínez-Martínez, J.M., 1992. Miocene extensional detachments in the outcropping basement of the northern Alborán basin (Betics) and their tectonic implications. *Geo-Marine Letters*, **12**: 88 - 95.

García-Dueñas, V., Martínez-Martínez, J.M., Soto, J.I., 1988. Los Nevado-Filábrides, una pila de pliegue-mantos separados por zonas de cizalla, *II Congreso Geológico de España*, Granada.

García-Tortosa, F.J., Alfaro, P., Galindo-Zaldívar, J., Gibert, L., López-Garrido, A.C., Sanz de Galdeano, C., Ureña, M., 2008. Geomorphologic evidence of the active Baza Fault (Betic Cordillera, South Spain). *Geomorphology*, **97**(3-4): 374-391.

García Hernández, M., López Garrido, A.C., Rivas, P., Sanz de Galdeano, C., Vera, J.A., 1980. Mesozoic paleogeographic evolution the External Zones of the Betic Cordillera. *Geologie en Mijnbouw*, **59**: 155-168.

Getis, A., Ord, K., 1996. Local spatial statistics: an overview. In: P., Longley, M., Batty (Eds.), *Spatial Analysis: Modelling in a GIS Environment. Geo-Information International*, Cambridge, pp 261-277.

Giménez, J., Suriñach, E., Goula, X., 2000. Quantification of vertical movements in the eastern Betics (Spain) by comparing levelling data. *Tectonophysics*, **317**(3-4): 237-258.

Goldrick, G., Bishop, P., 2007. Regional analysis of bedrock stream long profiles: evaluation of Hack's SL form, and formulation and assessment of an alternative (the DS form). *Earth Surface Processes and Landforms*, **32**: 649-671.

Goovaerts, P., 1997. Geostatistics for Natural Resources Evaluation. Oxford University Press, New York, 483 pp.

Hack, J.T., 1957. Studies of longitudinal profiles in Virginia and Maryland. *U.S. Geol. Surv. Prof. Pap.*, **294-B**: 1.

Hack, J.T., 1973. Stream profile analysis and stream-gradient index. *J. Res. U.S. Geol. Surv.*, **1**(4): 421-429.

Hancock, G.S., Anderson, R.S., 2002. Numerical modeling of fluvial strath-terrace formation in response to oscillating climate. *Geological Society of America Bulletin*, **114**(9): 1131-1142.

Hare, P.W., Gardner, T.W., 1985. Geomorphic indicators of vertical neotectonism along converging plate margins, Nicoya Peninsula, Costa Rica. In: M. Morisawa, J.T. Hack (Eds.), *Tectonic Geomorphology: Proccedings of the 15th Annual Bighamton Geomorphology Symposium*. Allen & Unwin, Boston, pp. 75-104.

Harkins, N.W., Anastasio, D.J., Pazzaglia, F.J., 2005. Tectonic geomorphology of the Red Rock fault, insights into segmentation and landscape evolution of a developing range front normal fault. *Journal of Structural Geology*, **27**(11): 1925-1939.

Harlin, J.M., 1978. Statistical moments of the hypsometric curve and its density function. *Mathematical Geology*, **10**(1): 59-72.

Hetzel, R., Niedermann, S., Ivy-Ochs, S., Kubik, P.W., Tao, M.X., Gao, B., 2002. Ne-21 versus Be-10 and Al-26 exposure ages of fluvial terraces: the influence of crustal Ne in quartz. *Earth and Planetary Science Letters*, **201**(3-4): 575-591.

Hovius, N., 2000. Macroscale process systems of mountain belt erosion. In: M.A. Summerfield (Ed.), *Geomorphology and Global Tectonics*. Wiley and Sons, Chichester, pp. 77-105.

Howard, A.D., 1990. Role of hypsometry and planform in basin hydrologic response. *Hydrological Processes*, **4**: 373-385.

Howard, A.D., Kerby, G., 1983. Channel Changes in Badlands. *Geological Society of America Bulletin*, **94**(6): 739-752.

Huang, X.J., Niemann, J.D., 2006. An evaluation of the geomorphically effective event for fluvial processes over long periods. *Journal of Geophysical Research-Earth Surface*, **111**, DOI: 10.1029/2006JF000477.

Hurtrez, J. E., Lucazeau, F., 1999. Lithological control on relief and hypsometry in the Herault drainage basin (France), *C.R. Acad. Sci. II A,* **328**: 687-694.

Hurtrez, J.E., Sol, C., Lucazeau, F., 1999. Effect of drainage area on hypsometry from an analysis of small-scale drainage basins in the Siwalik Hills (central Nepal). *Earth Surface Processes and Landforms*, **24**: 799-808.

Iribarren, L., Verges, J., Camurri, F., Fullea, J., Fernandez, M., 2007. The structure of the Atlantic-Mediterranean transition zone from the Alboran Sea to the Horseshoe Abyssal Plain (Iberia-Africa plate boundary). *Marine Geology*, **243**(1-4): 97-119.

Isaaks, E.H., Srivastava, R.M., 1989. An introduction to applied geostatistics. Oxford University Press, New York, 592 pp.

Jabaloy, A., Galindo-Zaldívar, J., González-Lodeiro, F., 1992. The Mecina Extensional System - Its Relation with the Post-Aquitanian Piggyback Basins and the Paleostresses Evolution (Betic Cordilleras, Spain). *Geo-Marine Letters*, **12**(2-3): 96-103.

Jackson, J., Ritz, J.F., Siame, L., Raisbeck, G., Yiou, F., Norris, R., Youngson, J., Bennett, E., 2002. Fault growth and landscape development rates in Otago, New Zealand, using in situ cosmogenic Be-10, *Earth and Planetary Science Letters,* **195**: 185-193.

Jackson, J., Leeder, M., 1994. Drainage Systems and the Development of Normal Faults - an Example from Pleasant Valley, Nevada. *Journal of Structural Geology*, **16**(8): 1041-1059.

Jackson, J., Norris, R., 1996. The structural evolution of active fault and fold systems in central Ontago, New Zealand: evidence revealed by drainage patterns. *Journal of Structural Geology*, **18**: 217-234.

Jackson, J., Van Dissen, R., Berryman, K., 1998. Tilting of active folds and faults in the Manawatu region, New Zealand: evidence from surface drainage patterns. *New Zealand Journal of Geology & Geophysics*, **41**: 377-385.

Jain, V., Preston, N., Fryirs, K., Brierley, G., 2006. Comparative assessment of three approaches for deriving stream power plots along long profiles in the upper Hunter River catchment, New South Wales, Australia. *Geomorphology*, **74**(1-4): 297-317.

Johnson, C., 1997. Resolving denudatinoal histories in orogenic belts with apatite fission-track thermocronology and structural data: An example from southern Spain. *Geology*, **25**(7): 623-626.

Jolivet, L., Faccenna, C., 2000. Mediterranean Extension and the Africa-Eurasia Collision. *Tectonics*, **19**(6): 1095-1106.

Journel, A.G., 1986. Geostatistics: Models and tools for the earth sciences. *Mathematical Geology*, **18**: 119-140.

Karssenberg, D., 2002. The value of environmental modelling languages for building distributed hydrological models. *Hydrological Processes*, **16**(14): 2751-2766.

Karssenberg, D., De Jong, K., 2005. Dynamic environmental modelling in GIS: 1. Modeling in three spatial dimensions. *International Journal of Geographical Information Science*, **19**(5): 559-579.

Kaufman, A., Broecker, W., 1965. Comparison of Th230 and C14 ages for carbonate materials from lakes Lahontan and Bonneville. *Journal of Geophysical Research*, **70**(16): 4039-4054.

Keller, E.A., 1986. Investigation of active tectonics: use of surficial earth processes, Active Tectonics. National Academy Press, Washington D.C., 266 pp.

Keller, E.A., Pinter, N., 2002. Active Tectonics. Earthquakes, Uplift, and Landscape. Prentice Hall, New Jersey, 362 pp.

Keller, E.A., Sanz de Galdeano, C., Chacon, J., 1996. Tectonic geomorphology and earthquake hazard of Sierra Nevada, Southern Spain, 1ª Conferencia Internacional Sierra Nevada. Publicaciones Universidad de Granada, Granada, pp. 201-218.

Keller, E.A., Seaver, D.B., Laduzinsky, D.L., Johnson, D.L., Ku, T.L., 2000. Tectonic geomorphology of active folding over buried reverse faults: San Emigdio Mountain front, southern San Joaquin Valley, California. *Geological Society of America Bulletin*, **112**(1): 86-97.

Kirby, E., Whipple, K.X., Tang, W., Chen, Z., 2003. Distribution of active rock uplift along the eastern margin of the Tibetan plateau: Inferences from bedrock channel longitudinal profiles. *Journal of Geophysical Research*, **108**, DOI: 10.1029/2001JB000861.

Knox, J.C., 1976. The concept of the graded stream. In: W. Melhorn , R. Flemal (Eds.), *Theories of Landform Development*. George Allen and Unwin, London, pp. 168-198.

Kobor, J.S., Roering, J.J., 2004. Systematic variation of bedrock channel gradients in the central Oregon Coast Range: implications for rock uplift and shalow landsliding. *Geomorphology*, **62**: 239-256.

Korup, O., 2006. Rock-slope failure and the river long profile. *Geology*, **34**(1): 45-48.

Lan, H.X., Martin, C.D., Lim, C.H., 2007. RockFall analyst: A GIS extension for three dimensional and spatially distributed rockfall hazard modeling. *Computers & Geosciences*, **33**: 262-279.

Leopold, L.B., Maddock, T., 1953. The hydraulic geometry of stream channels and some physiographic implications. *U.S. Geological Survey Proffesional Paper*, **252**.

Lifton, N.A., Chase, C.G., 1992. Tectonic, climatic and lithologic influences on landscape fractal dimension and hypsometry: implications for landscape evolution in the San Gabriel Mountains, California. *Geomorphology*, **5**: 77-114.

Liu, Y.B., Gebremeskel, S., De Smedt, F., Hoffmann, L., Pfister, L., 2003. A diffusive transport approach for flow routing in GIS-based flood modelling. *Journal of Hydrology*, **283**(1-4): 91-106.

Lonergan, L., Platt, J.P., 1995. The Malaguide-Alpujarride boundary - A major extensional contact in the internal zone of the eastern Betic Cordillera, SE Spain. *Journal of Structural Geology*, **17**(12): 1655-1671.

Ludwig, K.R., 1994. Isoplot. A plotting and regression program for radiogenic-isotope data. *U.S. Geological Survey Open-File Report*, 91-445

Luo, W., 1998. Hypsometric analysis with a geographic information system. *Computers & Geosciences*, **24**: 815-821.

Luo, W., 2000. Quantifying groundwater sapping processes with a hypsometric analysis technique. *Journal of Geophysical Research*, **105**: 1685-1694.

Luo, W., 2002. Hypsometric analysis of Margaritifer Sinus and origin of valley networks. *Journal of Geophysical Research-Planets*, **107**, DOI: 10.1029/2001JE001500.

Mackin, J.H., 1948. Concept of the Graded River. *Geological Society of America Bulletin*, **59**(5): 463-511.

Marín-Lechado, C., Galindo-Zaldívar, J., Rodríguez-Fernández, L.R., Serrano, I., Pedrera, A., 2005. Active faults, seismicity and stresses in an internal boundary of a tectonic arc (Campo de Dalías and Níjar, southeastern Betic Cordilleras, Spain). *Tectonophysics*, **396**: 81-96.

Martín-Rojas, I., Martín-Martín, M., Sanz de Galdeano, C., 2001. Índices geomorfológicos de los frentes montañosos del borde occidental de Sierra Nevada (Granada - España). In: C. Sanz de Galdeano, J. Pelaez Montilla , A.C. López Garrido (Eds.), *La cuenca de Granada. Estructura, tectónica activa, sismicidad, geomorfología y dataciones existentes.* Universidad de Granada, Granada, pp. 59-66.

Martínez-Díaz, J.J., Hernández-Enrile, J.L., 2004. Neotectonics and morphotectonics of the southern Almería region (Betic Cordillera-Spain) kinematic implications. *International Journal of Earth Science (Geol Rundsch)*, **93**: 189-206.

Martínez-Martínez, J.M., Booth-Rea, G., Azañón, J.M., Torcal, F., 2006. Active transfer fault zone linking a segmented extensional system (Betics, southern Spain): Insight into heterogeneous extension driven by edge delamination. *Tectonophysics*, **422**: 159-173.

Martínez-Martínez, J.M., Soto, J.I., 2002. Orthogonal folding of extensional detachtments: Structure and origin of the Sierra Nevada elongated dome (Betics, Spain). *Tectonics*, **21**(3): 1-22.

Martínez-Martínez, J.M., Soto, J.I., Balanyá, J.C., 1997. Crustal decoupling and intracrustal flow beneath domal exhumed core complexes, Betics (SE Spain). *Terra Nova*, **9**: 223-227.

Martínez-Martínez, J.M., Soto, J.I., Balanyá, J.C., 2004. Elongated domes in extended orogens: A mode of mountain uplift in the Betics (southeast Spain). In: D.L. Whitney, C. Teyssier, C.S. Siddoway (Eds.), *Gneiss domes in orogeny*. Geological Society of America, Boulder, Colorado, pp. 243–266.

Masek, J.G., Isacks, B.L., Gubbels, T.L., Fielding, E.J., 1994. Erosion and tectonics at the margins of Continental Plateaus. *Journal of Geophysical Research*, **99**: 13941-13956.

Menéndez, I., Martín Betancur, M., Silva, P.G., 2007. Morfología de perfiles longitudinales y tasas de incisión – elevación en el sector norte de la isla de Gran Canaria (España). *Cuaternario y Geomorfología*, **18**: 15-27.

Menendez, I., Silva, P.G., Martin-Betancor, M., Perez-Torrado, F.J., Guillou, H., Scaillet, S., 2008. Fluvial dissection, isostatic uplift, and geomorphological evolution of volcanic islands (Gran Canaria, Canary Islands, Spain). *Geomorphology*, **102**(1): 189-203.

Merritts, D., Vincent, K.R., 1989. Geomorphic Response of Coastal Streams to Low, Intermediate, and High-Rates of Uplift, Mendocino Triple Junction Region, Northern California. *Geological Society of America Bulletin*, **101**(11): 1373-1388.

Moglen, G.E., Bras, R.L., 1995. The effect of spatial heterogeneties on geomorphic expression in a model of basin evolution. *Water Resources Research*, **31**(10): 2613-2623.

Molin, P., Pazzaglia, F.J., Dramis, F., 2004. Geomorphic expression of active tectonics in a rapidly-deforming forearc, sila massif, calabria, southern Italy. *American Journal of Science*, **304**(7): 559-589.

Morales, J., Serrano, I., Vidal, F., Torcal, F., 1997. The depth of the earthquake activity in the Central Betics (Southern Spain). *Geophysical Research Letters*, **24**(24): 3289-3292.

Moran, P.A.P., 1950, Notes on continuous stochastic phenomena, *Biometrika*, **37**: 17-23.

Muñoz, D., Cisternas, A., Udías, A., Mezcua, J., Sanz de Galdeano, C., Morales, J., Sánchez-Venero, M., Haessler, H., Ibañez, J., Buforn, E., Pascual, G., Rivera, L., 2002. Microseismicity and tectonics in the Granada Basin (Spain). *Tectonophysics*, **356**: 233-252.

Necea, D., Fielitz, W., Matenco, L., 2005. Late Pliocene-Quaternary tectonics in the frontal part of the SE Carpathians: Insights from tectonic geomorphology. *Tectonophysics*, **410**(1-4): 137-156.

O' Callaghan, J.F., Mark, D.M., 1984. The Extraction of Drainage Networks from Digital Elevation Data. *Computer Vision Graphics and Image Processing*, **28**(3): 323-344.

Ohmori, H., 1993. Changes in the hypsometric curve trhough mountain building resulting from concurrent tectonics and denudation. *Geomorphology*, **8**: 263-277.

Ord, J.K., Getis, A. 1995. Local spatial autocorreltacion statistics. Distributional issues and application, *Geographical Analysis*, **27**: 286-306.

Orozco, M., Alvarez-Valero, A.M., Alonso-Chaves, F.M., Platt, J.P., 2004. Internal structure of a collapsed terrain The Lujar syncline and its significance for the fold- and sheet-structure of the Alboran Domain (Betic Cordilleras, Spain). *Tectonophysics*, **385**(1-4): 85-104.

Ortiz, J.E., Torres, T., Juliá, R., Delgado, A., Llamas, F.J., Soler, V., Delgado, J., 2004. Numerical dating algorithms of amino acid racemization ratios from continental ostracodes. Application to the Guadix-Baza Basin (southern Spain). *Quaternary Science Reviews*, **23**(5-6): 717-730.

Ouchi, S., 1985. Response of Alluvial Rivers to Slow Active Tectonic Movement. *Geological Society of America Bulletin*, **96**(4): 504-515.

Pedrera, A., Pérez-Peña, J.V., Galindo-Zaldívar, J., Azañón, J.M., Azor, A., 2009. Testing the sensitivity of geomorphic indices in areas of low-rate active folding (eastern Betic Cordillera, Spain). *Geomorphology*, DOI: 10.1016/j.geomorph.2008.09.026.

Pélaez-Montilla, J.A., Sanz de Galdeano, C., López Casado, C., 2001. Potencialidad sísmica de las fallas de la cuenca de Granada. In: C. Sanz de Galdeano, J.A. Pelaez Montilla , A.C. López Garrido (Eds.), *La cuenca de Granada. Estructura, tectónica activa, sismicidad, geomorfología y dataciones existentes*. Universidad de Granada, Granada, pp. 158-174.

Pérez-Peña, J.V., Azañón, J.M., Azor, A., 2009a. CalHypso: An ArcGIS extension to calculate hypsometric curves and their statistical moments. Applications to drainage basin analysis in SE Spain. *Computers & Geosciences*, DOI: 10.1016/j.cageo.2008.06.006.

Pérez-Peña, J.V., Azañón, J.M., Azor, A., Tuccimei, P., Della Seta, M., Soligo, M., 2009b. Quaternary landscape evolution and erosion rates for an intramontane Neogene basin (Guadix-Baza basin, SE Spain). *Geomorphology*, DOI: 10.1016/j.geomorph.2008.10.018.

Pérez-Peña, J. V., J. M. Azañón, A. Azor, J. Delgado, González-Lodeiro, F., 2009c. Spatial analysis of stream power using GIS: SLk anomaly maps, *Earth Surface Processes and Landforms*, **34**: 16-25.

Pérez-Peña, J.V., Azañón, J.M., Delgado, J., 2004. Metodología para el análisis de redes de drenaje mediante índices geomorfológicos y su relación con la tectónica activa. *Geotemas*, **6**(4): 259-262.

Peuker, T.K., Douglas, D.H., 1975. Detection of surface-specific points by local parallel processing of discrete terrain elevation data. *Computer Graphics and Image Processing*, **4**: 375-387.

Pike, R.J., Wilson, S.E., 1971. Elevation-relief ratio, hypsometric integral, and geomorphic area-altitude analysis, *Geological Society of America Bulletin*, **82**: 1079-1084.

Pizzuto, J.E., 1992. The Morphology of Graded Gravel Rivers-a Network Perspective. *Geomorphology*, **5**(3-5): 457-474.

Platt, J.P., Allerton, S., Kirker, A., Mandeville, C., Mayfield, A., Platzman, E.S., Rimi, A., 2003. The ultimate arc: Differential displacement, oroclinal bending, and vertical axis rotation in the External Betic-Rif arc. *Tectonics*, **22**(3), DOI: 10.1029/2001TC001321.

Platt, J.P., Vissers, R.L.M., 1989. Extensional collapse of thickened continental lithosphere: A working hypothesis for the Alboran Sea and Gibraltar Arc. *Geology*, **17**: 540-543.

Pratt-Sitaula, B., Burbank, D.W., Heimsath, A., Qjha, T., 2004. Landscape disequilibrium on 1000-10,000 year scales Marsyandi River, Nepal, central Himalaya. *Geomorphology*, **58**(1-4): 223-241.

Ramsay, J.G., Huber, M.I., 1987. The Techniques of Modern Structural Geology 2: Folds and Fractures. Academic Press, London, 391 pp.

Ratcliffe, J.H., McCullagh, M.J., 1998. Identifying repeat victimization with GIS, *British Journal of Criminololy*, **38**: 651-662.

Reinhardt, L.J., Bishop, P., Hoey, T.B., Dempster, T.J., Sanderson, D.C.W., 2007a. Quantification of the transient response to base-level fall in a small mountain catchment: Sierra Nevada, southern Spain. *Journal of Geophysical Research-Earth Surface*, **112**, DOI: 10.1029/2006jf000524.

Reinhardt, L.J., Dempster, T.J., Shroder, J.F., Persano, C., 2007b. Tectonic denudation and topographic development in the Spanish Sierra Nevada. *Tectonics*, **26**(3), DOI: 10.1029/2006tc001954.

Rigon, R., RodriguezIturbe, I., Maritan, A., Giacometti, A., Tarboton, D.G., Rinaldo, A., 1996. On Hack's law. *Water Resources Research*, **32**(11): 3367-3374.

Rodríguez-Fernández, J., de Galdeano, C., 2006. Late orogenic intramontane basin development: the Granada basin, Betics (southern Spain). *Basin Research*, **18**(1): 85-102.

Ruano, P., 2003. Estructuras tectónicas recientes en la transversal central de las Cordilleras Béticas. Thesis Doctoral, University of Granada, Granada, 446 pp.

Ruiz Bustos, J.A., 2002. Mammals biostratigraphy and palaeoecology of the Pliocene continental deposits in the Betic Cordillera. *Pliocenica*, **2**: 44-64.

Salvany, J.M., 2004. Tilting neotectonics of the Guadiamar drainage basin, SW Spain. *Earth Surface Processes and Landforms*, **29**: 145-160.

Sanz de Galdeano, C., 1976. Datos sobre las deformaciones neogenas y cuaternarias del sector del Padúl (Granada), *Reunión sobre la geodinámica de las Cordilleras Béticas y el Mar de Alborán*. Univ. Granada, Granada, pp. 197-218.

Sanz de Galdeano, C., 1980. La neotectónica del norte de la depresión de Granada. *Estudios Geológicos*, **36**: 255-261.

Sanz de Galdeano, C., 1985. La fracturación del borde sur de la depresión de Granada (Discusión acerca del escenario del terremoto del 25-XII-1884). *Estudios Geológicos*, **41**: 59-68.

Sanz de Galdeano, C., 1996. Datos sobre las deformaciones neógenas y cuaternarias del sector del Padul (Granada), 1ª Conferencia Internacional Sierra Nevada. Publicaciones Universidad de Granada, Granada, pp. 219-231.

Sanz de Galdeano, C., Alfaro, P., 2004. Tectonic significance of the present relief of the Betic Cordillera. *Geomorphology*, **63**(3-4): 175-190.

Sanz de Galdeano, C., López-Garrido, A.C., 1999. Nature and impact of the Neotectonic deformation in the western Sierra Nevada (Spain). *Geomorphology*, **30**: 259-272.

Sanz de Galdeano, C., Montilla, J.A.P., Casado, C.L., 2003. Seismic potential of the main active faults in the Granada Basin (southern Spain). *Pure and Applied Geophysics*, **160**(8): 1537-1556.

Sanz de Galdeano, C., Rodríguez-Fernández, J., 1985. A Strike-Slip-Fault Corridor within the Alpujarra Mountains (Betic-Cordilleras, Spain). *Geologische Rundschau* **74**: 641-655.

Schildgen, T.F., Hodges, K.V., Whipple, K.X., Reiners, P.W., Pringle, M.S., 2007. Uplift of the western margin of the Andean plateau revealed from canyon incision history, southern Peru. *Geology*, **35**(6): 523-526.

Schoenbohm, L.M., Whipple, K.X., Burchfiel, B.C., Chen, L., 2004. Geomorphic constraints on surface uplift, exhumation, and plateau growth in the Red River region, Yunnan Province, China. *Geological Society of America Bulletin*, **116**(7-8): 895-909.

Schumm, S.A., 1956. Evolution of drainage systems and slopes in badlands at Perth Amboy, New Jersey. *Geological Society of America Bulletin*, **67**: 597-646.

Schumm, S.A., Dumont, J.F., Holbrook, J.M., 2000. Active tectonics and alluvial rivers. Cambridge University Press, Cambridge, 292 pp.

Schwarcz, H.P., Latham, A.G., 1989. Dirty calcites 1. Uranium-series dating of contaminated calcites using leachates alone. *Chemical Geology*, **80**: 35-43.

Scott, G.R., Gibert, L., Gibert, J., 2007. Magnetostratigraphy of the Orce Region (Baza Basin), SE spain: New chronologies for Early Pleistocene faunas and hominid occupation sites. *Quaternary Science Reviews*, **26**(3-4): 415-435.

Seeber, L., Gornitz, V., 1983. River Profiles Along the Himalayan Arc as Indicators of Active Tectonics. *Tectonophysics*, **92**(4): 335-367.

Seong, J.C., Choib, J., 2007. GEODIST: A C++ program for calculating geodesic distances with a shapefile. *Computers & Geosciences*, **33**: 705-708.

Silva, P.G., Goy, J.L., Zazo, C., Bardají, T., 2003. Fault-generated mountain fronts in southeast Spain: geomorphologic assessment of tectonic and seismic activity. *Geomorphology*, **50**: 203-225.

Small, E.E., 1999. Estimates of regolith production from 10Be and 26Al; evidence for steady state alpine hillslopes. *Geomorphology*, **27**: 131-150.

Small, E.E., Anderson, R.S., 1998. Pleistocene relief production in Laramide mountain ranges, western United States. *Geology*, **26**: 123-126.

Starkel, L., 2003. Climatically controlled terraces in uplifting mountaines areas. *Quaternary Science Reviews*, **22**(20): 2189-2198.

Stich, D., Ammon, C.J., Morales, J., 2003. Moment tensor solutions for small and moderate earthquakes in the Ibero-Maghreb region. *Journal of Geophysical Research-Solid Earth*, **108**, DOI: 10.1029/2002JB002057.

Stock, G.M., Anderson, R.S., Finkel, R.C., 2005. Rates of erosion and topographic evolution of the Sierra Nevada, California, inferred from cosmogenic Al-26 and Be-10 concentrations. *Earth Surface Processes and Landforms*, **30**(8): 985-1006.

Strahler, A.N., 1952. Hypsometric (area-altitude) analysis of erosional tophography. *Geological Society of America Bulletin*, **63**: 1117-1142.

Summerfield, M.A., 1991. Global Geomorphology. Longman Group Ltd., Singapore, 537 pp.

Tarboton, D.G., 1997. A new method for the determination of flow directions and upslope areas in grid digital elevation models. *Water Resources Research*, **33**(2): 309-319.

Townsend, P.A., Walsh, S.J., 1998. Modeling floodplain inundation using an integrated GIS with radar and optical remote sensing. *Geomorphology*, **21**(3-4): 295-312.

Tuccimei, P., Giordano, G., Tedeschi, M., 2006. CO2 release variations during the last 2000 years at the Colli Albani volcano (Roma, Italy) from speleothems studies. *Earth and Planetary Science Letters*, **243**(3-4): 449-462.

Unwin, D.J., 1996. GIS, spatial analysis and spatial statistics, *Progress in Human Geography,* **20**: 540-551.

Van Bemmelen, R.W., 1927. Bijdrage tot de geologie der Betisch Ketens in de provincie Granada. Thesis Doctoral, University of Delft, Delft.

van der Beek, P., Braun, J., 1998. Numerical modeling of landscape evolution on geologic time-scales: A parameter analysis and comparison with the south-eastern highlands of Australia, *Basin Research*, **10**: 49-68.

van der Beek, P., Champel, B., Mugnier, J.L., 2002. Control of detachment dip on drainage development in regions of active fault-propagation folding. *Geology*, **30**(5): 471-474.

Vandekerckhove, L., Poesen, J., Wijdenes, D.O., Gyssels, G., 2001. Short-term bank gully retreat rates in Mediterranean environments. *Catena*, **44**(2): 133-161.

Vera, J.A., 1970. Estudio estratigráfico de la depresión de Guadix-Baza. *Boletín Geológico y Minero*, **81**: 429-462.

Vera, J.A., 2001. Evolution of the South Iberian continental margin. In: P.A. Ziegler, W. Cavazza , A.F.H. Robertson (Eds.), *PeriTethys Memoir: Peri Tethyan Rift/Wrench Basins and Passive margins*. PeriTethys Memoir. Mémoires du Muséum national d'Histoire naturelle, Paris, pp. 109-143.

Viseras, C., 1991. Estratigrafía y sedimentología del relleno aluvial de la Cuenca de Guadix (Cordilleras Béticas), Thesis Doctoral, University of Granada, Granada.

Walcott, R.C., Summerfield, M.A., 2008. Scale dependence of hypsometric integrals: An analysis of southeast African basins, *Geomorphology*, **96**: 174-186.

Watchman, A.L., Twidale, C.R., 2002. Relative and 'absolute' dating of land surfaces. *Earth-Science Reviews*, **58**(1-2): 1-49.

Watts, A.B., Platt, J.P., Bulh, P., 1993. Tectonic evolution of the Alboran Sea Basin. *Basin Research*, **5**: 153-177.

Wegmann, K.W., Pazzaglia, F.J., 2002. Holocene strath terraces, climate change, and active tectonics: The Clearwater River basin, Olympic Peninsula, Washington State. *Geological Society of America Bulletin*, **114**(6): 731-744.

Whipple, K.X., 2004. Bedrock rivers and the geomorphology of active orogens. *Annual Review of Earth and Planetary Sciences*, **32**: 151-185.

Whipple, K.X., Tucker, G.E., 1999. Dynamics of the stream-power river incision model: Implications for height limits of mountain ranges, landscape response timescales, and research needs. *Journal of Geophysical Research-Solid Earth*, **104**(B8): 17661-17674.

Willgoose, G., 1994. A physical explanation for an observed area-slope-elevation relationship for catchments with declining relief. *Water Resources Research*, **30**: 151-159.

Willgoose, G., Hancock, G., 1998. Revisiting the hypsometric curve as an indicator of form and process in transport-limited catchment. *Earth Surface Processes and Landforms*, **23**: 611-623.

Wulder, M., Boots, B., 1998. Local spatial autocorrelation characteristics of remotely sensed imagery assessed with the Getis statistic, *International Journal of Remote Sesing*, **19**: 2223-2231.

Zhang, K., Liu, K.Y., Yang, J.C., 2004. Asymmetrical valleys created by the geomorphic response of rivers to strike-slip fault. *Quaternary Research*, **62**(3): 310-315.